Improving the Methodology and Instrumentation for On-Scalp Magnetoencephalography (MEG)

Alexandria (Xan) McPherson

A dissertation
submitted in partial fulfillment of the
requirements for the degree of

Doctor of Philosophy

University of Washington

2025

Reading Committee:
Samu Taulu, Chair
Marcel Den Nijs
Jens Gundlach

Program Authorized to Offer Degree:
Department of Physics

University of Washington

Abstract

Improving the Methodology and Instrumentation for On-Scalp Magnetoencephalography (MEG)

Alexandria (Xan) McPherson

Chair of the Supervisory Committee:
Samu Taulu
Department of Physics

The recent implementation of novel on-scalp magnetoencephalography (MEG) sensors, specifically optically pumped magnetometers (OPM), has brought about exciting prospects for more precise measurements of natural human brain activity. In order to leverage the full potential of on-scalp systems, certain challenges must be overcome, requiring improvements in both the methodology and instrumentation of these MEG systems. First, traditional signal space separation (SSS) methods for isolating the weak, pico-Tesla (pT) magnetic fields generated form neuronal activity fail when the MEG sensors are on the scalp, as opposed to elevated above the head in a liquid helium Dewar as with traditional, cryogenic MEG systems made of Superconducting Quantum Interference Devices (SQUID). Next, due to the increased proximity of sensors to the brain, on-scalp systems can in principle capture higher spatial frequencies of magnetic signal topology, but current inverse methods may fail with the increased impacts from noise that comes with higher frequency components. Finally, the OPM sensors themselves are more sensitive to low-frequency and DC fields than SQUID MEG systems, so new hardware and magnetic field compensation techniques are needed to reduce the remnant magnetic field around the sensor systems.

In this dissertation, we first present the novel multi-SSS (mSSS) method, a straightforward mathematical adaptation to the SSS method to account for the on-scalp sensor geometry with

various OPM systems. Next, we explore the applications of a matrix regularization method, Foster's Inverse, on SSS to reduce the detrimental impacts of sensor noise on the reconstruction of the internal brain activity, specifically when focusing on higher order components of the magnetic field. Finally, we discuss challenges and current solutions for reducing the remnant magnetic field in the presence of OPM sensors low enough for desired operation, and present the coil compensation system designed for use at the Institute for Learning and Brain Sciences (I-LABS) MEG Center, University of Washington. All three of these projects culminate to an advancement of the methodology and instrumentation needed for successful studies of human brain activity with on-scalp MEG systems.

TABLE OF CONTENTS

LIST OF FIGURES

ACKNOWLEDGMENTS

First, I would like to thank my advisor Samu Taulu for all the ideas, assistance, support, and new opportunities that he gave me during my time at I-LABS. I am beyond grateful for his part in my transformative time here at UW, and thankful for the future connections!

I would also like to thank my committee for their constructive feedback and kind words during the general and final exams: Marcel den Nijs, Adrian KC Lee, Paul Wiggins, Jens Gundlach, and Sarah Tuttle.

A big thank you to all the collaborators and colleagues that I had the pleasure and opportunity to meet along the way, including Iman Fahmy, Steven Bierer, Eric Larson, McKay Oyler, Niall Holmes, Wan Jin Yeo, Ashley Drew, Alexis Bosseler, Abigail George, Erica Peterson, Dan McCloy, and all of the lovely people at I-LABS and the Physics Department at UW. I have learned so much from you all and am beyond thankful for your constant support.

A big thanks to my family for always being there for me, supporting me through it all, celebrating me, and being a great audience for all of my practice presentations.

Last, but certainly not least, I'd like to thank all the amazing friends I made in Seattle, from the Physics department and beyond. Thank you for making me smile, adventuring with me, and making the rainy winters a lot less gloomy. I will miss you all dearly - you better visit me! To The Rag, thank you for reminding me how much I love playing music! To Mt Hood, Mt Ranier, Lake Ann, Mt Shuksan, Mt Baker, Mt Mystery, Gothic Basin, Blue Lake, Cutthroat Lake, Maple Pass, Panorama Point, Copper Creek, Mt Townsend, Lake 22, Heather Lake, Tolmie Peak, Snow Lake, Blanca Lake, Big Heart Lake, Mount Blanc, Hauteluce, and all the other trails and mountains that kept me grounded, thank you for reminding me that life is more than physics, or perhaps that physics is everywhere! To my

paintbrushes, thank you for bringing my memories and dreams to life, and giving me an outlet to escape this writing! You have made me myself and I will cherish you all, always and forever.

DEDICATION

To my family and friends, both near and far.

Chapter 1

INTRODUCTION

Perhaps the greatest frontier of human knowledge is the pursuit of understanding the very tool that helps us live, study, laugh, and think - the brain. Clinicians, psychologists, engineers, neuroscientist, physicists and more have been working to understand the mysteries of how our brains work, from the microscopic neuronal level to the macroscopic functions. The advancement of non-invasive brain imaging techniques has allowed us to study function, development, and structure of the brain with low-risk procedures for the patient, and each imaging technique gives us a small piece of the human brain puzzle. Functional Magnetic Resonance Imaging (fMRI) is widely used for its ability to obtain detailed pictures of the structure and active regions of the brain by measuring a variety of markers related to the cerebral blood volume, which is correlated with higher brain activity in a specific region with more blood volume [61]. This type of fMRI, called blood-oxygen level dependent (BOLD) fMRI, measures the difference in magnetic susceptibility in oxygenated hemoglobin, which has the highest BOLD response in active areas of the brain. Other techniques include electroencephalography (EEG), which measures the electric signals of postsynaptic neuronal currents generated from large numbers of neurons [61]. Electric fields are closely related to magnetic fields, so EEG is often used in conjunction with magnetoencephalography (MEG)[16]. Each of these techniques share a common core of fundamental physics behind the mechanism of the imaging and neurobiological happenings themselves.

This dissertation focuses on MEG, a technique used to measure the weak magnetic fields produced by neuronal activity in the brain with the best combination of spatial and temporal precision over fMRI and EEG. These signals typically range from 10 fT to 1 pT in strength, 1-100 Hz in frequency, and are mainly produced by the activity of pyramidal cortical neurons

aligned perpendicular to the gray/white matter boundary [27]. Based on the magnetic field distribution provided by sensors arranged around the head, the underlying neural current can be reconstructed in a non-invasive fashion with millimeter-range spatial resolution and millisecond-range temporal resolution. Traditional MEG sensors are made of an array of superconducting quantum interference devices (SQUIDs) that are kept in the superconducting state by cooling them with liquid helium in a Dewar elevated above the patient's scalp [27], with approximately 18 mm between the room-temperature surface of the MEG helmet and the SQUID sensors themselves. Due to the spatial degradation of magnetic fields as a function of distance and the presence of numerous external noise sources, it is difficult to accurately measure these small brain signals. Additionally, noise from external sources, movement of the patient, sensor system crosstalk, and any remnant magnetic fields around the sensors can cause signal-like artifacts that are difficult to distinguish from the brain activity itself [54]. MEG studies employ a wide variety of software and hardware techniques to reduce noise levels and improve the measurement of brain activity.

The most fundamental methods for isolating neuronal magnetic fields are based on the physics of electromagnetism. Brain signals can be separated from external interference signals using, for example, the signal space separation (SSS) method (also known as Maxwell filtering), which models the quasi-static magnetic fields as a series of vector spherical harmonics (VSH), a fundamental method for the discretization of magnetic fields, with separate expansions for the brain and external contributions [51]. SSS is based only on the geometric configuration of the MEG sensor helmet in relation to the neuronal sources [53]. With current cryo-MEG sensor systems, the number of detectable degrees of freedom of the magnetic field is around 80, meaning most post-processing noise reduction methods rely on the oversampling of the magnetic field with over 300 or so independent sensor measurements.

MEG has been used for about 50 years, but full-head sensor systems were not commercially available until the 2010's, with the first IFCN-endorsed guidelines for clinical MEG published in 2018 [16]. Newer on-scalp sensors, such as optically pumped magnetometers (OPM), have recently begun to be implemented in MEG systems [42], [55] [23], [3]. OPM sensors exploit

the quantum-mechanical properties of alkali metal gas within the sensors. Energy is pumped in from a modulating laser to bring the gas atoms into the same energy level such that they are at their most sensitive to small changes in magnetic fields [55]. The changes in magnetic fields are typically measured as changes in absorption and amplitude by a second laser. The ability of OPM sensors to operate without cryogenic cooling mitigates previous issues with signal depreciation over distance and potentially allows for more naturalistic neuroscience due to the freedom of the subjects to move with the MEG array being fixed to their head [3]. This is because, unlike SQUID sensors, OPM sensors do not require thick thermal insulation or a heavy Dewar as seen in Figure 1.1. OPM sensors can be placed directly on the head as they are operated at room temperature, giving in principle a three to five-fold improvement in sensitivity to neuronal magnetic fields [55]. Additionally, OPM sensors are more versatile and can be fitted to any head shape or size, and can allow for more head movement without needing as much data processing to deal with this movement.

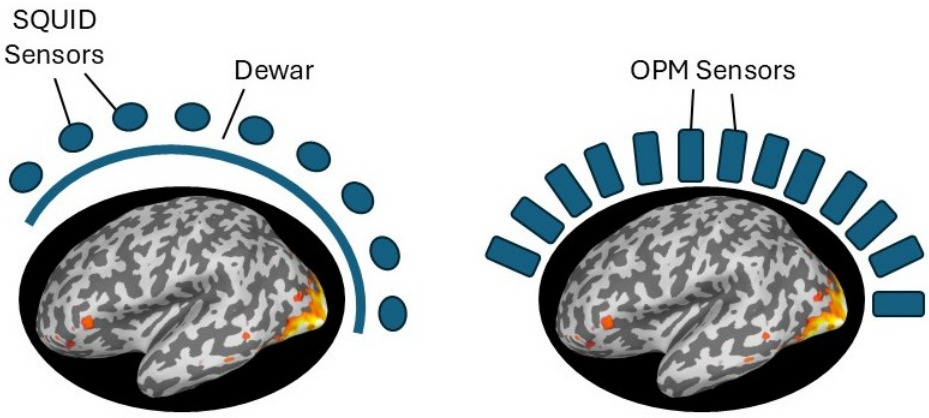

Figure 1.1: Simple schematic to visualize the main differences between common cryogenic MEG sensor systems (SQUID sensors on the left) and new on-scalp sensor systems (OPM sensors) on the right. SQUID sensors are further away from the head as they must be supercooled and housed in a Dewar, whereas OPM sensors can be placed on the scalp in more variable positions.

However, the new technology gives rise to new hardware and software considerations in order to capitalize on the potential improvements from on-scalp sensor systems. For example, OPM sensors are more sensitive to low-frequency, remnant DC magnetic fields [56], raising a need for more finely tunable technologies, including magnetically shielded room (MRS) modifications, for reducing the magnetic fields around the sensors. Other potential designs for on-scalp systems utilize nitrogen vacancy (NV) sensors, which exploit vacancy centers in diamond crystals to sense small magnetic fields [41]. Like OPM sensors, NV systems can operate at room temperature, but are theoretically more stable and robust due to their crystal structure. This dissertation focuses on OPM sensors as an example of on-scalp MEG systems as full-head NV sensor systems are not yet available, but the findings and methods developed in the following chapters are intended to be applicable to any on-scalp system.

In this dissertation, novel methods for improving the methodology and implementation of on-scalp MEG systems are developed, tested, and discussed. These improvements fall into three main projects, which make up the three Chapters after Chapter 2, which delves into the necessary background and theory to support the work in this dissertation. First, Chapter 3 discusses the development and testing of novel refined inverse models for on-scalp systems. We propose the novel multi-origin SSS (mSSS) method [35], a straightforward mathematical adaptation that allows signal space separation methods to function with on-scalp sensor systems. The mSSS method is compared to SSS and spheroidal harmonic expansions of the magnetic signals [56] on a variety of different sensor systems with simulated data, empty room MSR recordings, and single-subject data collected at the University of Washington, Nottingham, and the University College London. We end this Chapter with a discussion of the mSSS method's superior performance in a number of metrics.

Next, Chapter 4 delves into the optimization of the basic component extraction of the magnetic fields with an emphasis on noise reduction using Foster's inverse [11] matrix normalization applied to SSS signal reconstruction in order to uncover the higher-level magnetic field components that on-scalp systems can capture. Higher order components help distinguish between two neuromagnetic sources that may have similar lower order components,

giving a higher level of precision in activity localization. We discuss the importance of accurate sensor noise covariance profiles, investigate the consequences of varying profiles using simulation, and offer methodology for estimating sensor noise covariance profiles from MEG data. Finally, we demonstrate the functionality of Foster's inverse applied to SSS with a variety of datasets including a noisy current dipole simulation, SQUID-MEG Phantom datasets, and OPM-MEG single-subject recordings.

In Chapter 5, we discuss field compensation optimization using the magnetically shielded room (MSR) at the Institute for Learning and Brain Sciences (I-LABS) towards the goal of taking high-quality on-scalp MEG measurements. We begin with an overview of current field compensation system designs and implementations, then detail the simulated design of a coil compensation system for use at I-LABS that can reduce the remnant magnetic field in the MSR around the Flux OPM helmet to the safe operating regime of 5 nT. This project is a step in the long term goal of obtaining simultaneous human interaction measurements, where one subject is wearing the SQUID helmet and the other is wearing the Flux OPM system, so synchronized brain activity between two interacting people can be studied.

Finally, we offer conclusions and discuss how the work described in each of these chapters furthers the common goal of improving and expanding the clinical applications of MEG, allowing for a deeper understanding of human brain functionality.

Chapter 2

THEORETICAL BACKGROUND

In this chapter, we explore the necessary background for understanding the fundamentals of MEG and the need for improvements in methodology and implementations to match advancements in on-scalp MEG systems. We begin with a discussion of biology and neurophysiology, which drives the way we model and interpret brain signals using electromagnetism.

2.1 Neurophysiology

When our brains receive a stimulus, neurons associated with the stimulus response are activated. This activation involves the movement of Na^+, K^+, and Cl^- ions through the cellular membrane of a neuron, thus causing a shift in the relative concentration of ions on the inside of the neuron compared to the outside [27],[16]. This potential difference and ion pumping creates a current, and this current along the dendrites of multiple neurons is the origin of the magnetic fields measured by MEG.

MEG primarily measures the fields generated from postsynaptic currents in cortical pyramidal cells due to the fact that the transfer of ions at the post synapse takes longer than the pre-synaptic process, so the signals are more significant and are more likely to be picked up by the sensors [27]. The dendrites of the pyramidal cells are oriented perpendicularly to the surface of the cortex, so they guide the currents to flow perpendicularly as well. The excitatory activity of 10,000 to 50,000 pyramidal neurons results in measurable magnetic and electric fields using MEG and EEG, respectively [40].

Brain signals also have unique rhythms or frequencies that can help us tell which parts of the brain may be involved based on the MEG data itself [27]. First, the parieto-occipital

alpha rhythm is generated in the posterior part of the brain. The alpha rhythm is prominent when subjects have their eyes closed, are sleepy, unfocused, or are not using their eyes for a particular task. The mu rhythm has two components, one around 10 Hz and another around 20 Hz, that are involved in motor cortex function. Signals of 14-30 Hz are Beta rhythms and are active during sensorimotor and cognitive functions. Theta bands, from 4-7 Hz, and Delta bands, less than 3 Hz, indicate a state of lower vigilance, deep sleep, and are activated when a person is retrieving or encoding information in their working memory. These frequencies and their generation sites can be identified using MEG, as MEG sensors are designed to be sensitive to neuronal activity in the 1-100 Hz range [27].

Knowing more about the physiology of our neurons helps us create a meaningful mathematical model connecting electromagnetic equations to the human brain. For example, the permeability of each ion flowing into or out of the neuron can change with synaptic inhibition of excitation, which in turn changes the flow of voltage through a neuronal pathway depending on the particular stimulus and response. We can also use this knowledge to isolate the primary current, related to the movement of ions as discussed above, from the volume current, which are passive ohmic currents completing the loop of ionic flow as seen in Figure 2.1.

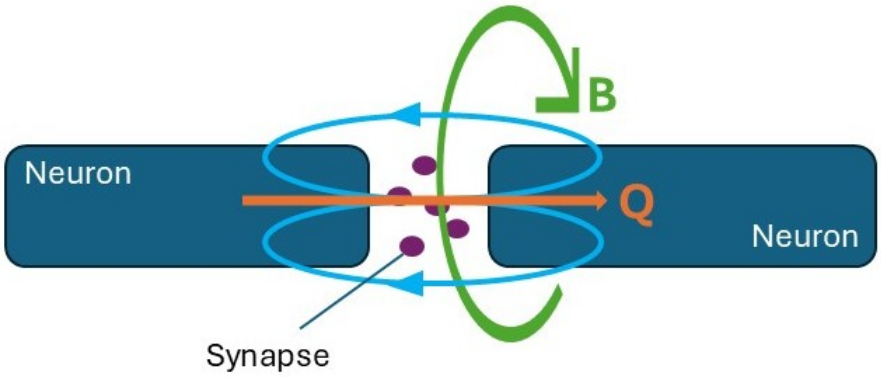

Figure 2.1: Simple schematic visualization of the postsynaptic potential, where the flow of ions (purple) across the synapse create the primary current, modeled with current dipole **Q** (orange), and resulting magnetic field **B** (green), and the volume currents (blue).

Using spherical symmetry, we can deduce that MEG measures the primary currents, which correspond to activity within the fissures of the cortex [27]. This is biologically significant since all of the primary sensory parts of the brain are located within the fissures of the cortex. From all of these anatomical considerations, the whole cortex is modeled as a homogeneous conductor, where the primary current is approximated as a current dipole determined at a neuronal level.

2.2 The Physics of MEG

The macroscopic effects of small neuronal currents create magnetic fields, which with enough neurons active as once, create a measurable effect with MEG sensors. The origins of these fields can be contextualized with fundamental electromagnetism, allowing us to model 10,000-50,000 active neurons as a current dipole source [45]. In this section, we explore the fundamental mathematical and physics basis MEG, starting with Maxwell's Equations.

2.2.1 Quasistatic Approximation of Maxwell's Equations

We can start with Maxwell's equations:

$$\nabla \cdot \mathbf{E} = -\frac{\rho}{\epsilon_0} \tag{2.1}$$

$$\nabla \times \mathbf{E} = -\frac{\partial \mathbf{B}}{\partial t} \tag{2.2}$$

$$\nabla \cdot \mathbf{B} = 0 \tag{2.3}$$

$$\nabla \times \mathbf{B} = \mu_0 \mathbf{J} + \mu_0 \epsilon_0 \frac{\partial \mathbf{E}}{\partial t} \tag{2.4}$$

From the behavior of neuronal sources, we know the time derivatives of the electric and magnetic fields are small compared to the ohmic current and that the characteristic wavelengths of biomagnetic signals are much longer than the head's diameter [27]. Thus, we can adopt the quasistatic approximation, and note that the conductivity of brain tissue is the same as free space. From this, we arrive at simplified equations for the electric fields and source potentials

$$\nabla \times \mathbf{E} = 0 \tag{2.5}$$

$$\mathbf{E} = -\nabla V \tag{2.6}$$

and the simplified versions of Maxwell's magnetic field equations

$$\nabla \times \mathbf{B} = \mu_0 \mathbf{J} \tag{2.7}$$

$$\nabla \cdot \mathbf{B} = 0. \tag{2.8}$$

The cortex is modeled as a homogeneous conductor with $\sigma(\mathbf{r})$ representing the macroscopic conductivity. This allows us to split the current $\mathbf{J}(\mathbf{r})$ into primary and volume currents

$$\mathbf{J}(\mathbf{r}) = \mathbf{J}^P(\mathbf{r}) + \sigma(\mathbf{r})\mathbf{E}(\mathbf{r}) \tag{2.9}$$

Where $\mathbf{J}^P(\mathbf{r})$ is the primary current. The primary current is concentrated into a single point using the current dipole $\mathbf{Q}$ such that

$$\mathbf{J}^P(\mathbf{r}) = \mathbf{Q}\delta(\mathbf{r} - \mathbf{r}_Q) \tag{2.10}$$

This form of a current dipole is commonly used in both MEG and EEG as as an equivalent current source that may extend over an area of the cortex on the order of a such that it represents the activity of many neurons. We can also use the primary current to obtain an equation that allows us to solve for V:

$$\nabla \cdot (\sigma \nabla V) = \nabla \cdot \mathbf{J}^P. \tag{2.11}$$

We are interested in the magnetic field, and this electric potential in Eq. 5 is an intermediate step to calculating the magnetic field. The magnetic field is calculated by the MEG sensors, and can be turned back into the neuronal activity by a process known as the inverse problem, which we will discuss in detail in the next section of this chapter. Conversely, one can construct the expected measured magnetic field generated from a single or group of current dipoles at some location in the brain, and see how well this expected value matches the measured value. This process is called the forward problem and starts with $\mathbf{B}$ given by the Ampere-Laplace law, a continuous form of the Biot-Savart Law

$$\mathbf{B}(\mathbf{r}) = \frac{\mu_0}{4\pi} \int_G \mathbf{J}(\mathbf{r}') \times \frac{\mathbf{r} - \mathbf{r}'}{|\mathbf{r} - \mathbf{r}'|^3}\, dv'. \tag{2.12}$$

For a spherically symmetric conductor with an interior current dipole, the $\mathbf{B}$ field can be simplified to

$$\mathbf{B}_z = \frac{\mu_0}{4\pi} \frac{\mathbf{Q} \times (\mathbf{r} - \mathbf{r}_Q) \cdot \mathbf{e}_z}{|\mathbf{r} - \mathbf{r}_Q|^3}. \tag{2.13}$$

We can discretize the measured potential difference V_i between two magnetometers and use

it to find a relationship between the primary current and the lead field of the ith magnetometer

$$b_i = \int_V \mathbf{L}_i(\mathbf{r}) \cdot \mathbf{J}^P(\mathbf{r}, t)\, dV \tag{2.14}$$

where

$$\mathbf{L}_i(\mathbf{r}') = [\mathbf{L}_{i1}(\mathbf{r}'), \mathbf{L}_{i2}(\mathbf{r}'), \mathbf{L}_{i3}(\mathbf{r}')]^T \tag{2.15}$$

$$\mathbf{J}^P(\mathbf{r}) = \delta(\mathbf{r} - \mathbf{r}')\mathbf{e}_j \tag{2.16}$$

.

The lead field representation has the same mathematical formalism for EEG and MEG, but MEG lead fields are magnetic flux values through the pickup loop. If the magnetometers used are planar coils, their lead fields are sensitive to the radial components of the B field, the tangential components, and the derivative of the radial field component. This is done assuming spherical symmetry. In this fashion, MEG provides a projection of the primary current $\mathbf{J}^p$ onto the lead field. These are some results of the forward problem that help provide insight into the inverse problem, and both solutions can be used in conjunction to arrive at the most likely origin of the neuronal activity measured by MEG.

2.2.2 Sarvas Current Dipole Formula

From Maxwell's equations we know that there are no magnetic monopoles, therefore the simplest source of a magnetic field is a tiny loop of current, which is essentially localized to a singular point at far away distances. In this fashion, the magnetic dipole is calculated as

$$\mathbf{B}_{dip}(\mathbf{r}) = \frac{\mu_0}{4\pi r^3} [3(\mathbf{m} \cdot \hat{\mathbf{r}})\hat{\mathbf{r}} - \mathbf{m}] \tag{2.17}$$

where $\mathbf{r}$ is the vector from the dipole to the location of each sensor in direction $\hat{\mathbf{r}}$, and $\mathbf{m}$ is the dipole moment. The magnetic flux calculated through a sensor loop can be found

using the Biot-Savart law

$$\Phi_i = \int_{\mathbf{A}_i} \mathbf{B}_{dip} \cdot \mathrm{d}\mathbf{A}_i \tag{2.18}$$

where $\mathbf{A}_i$ is the area of the coil loop, which can be determined using the dimensions of the particular MEG sensor system [31]. For example, with the MEGIN/Elekta Neuromag SQUID helmet, when numerically implemented, integration can be approximated over 9 points for magnetometers and 8 for gradiometers using a weighted numerical integration method [53].

Current dipoles are a more accurate representation of human MEG data because they match the form of the primary current originating from neurons, completed by a distribution of volume currents that are shaped by the geometry of the electric conductor structure of the head. Here, we have assumed that the neuronal activity has a small enough spatial extent per unit time to be accounted for by an equivalent current dipole (ECD) [16]. In the case of a spherically symmetric conductor, the forward field of a current dipole has an analytical form [45]:

$$\mathbf{B}(\mathbf{r}) = \frac{\mu_0}{4\pi F^2} \left(F\mathbf{Q} \times \mathbf{r}_0 - \mathbf{Q} \times \mathbf{r}_0 \cdot \mathbf{r}\nabla F\right) \tag{2.19}$$

$\mathbf{Q}$ is the current dipole defined as the primary current confined to a single point, where $\mathbf{r}$ is the vector from the origin to the location of each sensor, $\mathbf{r}_0$ is the location of the current dipole, and F is defined as $F = a(ra + r^2 - \mathbf{r}_0 \cdot \boldsymbol{r})$ with $\mathbf{a} = \mathbf{r}_0 - \mathbf{r}$ [45]. The magnetic flux from a simulated current dipole located at a specific point measured by a specific MEG system can thus be calculated using this formula.

The current dipole has a very different mathematical configuration than the magnetic dipole given in Equation 2.17: it has a focal primary current segment corresponding to postsynaptic activity in mostly pyramidal neurons, but this segment is completed by a potentially very large loop of passive volume currents. These passive currents mean the current dipole model is not suitable for external sources unless the whole conductor is taken outside of the sensor array. This would mean placing the origin of the coordinate system used

in the dipole calculation in the exterior space accordingly. Therefore, the magnetic dipole is a better model for external sources, and can be used to simulate external magnetic interference in MEG data.

2.3 Signal Reconstruction and the Inverse Problem

As briefly mentioned before, the inverse problem solves for the underlying current distribution to the measured magnetic field. There is no unique solution as there are infinitely many neuronal groupings that could result in the same magnetic field. The most likely solution is found using knowledge from neurophysiology, the physical and mathematical form of the expected current dipole signals, information about the sensor array, etc. and is computationally solved. Inverse methods can be used used in conjunction with data cleaning techniques to reach the best result for the reconstruction of interior brain signals.

MEG directly measures components of the primary current vector $\mathbf{J}^P$, which in principle is continuous and therefore has infinitely many spatial components. The measurement exists in the sensor space, characterized by the MEG sensors themselves, whereas the actual brain activity exits in the source space. One method to navigate between the two to solve the inverse problem is to construct a signal space projector (SSP), which is a projection of the measured vector onto a subspace of the signal space [29]. SSP can be used to eliminate possible sources of noise that only span a small part of the signal space and cannot be explained by the source space.

One of the most important parts of any inverse model is the equivalent current dipole (ECD), which is based on the fact that fields produced by the brain resemble dipoles that are dynamic spatially and temporally [29]. The ECD helps constrain the possible inverse solutions to ones that fit the approximate location, orientation, and collective dipole moment of a collection of modeled neuronal activity. However, the fields from a single dipole can resemble a pair of dipoles close to each other and a pair of dipoles lined up. This is a problem because our model can be incorrect even if the goodness-of-fit value indicates that the model

is functioning well.

Another common method that can be used to solve the inverse problem is the minimum-norm estimate (MNE). In this method, we look for the primary current that has the smallest overall amplitude but still contains all of the information that we need to describe the measured signals. This approach involves variations of singular value decomposition (SVD). Python's MNE package includes source estimation, machine learning for decoding models, encoding models, connectivity, and data visualization packages [31]. MNE methods can utilize a priori information to weight or normalize components of the estimate to further improve the localization of dipole activity and help combat the method's tendency to mislocate deep brain activity to the cortical surface [29]. Both SVD and noise-normalized MNE methods are discussed in greater detail in Chapters 3 and 4, respectively.

In this section, we discuss computational methods for separating the brain signals our from external magnetic sources that arise from fundamental physics and electromagnetism called the Signal Space Separation (SSS) method and other variants, as these types of methods serve as the foundation for much of the work in this dissertation.

2.3.1 Signal Space Separation Method

The Signal Space Separation (SSS) method decomposes the MEG signal vectors into two expansions of vector spherical harmonic functions - one that corresponds to sources within the sensor helmet and one that corresponds to sources outside the sensors [53],[51]. This basis separation assumes the quasistatic approximation and that the sensors are located in a current-free volume so that the magnetic field can be written as the gradient of a harmonic scalar potential,

$$\mathbf{B} = -\mu_0 \nabla V. \tag{2.20}$$

The origins of the electromagnetic signals measured by the sensor array can be deduced based on how the signals decay. Signals arising from sources within the brain should not decay at the origin, while signals that come from sources located outside the helmet should. We can further restrict the plausible subspace by only looking for signals that obey quasi-static

Maxwell's equations and can therefore be derived from the magnetostatic scalar potential. This potential satisfies Laplace's equation and has a solution that can be separated into two different sets of harmonic basis functions based on their convergence properties:

$$V(\mathbf{r}) = \sum_{l=0}^{\infty} \sum_{m} \alpha_{lm} \frac{Y_{lm}(\theta, \varphi)}{r^{l+1}} + \sum_{l=0}^{\infty} \sum_{m=-l}^{l} \beta_{lm} r^{l} Y_{lm}(\theta, \varphi), \tag{2.21}$$

where $Y_{lm}(\theta, \varphi)$ is the normalized spherical harmonic function related to the associated Legendre polynomials and the radius r is the distance from the origin to a field point located outside of the head. We can then take the gradient of this expansion for the scalar potential $V(\mathbf{r})$ to find the magnetic field $\mathbf{B}$.

$$\mathbf{B}(\mathbf{r}) = -\mu_0 \sum_{l=0}^{\infty} \sum_{m=-l}^{l} \alpha_{lm} \nabla \left[\frac{Y_{lm}(\theta, \varphi)}{r^{l+1}} \right] - \mu_0 \sum_{l=0}^{\infty} \sum_{m=-l}^{l} \beta_{lm} \nabla \left[r^{l} Y_{lm}(\theta, \varphi) \right] \tag{2.22}$$

Applying the gradient operator gives the angular dependence and can be expressed using modified vector spherical harmonics $\boldsymbol{\nu}_{lm}(\theta, \phi)$ and $\boldsymbol{\omega}_{lm}(\theta, \phi)$.

$$\mathbf{B}(\mathbf{r}) = -\mu_0 \sum_{l=0}^{\infty} \sum_{m=-l}^{l} \alpha_{lm} \frac{\boldsymbol{\nu}_{lm}(\theta, \varphi)}{r^{l+2}} - \mu_0 \sum_{l=0}^{\infty} \sum_{m=-l}^{l} \beta_{lm} r^{l-1} \boldsymbol{\omega}_{lm}(\theta, \varphi) \tag{2.23}$$

$$\mathbf{B}(\mathbf{r}) = \mathbf{B}_{\alpha}(\mathbf{r}) + \mathbf{B}_{\beta}(\mathbf{r}) \tag{2.24}$$

This expansion for $\mathbf{B}$ is a fundamental discretization of a continuous magnetic field and can be applied to multichannel measurement of electromagnetic fields. When we define the radius r as the distance from the origin to the closest sensor, the first term of the sum corresponds to signals that originate inside the brain and decay at large r, whereas the second term represents signals that are large at large distances away from the origin and thus come from signals external to the brain such that α terms denote internal signals and β terms denote external signals. The coefficients α_{lm} and β_{lm} denote the multiple moments and can

be written in a lead-field like representation using the vector spherical harmonic function $\mathbf{X}_{lm}(\theta, \varphi)$

$$\alpha_{lm} = \int_{v'} \lambda^{\alpha}_{lm}(\mathbf{r}') \cdot \mathbf{J}_{in}(\mathbf{r}')dv', \tag{2.25}$$

where $\mathbf{J}_{in}(\mathbf{r}')$ is the internal current distribution and $\lambda^{\alpha}_{lm}(\mathbf{r}')$ represent the analogy to the conventional lead fields. Fully expanded, we have

$$\lambda^{\alpha}_{lm}(\mathbf{r}') = \frac{i}{2l+1}\sqrt{\frac{l}{l+1}} r^l \mathbf{X}^*_{lm}(\theta, \varphi). \tag{2.26}$$

$\mathbf{X}_{lm}(\theta, \varphi)$ can be written using the spherical harmonic function $Y_{lm}(\theta, \varphi)$ as [51]

$$\mathbf{X}_{lm}(\theta, \varphi) = \frac{-i}{\sqrt{l(l+1)}}(\mathbf{r} \times \nabla) Y_{lm}(\theta, \varphi). \tag{2.27}$$

Note that the current $\mathbf{J}$ given from Maxwell's equations as the curl of the magnetic field must be zero given the VSH expansion of $\mathbf{B}$, meaning the sensors must be located in a source-free zone outside of the head. For computational applications, the measured signal vector $\boldsymbol{\phi}$ can be written as follows

$$\boldsymbol{\phi} = \sum_{l=1}^{L_{in}} \sum_{m=-l}^{l} \alpha_{lm} \mathbf{a}_{lm} + \sum_{l=1}^{L_{out}} \sum_{m=-l}^{l} \beta_{lm} \mathbf{b}_{lm}, \tag{2.28}$$

where $\mathbf{a}_{lm}$ and $\mathbf{b}_{lm}$ are the signal vector responses of the multichannel measurement device and $\boldsymbol{\phi} = [\phi_1 ... \phi_N]^T$ is the measures signal vector of all N channels. The $l = 0$ components are excluded because they correspond to magnetic monopoles, which do not exist according to Maxwell's equations. This form of $\boldsymbol{\phi}$ can be expressed in matrix notation as:

$$\boldsymbol{\phi} = \mathbf{S}\mathbf{x} = \begin{bmatrix} \mathbf{S}_{in} & \mathbf{S}_{out} \end{bmatrix} \begin{bmatrix} \mathbf{x}_{in} \\ \mathbf{x}_{out} \end{bmatrix}. \tag{2.29}$$

Here, $\mathbf{S}$ is the magnetic subspace containing separate subspaces for internal and external

sources, and the corresponding multiple moments are contained in vector $\mathbf{x}$. The moments L of the interior and exterior expansions are truncated at $L_{in} = 8$ and $= L_{out} = 3$ [53], resulting in a $(L_{in}+1)^2 + (L_{out}+1)^2 + 2 = D$ dimensional space. The interior basis represented by $\mathbf{S}_{in}$ can be used to reconstruct the raw data in a way that excludes any noise that came from signals outside of the helmet. This reconstruction is done by first finding an estimate for the multipole moments $\hat{\mathbf{x}}$ using the pseudo-inverse inverse of the full SSS basis.

$$\hat{\mathbf{x}} = \begin{bmatrix} \hat{\mathbf{x}}_{in} \\ \hat{\mathbf{x}}_{out} \end{bmatrix} = \mathbf{S}^{\dagger}\boldsymbol{\phi}. \tag{2.30}$$

The internal signals $\boldsymbol{\phi}$ are then reconstructed using the internal SSS basis and the estimated multipole moments as $\boldsymbol{\phi}_{in} = \mathbf{S}_{in}\hat{\mathbf{x}}_{in}$. The reconstruction allows for a clearer and more accurate representation of the signals that were produced by the brain during a specific period of time, cleaned of external magnetic field interference, only requiring the sensor geometry to be known.

2.3.2 Extended Signal Space Separation

Extended SSS combined traditional SSS with statistical aspects from SSP in order to improve the behavior under external interference and reduces sensitivity to geometry and sensor calibration errors [17]. However, eSSS requires empty-MSR recording in order to establish the dominant principle components of the external interference ($\boldsymbol{PC}_{out}$). The external SSS basis is augmented as follows

$$\mathbf{S}_{out,e} = orth([\mathbf{S}_{out}\mathbf{PC}_{out}]) \tag{2.31}$$

where the orthogonal function can be done using SVD. The new $\boldsymbol{S}_{out,e}$ matrix contains features that correct the inaccuracies due to calibration and geometry errors. The combined $\boldsymbol{S}_e$ matrix can then be used as normal in SSS calculations for reconstructing data.

$$\mathbf{S}_e = [\mathbf{S}_{in}\mathbf{S}_{out,e}] \tag{2.32}$$

This SSS basis can be further augmented to include band-pass filtered PC's to suppress known artifacts, and it can be combined with spatiotemporal (tSSS) to deal with other kinds of artifacts. eSSS is able to suppress artifacts caused by asynchronous artifacts in the sensor array that SSS cannot. It has been found that eSSS significantly improves external interference suppression, does not increase error in source estimations, has a similar truncation level as SSS, but requires an empty-MSR to correct for inaccurate calibration information.

2.3.3 Spatiotemporal Signal Space Separation

Conventional interference rejection methods struggle to remove unwanted signals that originate close to the sensor array. Spatiotemporal SSS (tSSS) can remove both external interference and artifacts produced by unwanted nearby sources by using Maxwell's equations, sensor geometry, and statistical analysis in the time domain. This opens the scope of clinical research to more patients with potential magnetic impurities [52]. SSS cannot separate sources very close to the sensors, but we can recognize these signals by finding and extracting temporal components that are found in both the internal and external multipole moments.

Two sources of inaccuracy in the SSS reconstructions come from errors in truncation of the harmonic expansions and calibration issues in the MEG sensor array. These errors can be mathematical shown in the interior and exterior multipole expansions as

$$\hat{\mathbf{X}}_{in} = \hat{\mathbf{X}}_{in,0} + \hat{\mathbf{X}}_{in,\epsilon} \tag{2.33}$$

$$\hat{\mathbf{X}}_{out} = \hat{\mathbf{X}}_{out,0} + \hat{\mathbf{X}}_{out,\epsilon} \tag{2.34}$$

Where the subscript 0 represents the undistorted reconstruction of the brain signal and ϵ denotes the errors from truncation and calibration. The undistorted estimates are uncorrelated whereas the errors are correlated and cause multipole moment mixing between the interior and exterior basis components. We can find the correlated sources by first taking the SVD of $\hat{\mathbf{X}}_{in,\epsilon}$ and $\hat{\mathbf{X}}_{o,\epsilon}$, denoted as bases $\mathbf{C_{in}}$ and $\mathbf{C}_{out}$. Then, the correlation is the overlap of these two bases in the temporal domain $\mathbf{L} = \mathbf{C}_{in} \cap \mathbf{C}_{out}$. $\mathbf{L}$ will be empty in the absence of

nearby interference and with perfect calibration. The overlap and comparison is done with a small positive inaccuracy value δ so that two vectors are considered identical when the angle between them θ satisfies $cos(\theta) > 1 - \delta$. Examples with data and simulations have shown that the best values are $\delta = 0.01 - 0.05$ [52].

L, as an orthonormal basis, can be used to construct a projection operator to remove the time patterns from the multipole moments

$$\hat{\mathbf{X}}_{in,p} = \left[(\mathbf{I} - \mathbf{L}\mathbf{L}^T)\hat{\mathbf{X}}_{in}^T\right]^T. \tag{2.35}$$

Any randomly chosen high-dimensional vectors are approximately orthogonal to each other, so over a long period of time the brain and interference signals are close to orthogonal, meaning $\hat{\mathbf{X}}_{in,p} \approx \hat{\mathbf{X}}_{in,0}$. This projection operator is the same as SSP, but applied in the temporal domain as opposed to spatial domain. The same method can be used with the data vector Φ as opposed to the multiple moments as shown. tSSS reduces the artifact noise down to the noise level.

2.3.4 Iterative Signal Space Separation

SSS methods are defined by the sensor geometry, both in position and number. For current OPM systems, the low number of channels detrimentally effects the performance of SSS. The noise and condition number of the internal basis matrix increase as more internal multipole components are kept. To combat this problem, SSS methods can be conducted iteratively based on the hierarchy of the multipole orders in the expansion [21]. The reconstruction noise n_r is calculated as a ratio of the noise between the internal signal vector and full signal vector

$$n_r = \frac{||\hat{\phi}_{in,noise}||}{||\phi_{noise}||} \tag{2.36}$$

.

The iterative approach reduces this ratio by assuming that lower order multipole components contain the most important information about the signal. The first step is to separate

the inner subspace by multiple order ($l = 1$ up to $l = L_{in}$)

$$\mathbf{S}_{in} = [\mathbf{S}_{in,l=1}, \mathbf{S}_{in,l=2}...\mathbf{S}_{in,l=L_{in}}]\,. \tag{2.37}$$

Next, a partial basis can be established using only the first order components of both the $\mathbf{S}_{in}$ basis and corresponding amplitudes, or weights, $\mathbf{x}_{in}$. The first order weight, $\mathbf{x}_{in,l=1}$, is estimated using a measured signal vector $\boldsymbol{\phi}$ and the partial basis as

$$\mathbf{x}_{in,l=1} = \mathbf{S}^{\dagger}_{in,l=1}\boldsymbol{\phi} \tag{2.38}$$

The calculated estimate for $\mathbf{x}_{in,l=1}$ is then used to calculate $\mathbf{x}_{in,l=2}$ by subtracting the $l = 1$ component out of the measured signal.

$$\mathbf{x}_{in,l=2} = \mathbf{S}^{\dagger}_{in,l=2}(\boldsymbol{\phi} - \mathbf{S}[\mathbf{x}_{in,l=1}, 0, ...0]^T) \tag{2.39}$$

Where the matrix $\mathbf{x}$ only contains the information from the first order: $\mathbf{x} = [\mathbf{x}_{in,l=1}, 0, ...0]^T$. $\mathbf{x}_{in,l=2}$ can be found next by subtracting out the first two contributions

$$\mathbf{x}_{in,l=3} = \mathbf{S}^{\dagger}_{in,l=3}(\boldsymbol{\phi} - \mathbf{S}[\mathbf{x}_{in,l=1}, \mathbf{x}_{in,l=2}, 0...0]^T). \tag{2.40}$$

We continue to iteratively calculate $\mathbf{x}_{it,in}$ (with subscript "it" denoting the iterative process) for all L_{in} components to reconstruct the interior data as

$$\boldsymbol{\phi}_{in} = \mathbf{S}_{in}\mathbf{x}_{it,in}. \tag{2.41}$$

After five iterations, the SSS expansions are more stable with lower reconstruction noise than without iterations on a simulated 192-channel system [21]. An optimal 10 iterations is sufficient to improve the reconstruction of the interior signals for low channel count systems.

2.4 MEG hardware

2.4.1 Superconducting Quantum Interference Devices (SQUID)

Historically, SQUID sensor systems are the most widely used MEG system around the world. As they are superconductors, the sensors are housed in a thermally insulated helmet surrounded by a liquid helium Dewar kept at around $-270°$C [27], [14]. SQUID systems are typically made up of a combination of magnetometers and gradiometers, which measure the magnetic field components and gradients. In this dissertation, we focus on the Megin/Elekta Neuromag SQUID sensor system, which is the kind of sensor system located at I-LABS at UW. The Megin/Elekta Neuromag system is composed of 204 planar gradiometers and 102 magnetometers for a total of 306 channels to sample the magnetic field around a subject's head. The magnetometers have an approximate radius of 8.1 mm (diameter of 16.2 mm) and planar gradiometers have a radius of 8.4 mm (diameter of 16.8 mm) when implemented numerically [31]. On average, the sensors are 35 mm apart and are located about 18 mm away from the surface of the helmet, which is at room temperature [**?**]. A visualization of the difference between the magnetometers and planar gradiometer sensors that compose the Megin/Elekta Neuromag SQUID sensor system is given in Figure 2.2

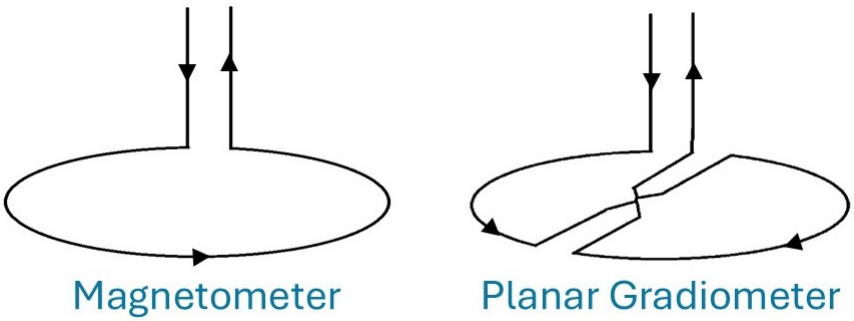

Figure 2.2: Simple schematic visualization of magnetometer and planar gradiometers, the two types of sensors used in the typical Megin/Elekta Neuromag SQUID MEG sensor system.

The typical noise floor for SQUID magnetometers is around 3.5 fT/$\sqrt{\text{Hz}}$ and 3.6 fT/cm/$\sqrt{\text{Hz}}$ with <0.1% crosstalk between the sensors [**?**]. Despite the cost, weight, and extra considerations with liquid helium management, the low noise of SQUID systems sets the bar that other, newer, MEG sensor systems will have to at the very least match in order to maintain our ability to localize brain activity with current precision levels.

Other than MEG channels, the Megin/Elekta Neuromag helmet contains up to 128 EEG channels for simultaneous EEG/MEG measurements and 16 trigger channels for keeping track of stimulus onset during clinical testing. In general, the magnetic flux through each of the 306 SQUID sensors in this system is calculated as

$$\Phi_i = \int_{\mathbf{A}_i} \mathbf{B}_{dip} \cdot \mathrm{d}\mathbf{A}_i \tag{2.42}$$

where $\mathbf{A}_i$ is the area of the coil loop, visualized in Figure 2.2, using standard gradiometer and magnetometer dimensions for SQUID sensors. Magnetometer can also be modeled as point magnetometers, which requires no numerical integration during data processing. In clinical and research settings, the Megin/Elekta Neuromag MEG system also comes with software packages for data processing including Maxwell Filtering, which includes SSS and an additional step of removing high-frequency components of the internal basis classified as noise, and continuous head position tracking used for offline movement compensation methods, such as the spatiotemporal-SSS method [52]. The location and design of SQUID sensor systems has been heavily researched and optimized, but one of the most limiting factors for these MEG systems is the relatively large distance between the head and the sensor helmet due to the necessity of cryogenic cooling, resulting in a loss of brain signal strength and higher spatial frequency components that decay rapidly over distance. Additionally, SQUID systems are very large and expensive due to the liquid helium Dewar, which makes it less accessible to institutions without space or funds for such a system.

2.4.2 Magnetically Shielded Room (MSR)

Despite the built-in noise reduction methods in MEG systems, the sensors must be housed in a magnetically shielded room (MSR) to help attenuate against external interference and keep the background noise within the operating range of the sensors. Typically, MSRs are made of a variety of different layers for both passive and active shielding to help combat against a variety of types of interference, including magnetic fields from outside traffic, trains, metros, elevators, power lines, and more, which can cause magnetic fields of around 1-3 μT [54]. Some of these signals occur at a known frequency, like power lines at 50-60 Hz, and can be removed from the data using a notch filter during data processing, but most interference is unknown, thus the need for MSRs that can attenuate against many frequencies at once.

Passive shielding refer to layers of Mu-metal, a nickel-iron alloy that attenuates against low frequency magnetic fields, coupled with layers of highly conductive metals, like copper or aluminum, which attenuate against high frequency signals by producing eddy currents [54]. At low frequencies, below 0.1 Hz, the high-permeability metal is doing most of the shielding, and as the frequency increases, global eddy currents are induced in the conducting walls of the room. As the physics of the shielding depends on the frequency of the external magnetic field, MSR performance is given by the shielding factor $S(f) = B_{ext}(f)/B_{in}(f)$ as a ratio of the external field frequency to the internal, post-shielded field [54]. MSRs also include active shielding in the form of large orthogonal sets of coils on the walls of the MSR, which can be tuned with specific current and frequency to dynamically null remnant fields inside. This requires good knowledge of the interior fields themselves, and is typically measured by extra MEG sensors in the helmet, which read the components of the magnetic field at a location along the three cartesian axes and use this information in a negative feedback loop to control the MSR wall coils [54]. The most robust MSRs with many layers of metal provide excellent shielding, but can weight up to 20 tons and are very large and costly to install. Conversely, some lightweight, 5 tons or less, MSRs have been recently investigated to reduce the weight, cost, and size, thereby making MEG clinical trials more accessible for a variety of institutions

to install [24].

At I-LABS, we have an MSR manufactured by Imedco (see Figure 3.9) composed of alternating layers of MuMetal and Aluminum, creating a 4-layer system.

Figure 2.3: The MSR located in the MEG center of I-LABS at the University of Washington. The walls are very thick to accommodate the layers of passive and active shielding. The door is shielded with the same technology and is closed using vacuum technology.

The typical remnant field inside an MSR is around 100 nT [54]. As mentioned in the introduction, new on-scalp sensors are more sensitive to low-frequency and DC magnetic fields and require a remnant field of <5 nT [56], which means we now require more tunable MSR technologies to make sure the fields and first-order gradients around the sensor systems are as close to null as possible. Reasons for this necessity is discussed in the next section based on the mechanics and physics of the OPM sensors themselves, and we delve into work done to improve the MSR at I-LABS for the goal of taking high-quality on-scalp measurements Chapter 5 of this dissertation.

2.4.3 The Physics of Optically Pumped Magnetometers

As mentioned in the introduction, novel on-scalp sensor systems have begun to be implemented in MEG, with Optically Pumped Magnetometers (OPMs) being the most widely-used sensor type for these on scalp systems [23], [42]. Optical Pumping is a technique where a laser with a specific frequency shines on an alkali metal vapor to change the sample's quantum state [55]. A diagram of a simple OPM sensor is included in Figure 2.4

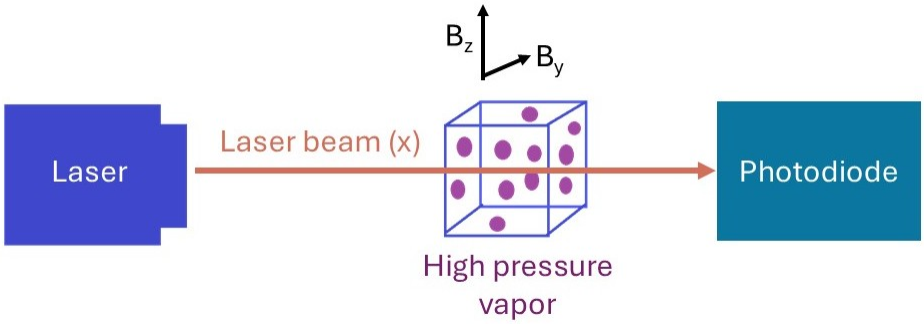

Figure 2.4: Visualization of a simplified OPM sensor. Light from the laser on the left is shone through a small glass chamber containing alkali metal vapor gas, which facilitates optic pumping. Changes in laser amplitude that passes through the gas cell is measured by a photodiode, which may also be another laser in some OPM designs. The photodiode signal is a function of the magnetic field around the gas cell.

The light from the laser transfers angular momentum to the gas such that nearly all atoms occupy the same energy level after a D1 level transition. During this optimized state, the gas is induced into a magnetically sensitive sate that allows for the measurement of weak magnetic fields. When a gas is optically pumped and reaches the specific altered quantum state, the laser frequency is no longer absorbed and carries through the material to a pickup probe. As the gas interacts with a magnetic field, the optimized state is altered, and the pumped laser can once again be absorbed. Fluctuations in the amount of energy picked up by the probe laser thus directly correlate with the magnetic field in question. The sensitivity of OPMs is increased by operating in the spin exchange relaxation free (SERF) regime, where

there is zero field and the sensors contain high density vapors. When the rate of spin exchange collisions due to high atomic density exceeds the precessional frequency (lowered by operating under a low field), a strong polarization in the gas can be maintained [56]. The operating temperature of OPMs is a little above room temperature, much warmer than SQUID sensors, and can thus be safely worn on the scalp.

In principle, OPM sensors have been show to have an intrinsic white noise level of 1 ft/$\sqrt{\text{Hz}}$, lower than SQUID sensors, but there are a variety of factors that mean in practice, the noise levels are usually higher, closer to 10-100 ft/$\sqrt{\text{Hz}}$ [55]. Methods to combat this typically address the noise levels by employing synthetic gradiometer calculations and measuring multiple components of the field simultaneously. In general, OPM sensors are more sensitive to DC and low-frequency magnetic fields, and this sensitivity is consequential in the relationship between measured laser amplitude and the magnetic field. Measured amplitude is linearly related to the magnetic field only when the OPM sensors are operating in low external fields, less than 5 nT of homogenous and static magnetic fields [56], so they data collected using OPMs becomes less reliable with larger remnant fields inside MSRs. Other than external fields, there are a few other considerations that influence the sensitivity and reliability of OPM sensors that are quite different than SQUID sensors. For example, collisions of the vapor gas atoms with the glass cells walls and with each other can disrupt, or "relax", the optically-pumped spin-state and affect the amount of modulated laser light. The responsiveness of the sensors is predominately disrupted by spin-exchange collisions, which is why most sensors are designed to operate in the SERF regime where the zero external field conditions and high density of atoms within the cell minimizes relaxation of the spin-state or spin-exchange during particle collisions [55]. The wavelength for the input laser is chosen based on the type of gas in order to create the optically pumping effect. This input laser can also be split and polarized in order to measure the different components, both scalp-radial and scalp-tangential, of the magnetic fields produced by neurons. Although co-registration between the OPM helmet and the patient's head is trivial with on-scalp systems, the newly allowed head movement can cause artifacts when the head moves through small fields with

gradients, thus further requiring that the operation of OPM systems must be done in a magnetic field less than 5nT [56].

Currently, there are a wide variety of types of OPM systems made globally by different companies, varying in sensor design, measurement direction, sensor number, and more. Here we provide some examples of current OPM systems, specifically systems that are used for investigation and data collection in this dissertation. At I-LABS, we have a full-head coverage OPM system manufactured by Kernel Flux, which features 432 individual Rubidium-gas OPM sensors mounted in an adjustable modular design with about 8 mm between the scalp and the sensors [42]. The Flux system's modular design is unique, where sensors are mounted in 3x3 grids with six sensors per grid measuring the radial component of the magnetic field and three sensors per grid measuring the tangential component of the field. Each vapor cell is 5 mm spaced from the next, resulting in a 10 mm$\times$10 mm sensor size, or about the size of a quarter. The sensors are optically pumped with a 795 nm laser, which is circularly polarized and distributed between the nine cells in each module. Cells are kept at about 120°C, which helps suppress spin-exchange collision induced relaxation and maintain the femto-Tesla sensitivity needed to measure brain signals [42]. A visualization and more details of the Kernel Flux system and others, including systems manufactured by QuSpin, are included in Figure 3.7 and discussed further in Chapter 3.

2.4.4 Summary of MEG Sensors

In this section, we present a concise table detailing the main aspects of SQUID and OPM sensors for a side-by-side comparison. Each metric is on average, and may vary between manufacturers.

Table 2.1: Average specifications and parameters for SQUID and OPM sensor system designs

Parameter	SQUID	OPM
Operating Temperature	-270°C	120°C
Sensor type	magnetometer, gradiometer	magnetometer
Size of sensor	21 mm side length	≈12 mm radius
Distance between sensors	35 mm	5 mm
Distance to scalp	18 mm	8 mm
Noise floor	$\approx$ 3.5 fT/$\sqrt{\text{Hz}}$	1-100 fT/$\sqrt{\text{Hz}}$
Crosstalk	$<$0.1%	highly variable
Operating field	20 nT	$<$5 nT

Due to the wide variety of new and developing OPM sensor system designs, the OPM entries in Table 2.1 vary more widely across different systems than the entries for SQUID sensors, and are biased towards the OPM systems discussed in this dissertation including QuSpin and Kernel, where each "sensor" is a 12mm radius casing enclosing a set of 9 OPM gas cells [42], [23]. Note that OPM sensors functions as magnetometers, but many OPM systems have built-in synthetic gradiometer calculations where the gradient of the magnetic field is calculated between two adjacent sensors [42]. Quantification of crosstalk between OPM sensors is particularly variable, both between designs, but depending on the modulating laser specifications and the proximity of the sensors.

2.5 Typical MEG Data Collection and Processing

The actual process of MEG data collection and processing has been iterated, expanded, and experimented with across the world since the beginning of the technology; however, there are general guidelines and steps that each experiment follows in order to obtain the best MEG

data recordings possible. Here, we briefly overview a typical collection and data processing pipeline to provide context for each step of this dissertation's work [16], [3], [4], [27]. First, the patient's head is digitized by marking the fiducial points, usually anatomical points like the nose, ears, chin, etc., and tracing the crown of the skull. Fiducial points (typically five) are marked with head position indication coils (cHPI) that are driven with specific frequencies of electromagnetic pulses during data collection. These signals are used to track the position of the patient's head throughout the test in relation to the location of the MEG sensors themselves. Next, the MSR is tuned with the active shielding coils to further reduce the external magnetic fields inside of the room. At this step, an empty room recording can be taken to help with noise reduction in the data later, and if an extra compensation coil system is present, it must be tuned before and potentially during data collection to dynamically null the field even more. This step is especially important for OPM MEG systems which require a background field of <5 nT for good operation. The design and use of such a compensation system is detailed in the work of Chapter 5. Then, data is collected from having the patient experience some type of stimulus (visual, auditory, etc.) within the MSR walls. The onset of each stimulus is tracked within the same data file as the magnetic MEG measurements to time stamp the dataset with periods of presumed interesting brain activity.

The first step of data processing is to visually inspect the raw data at the sensor level and remove any channels that were potentially malfunctioning during the collection. Artifacts from the heart, eyes, and external sources like power lines are also removed using bandpass and notch filtering at specific frequencies. Next, the cHPI signals are used to find the head position over time, and techniques like tSSS are applied to compensate for the movement. In this step, any combination of artifact suppression like SSS or signal space projection (SSP) can be used in conjunction with head position compensation. SSP, in particular, utilizes the principle component analysis of the empty room MSR recording to project out the assumed to be constant background noise from the data [54]. For use with on-scalp MEG systems, the SSS methods for data reconstruction need to be refined, as the work in Chapter 3 details, and improved to capture higher frequency components of the brain activity with less noise as

the work in Chapter 4 discusses.

After artifact suppression, the raw data can be parsed into time chunks using the recorded timestamps of the stimulus onsets, and evoked averaged for each type of stimulus are created. The averaging over multiple time courses of the same stimulus further reduced noise that may have arisen from the sensor themselves or other factors. Finally, the evoked data is used with both forward and inverse models to localize the current dipole sources that were active during each time point of the experiment. MNE-Python is the most commonly used package for the full MEG data analysis pipeline as it contains functionally for all steps of the process, including data visualization [31]. For example, the location and time coordinates achieved from MEG data reconstruction can be projected onto the patient's MRI for a clear picture of which areas of the brain were activated over the course of the investigation.

2.6 Clinical Uses for MEG

Here, we briefly explore the various clinical applications of MEG imaging and its impacts on the fields of neuroscience and psychology, which we use as motivation for the importance of this dissertation work.

MEG is an excellent tool for studying human brain development in infants to children because it is quiet, non-invasive, can be easily monitored by a parent nearby, and head movement compensation techniques mean the child can be fully awake and move more naturally. But, the biggest challenges, especially when using cryogenic MEG systems, are issues with co-registration between head and sensors, increased signal-to-noise ratio (SNR) due to an increased distance between scalp and sensors, and distortion of the signal due to head movement [4]. These challenges can be overcome mathematically using techniques like the minimum norm estimate (MNE) and SSS, as well as implementing best practices for infant brain imaging, leading to exciting results and studies on human brain development, specifically at the Institute for Learning and Brain Sciences.

Functional connectivity of different regions of the brain can also be readily investigated

with MEG, typically by estimates sources of activity across the brain, then measuring the connectivity afterwards. MEG, sometimes combined with EEG, is also used to study speech comprehension, specifically how the brain parses syllables, what neural representations are created, and how this information is combined with intonation and memories to result in comprehension, with public datasets readily available for study [16], [15]. MEG has also become part of the standard care at epilepsy centers, since it can localize epileptic neurons and help inform safe treatment plans even in patients with skull deformities or previous surgeries [36]. Potential clinical uses also include the study of traumatic brain injuries, stroke, Parkinson's, and other neuropsychiatric disorders [26], [16].

On-scalp MEG systems may offer more insight into the clinical studies listed above, as well as open the door to studying more diverse brain functions that require the subject to move. Some studies already conducted using OPMs include millisecond resolution of subjects nodding, stretching, drinking, and throwing/catching balls [2], [3]. Allowing the patients to move their head and body in any study will lead to more biologically natural results and a deeper insight into the human brain.

Chapter 3

REFINED SIGNAL SPACE SEPARATION METHODS FOR ON-SCALP MEG SYSTEMS

Newer on-scalp sensors, such as OPMs, have recently begun to be implemented in MEG systems. As discussed in Chapter 2, OPM sensors exploit the quantum-mechanical properties of alkali metal gas within the sensors. Energy is pumped in from a modulating laser to bring the gas atoms into the same energy level such that they are at their most sensitive to small changes in magnetic fields [55]. The changes in magnetic fields are typically measured as changes in absorption and amplitude by a second laser. The ability of OPM sensors to operate without cryogenic cooling mitigates previous issues with signal depreciation over distance and potentially allows for more naturalistic neuroscience due to the freedom of the subjects to move with the MEG array being fixed to their head [3]. This is because, unlike SQUID sensors, OPM sensors do not require thick thermal insulation or a heavy Dewar. In order to leverage the potentially improved spatial resolution provided by the on-scalp sensors, refined inverse models need to be developed for determining the origin of the magnetic signals in specific brain regions. As the distance between sensors and scalp decreases, it becomes difficult to encompass the full brain within a single sphere without the sphere protruding past the sensor array or excluding signals originating from the cortex. Current proposed solutions to this problem include modifying the VSH expansion to a prolate spheroidal harmonic expansion, allowing for a better geometric fit of the head while keeping the internal expansion within the radius of the sensors [56]. Other techniques focusing on improving SSS in on-scalp systems with low channel count include the iterative SSS method, which exploits the hierarchical nature of the spherical harmonics to stabilize matrix inversion [21]. Iterative SSS is based on single-origin VSH, so the method experiences the same problem when we

cannot safely assume that the magnetic field can be decomposed in terms of interior and exterior parts using a single reference sphere with on-scalp systems. Here, we propose an enhanced, mathematically straightforward, variant for modifying the SSS expansion to fit the on-scalp geometric constraints with multi-origin SSS (mSSS), which uses multiple optimized sets of vector spherical harmonic expansions to dynamically span the interior brain space without encroaching on the sensors.

This chapter details the mSSS method [35] and compares its effectiveness on removing external noise from MEG data against traditional and spheroidal harmonic expansions as detailed in Chapter 2. In particular, we test three variants of combining the signal space separation techniques: multi-origin VSH interior expansion with single-origin VSH exterior, spheroidal harmonic interior with spheroidal harmonic exterior [56], and spheroidal harmonic interior with single-origin VSH exterior. Each variant is implemented for 306-channel MEGIN/Elekta Neuromag sensor geometry specified from example files in MNE-Python [31], with a simplified SQUID system of only the 102 magnetometer channels of the MEGIN/Elekta Neuromag system, and the 432-channel Kernel Flux OPM-MEG [42]. A visualization of the coordinate system for each sensor helmet used can be found below in Figure 3.1. Further visuals and information for the 306-Channel MEGIN/Elekta Neuromag system, the 432-Channel Kernel OPM, and the two QuSpin systems can be found online with the relevant references [31], [42], [23], [47].

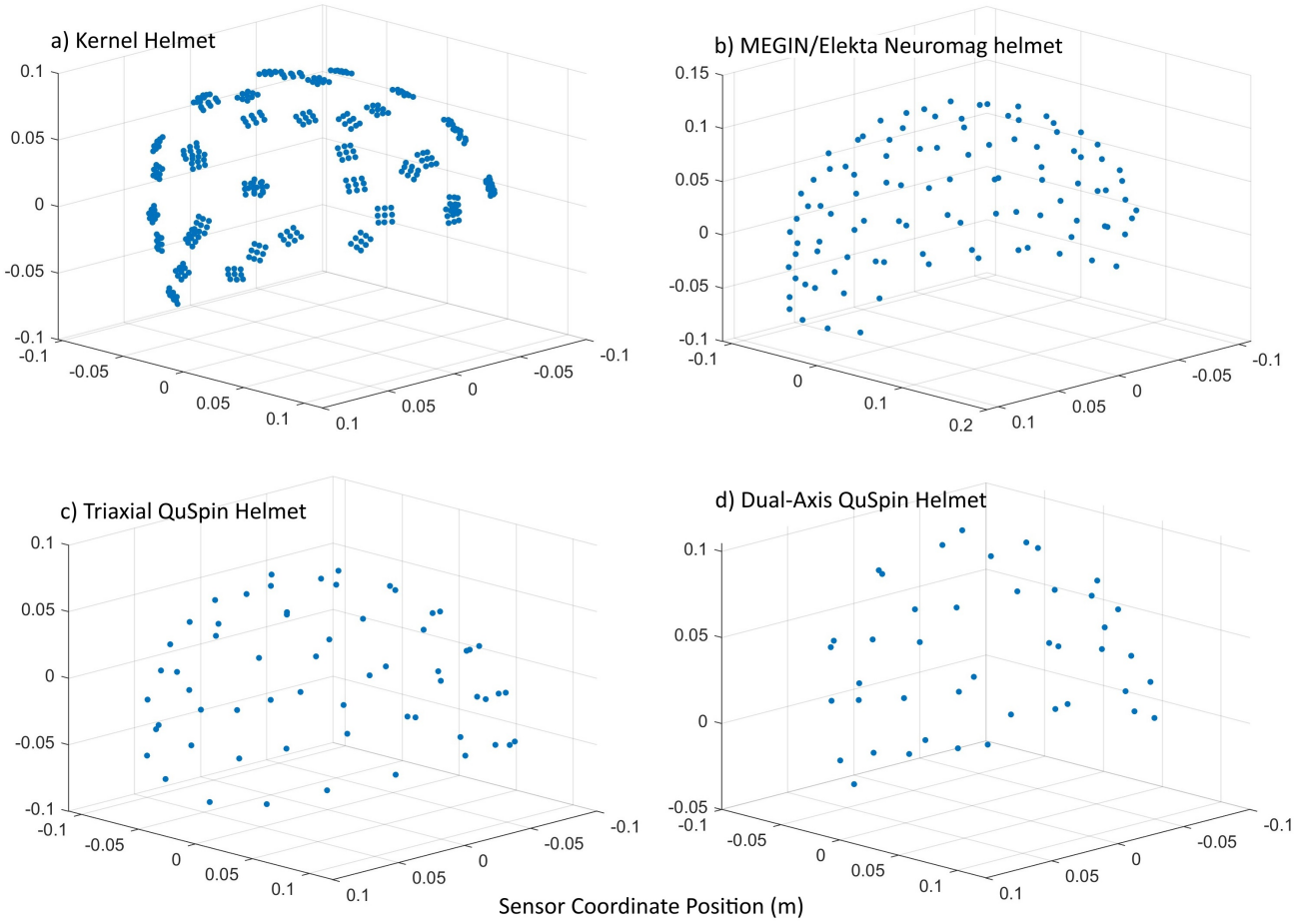

Figure 3.1: Coordinate visualization of the a) 432-Channel Kernel OPM helmet system, b) 306-Channel MEGIN/Elekta Neuromag Helmet, c) 192-Channel Triaxial QuSpin Helmet, and d) 86-Channel Dual-Axis QuSpin Helmet. In a), 349 channels are shown after the removal of bad channels, the full system is 432. In b), the 102 magnetometer and 204 gradiometers are located at the same 102 locations, so 102 coordinate positions are shown. In c) 183 channels are shown after removal of bad channels. The sensor positions are given as (x, y, z) coordinates in space and the sensors are visualized as points.

The ability for each variant to reconstruct the brain signals while minimizing noise is tested on simulated data from a variety of combination of interior current dipole signals, exterior magnetic dipole interference, and simulated noise levels. Finally, each variant is verified with OPM data, specifically an experimental single-subject audio evoked data set

collected with Kernel Flux OPM sensor system, empty-room data collected in a lightly-shielded magnetically shielded room (MSR) with 192-channel third generation triaxial QuSpin Zero Field Magnetometers, and audiovisual data collected with 86-Channel dual-axis QuSpin OPMs at the University College London[42], [23], [47].

3.1 Adjusting the internal SSS basis

3.1.1 A note on Singular Value Decomposition

Singular value decomposition (SVD) is a common linear algebra method to factor a matrix and has been widely used in MEG processing and analysis. The definition of the SVD of matrix $\mathbf{M}$ is given by

$$\mathbf{M} = \mathbf{U}\mathbf{\Sigma}\mathbf{V}^T \tag{3.1}$$

where both $\mathbf{U}$ and $\mathbf{V}$ are a orthogonal matrices by definition and $\mathbf{\Sigma}$ is a rectangular diagonal matrix of singular values along the diagonal [29], [13]. The singular values $\sigma_i = \mathbf{\Sigma}_{ii}$ are uniquely determined by $\mathbf{M}$ and the corresponding singular column vectors of $\mathbf{U}$ form an orthonormal basis that spans the same information as matrix $\mathbf{M}$. The decomposition of singular vectors are ordered by largest singular value to least, where the largest singular vectors contain more similar information to matrix $\mathbf{M}$ than the smallest values.

This technique has a wide variety of applications to MEG data processing and SSS methods. For example, singular values can be used to determine metrics like the condition number of a matrix by taking the ratio of the largest to smallest nonzero singular values of the SVD decomposition of $\mathbf{S}$ [29]. The condition number can serve as a metric of stability in the face of noise of the internal data reconstruction and is further discussed and implemented in Section 4.2 [13]. SVD can also be used as a method to combine two matrices into one that contains the same information in a more compact manner. For example, taking the SVD of a matrix $\mathbf{M} = [\mathbf{N}, \mathbf{M}]$ will result in an orthogonal matrix $\mathbf{U}$ which spans the same basis as $\mathbf{N}$

and **M** combined, by definition, in a more compact form. Matrix combination using SVD has been used in methods like extended SSS (eSSS) and is further explored as the methodology behind mSSS in Section 3 [17], [29].

3.1.2 Two Sphere Expansion

We construct mathematical expansion bases using multiple overlapping spherical sets which can be optimized to have origins and radii such that none of the brain is left out while the extent of the spheres is significantly far enough away from the sensor array that there can be a clearer distinction between interior and exterior signals. Figure 3.2 illustrates the issues with the single-origin VSH basis when calculated using on-scalp systems.

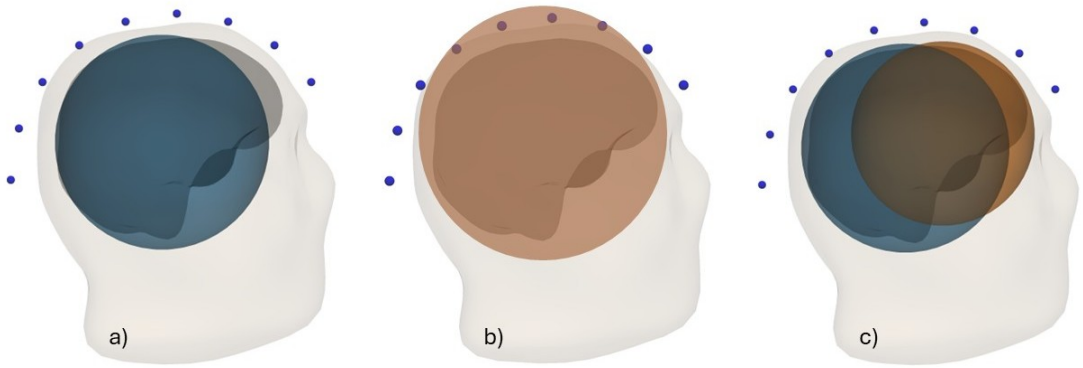

Figure 3.2: Visualization of Case a) the single-origin VSH basis with a sufficiently small expansion radius to be inside of the sensor array, compared to Case b) with the expansion radius large enough to encompass the full brain space but also includes the sensors, and finally Case c) with the two-origin VSH basis expansion where multiple spheres can encompass the full brain space while maintaining enough separation between the spheres (blue and orange) used to illustrate the internal basis expansions and the on-scalp sensors (blue dots).

As seen in Case a) and Case b) illustrated in Figure 3.2, one VSH expansion can no longer fully encompass the interior brain space without also including the sensors within the interior space. Case a) is problematic because we risk missing brain activity in the prefrontal cortex that is not included in the VSH expansion, but expanding the radius in Case b) to include

the missing area of the brain is impossible without including the sensor array within the interior basis. SSS requires that the sensors be located in a source-free volume in order for the VSH expansion of the magnetic field in Equation **??** to be valid, thus Case b) is not a solution to this issue. However, the novel mSSS method in Case c) is able to span the full brain without encroaching on the sensor-space. Using the example subject MRI found on MNE-Python to determine the anatomically meaningful region of the brain, the centers and radii of two separate VSH expansions were optimized to encompass the whole brain with the minimum possible radius [31], [14]

The methodology for combining multiple spherical bases into one interior basis spanning the brain space is motivated by the basis augmentation described eSSS [17]. The eSSS method adds components to the external SSS basis that are not accurately modeled by the external VSH expansion. Such components may include, e.g., vibration artifacts that cannot be modeled as a common-body vibration of the whole MEG system. For eSSS to be successful, it is beneficial to have reference data from which such interference components can be determined statistically, for example by the Principal Component Analysis (PCA). We can use the method of developing the eSSS matrix to combine the two-origin interior $\mathbf{S}$ matrices into one basis through the SVD of the concatenated interior vector spherical harmonic bases

$$[\mathbf{S}_{in,1}, \mathbf{S}_{in,2}] = \mathbf{U}\mathbf{\Sigma}\mathbf{V}^T \tag{3.2}$$

where $\mathbf{S}_{in,1}$ is the normalized SSS basis constructed with one expansion origin and $\mathbf{S}_{in,2}$ is the normalized SSS constructed with a second, different expansion origin. In principle, this method of combination can be extended to any number of spherical basis sets necessary to encompass the brain space, but we focus on the two-origin implementation. The matrix $\mathbf{U}$ contains the left singular vectors which span the same space as the two interior SSS matrices as defined in Section 2.3, creating the multi-signal space separation (mSSS) method when combined in this fashion. In order to improve stability of the augmented matrix, the column number of the mSSS basis is reduced by only keeping the most significant i column vectors

of $\mathbf{U}$ that are above a significance threshold defined using the ratio of each singular value σ_i to the greatest singular value σ_1. For our purposes, if the ratio $R = \sigma_i/\sigma_1$ is greater than the significance threshold, then the column vector corresponding to σ_i is deemed statistically and significantly relevant to span the brain-space and is included in the total interior basis. Based on the investigations conducted with the optimized centers and sensor geometries, the threshold is set to $R = 0.005$, or 0.5% of the maximum significant value. In this fashion, the mSSS basis is constructed

$$\mathbf{S}_m = [\mathbf{U}_{1:i}, \mathbf{S}_{out}] \tag{3.3}$$

where $\mathbf{S}_{out}$ is the exterior SSS basis constructed with single-origin VSH as discussed in Section 2.1. The exterior signals are not constrained by the sensor geometry specifications or biological considerations, so one exterior $\mathbf{S}_{out}$ basis constructed with one, single-origin VSH expansion with the origin set as the device origin is satisfactory. The mSSS basis matrix $\mathbf{S}_m$ can then be used in the same way as the $\mathbf{S}$ matrix to reconstruct the measured signal vector $\boldsymbol{\phi}$

$$\boldsymbol{\phi} = \mathbf{S}_m \mathbf{x} \tag{3.4}$$

As a result of the threshold, the dimensions of the mSSS basis is variable depending on the specific sensor geometry used. For example, the dimension of the mSSS basis for the 306-Channel MEGIN/Elekta Neuromag system is 306×115, which is larger than the typical SSS basis with 80 internal components. This feature allows the mSSS basis to be more dynamically stable depending on the number of kept components, and the multi-origin model can be adapted and optimized to a variety of MEG systems. Generally, the extra vectors in the mSSS provide additional information. It is expected that when the sensors are closer to the head, the number of degrees of freedom detected by MEG increases, which is consistent with the increased dimensionally of the mSSS basis, and containing the full internal brain-space may require more components. Any risk of overfitting the internal space

is mitigated by the SVD method for creating the mSSS basis, where only components above the significance threshold are kept. For a deeper investigation on the dimensionality of the internal mSSS basis and threshold adjustment for low-channel count systems, see Section 6.3.

3.1.3 Prolate Spheroidal Harmonics

Prolate spheroidal harmonics are solutions to Laplace's equation in spheroidal coordinates and have historically been used for a variety of problems in physics as solutions to wave equations and eigenfunctions in signal processing techniques [49],[1]. More recently, spheroidal harmonics have been implemented in the context of modeling gravitational fields and irregular celestial objects [12], [44]. The motivation for modeling the brain using spheroidal harmonics over spherical is similar to the applications in gravitational fields as the geometries of both systems are similar and can be described with spheroids. In order to combat issues with spherical OPM expansions, multipole expansions can be performed with prolate spheroidal harmonics to encompass more of the brain without encroaching on the locations of the OPM sensor array [56]. Prolate spheroidal harmonics satisfy the magnetic field presented in Equation (2.20) and are proportional to spherical harmonics when the origin for the expansion is centered at zero.

$$\mathbf{B}(r_{maj},\theta,\phi) = -\mu_0 \sum_{l=0}^{\infty}\sum_{m=-l}^{l} \alpha_{lm} \nabla \left[\frac{Q_l^m\left(\frac{r_{maj}}{c}\right)}{Q_l^m(\frac{a}{c})} S_{lm}(\theta,\phi) \right] - \mu_0 \sum_{l=0}^{\infty}\sum_{m=-l}^{l} \beta_{lm} \nabla \left[\frac{P_l^m\left(\frac{r_{maj}}{c}\right)}{P_l^m(\frac{a}{c})} S_{lm}(\theta,\phi) \right] \tag{3.5}$$

Instead of Y_{lm}, spheroidal harmonics are constructed using the first and second Legendre functions, P_l^m and Q_l^m, and the real counterpart of the complex Y_{lm} harmonics, S_{lm}. The geometry is defined with a as the major axis of the reference spheroid, b as the minor axis, and the focus $c = \sqrt{a^2 - b^2}$. As c approaches zero, the spheroidal harmonics becomes proportional to spherical harmonics. From the reference sphere, we can define r_{maj} is the spheroidal axis coordinate of the sensors: (r_{maj}, θ,ϕ). Prolate spheroids are based on a modified radius r_{maj} defined as:

$$r_{maj} = \sqrt{\frac{r^2 + c^2 + \sqrt{(r^2 + c^2)^2 - 4z^2c^2}}{2}} \tag{3.6}$$

with r being the spherical definition $r = \sqrt{x^2 + y^2 + z^2}$. These new coordinates allow us to redefine the spheroidal angles:

$$\begin{aligned} \phi &= \arccos \frac{z}{r_{maj}} \\ \theta &= \left(\arctan \frac{y}{x}\right)^2 \end{aligned} \tag{3.7}$$

These coordinates are visualized in Figure 3.3 for reference.

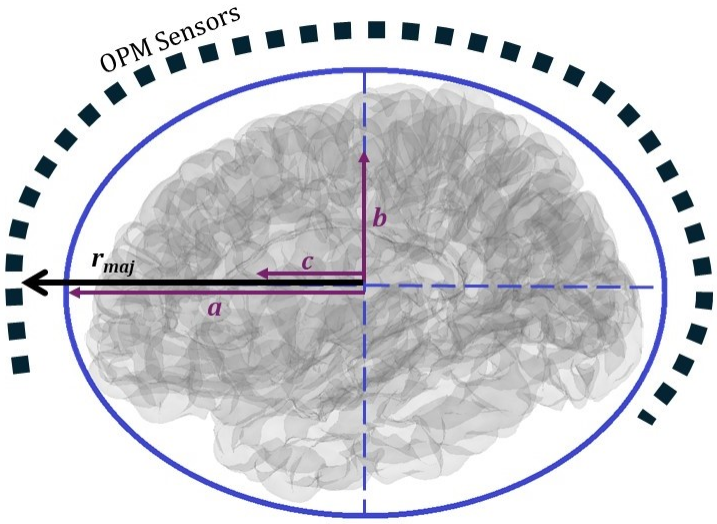

Figure 3.3: Visualization of the coordinate axes used to create the spheroidal harmonic expansions

The magnetic signal can be reconstructed by applying prolate spheroidal harmonics in a similar fashion to SSS

$$\boldsymbol{\phi} = \mathbf{H}\boldsymbol{\gamma} = \begin{bmatrix} \mathbf{H}_{in} & \mathbf{H}_{out} \end{bmatrix} \begin{bmatrix} \boldsymbol{\gamma}_{in} \\ \boldsymbol{\gamma}_{out} \end{bmatrix}. \tag{3.8}$$

where we use the harmonic matrix $\mathbf{H}_{in}$ and multipole weights $\boldsymbol{\gamma_{in}}$. In this fashion, the data can be split into three spatial regions corresponding to the proximity of the data signals to the sensors. The intermediate signals can further be associated with the interior or exterior basis using temporal correlations. We focus on the harmonic matrix $\mathbf{H}$ itself and its comparisons with the traditional $\mathbf{S}$ matrix generated in signal space separations based on the VSH functions. In previous applications, the spheroidal harmonics are implemented by keeping $L_{out} = 2$ components in the exterior sum, with sensor systems simulated as point magnetometers, and radial sensing directions [56]. To consistently compare each SSS variant, we implement the spheroidal harmonics with $L_{out} = 3$ and change the sensor type and orientation to match the different systems investigated.

3.1.4 Augmented Spheroidal Basis

In addition to mSSS, this Chapter offers a novel adaptation of the prolate spheroidal harmonic implementation that simplifies the basis computation by using vector spherical harmonics to reconstruct the external signals. The merit of using prolate spheroidal harmonics for the interior SSS basis comes from the biological geometry of the brain itself, but the exterior basis does not need to be defined by spheroidal geometry. The internal spheroidal harmonic basis can be combined with the external spherical harmonic basis in the same fashion as detailed in Section 2,

$$\boldsymbol{\phi} = \begin{bmatrix} \mathbf{H}_{in} & \mathbf{S}_{out} \end{bmatrix} \begin{bmatrix} \boldsymbol{\gamma}_{in} \\ \mathbf{x}_{out} \end{bmatrix}. \tag{3.9}$$

Where $\mathbf{H}_{in}$ is the internal prolate spheroidal harmonic basis with corresponding multipole weights $\boldsymbol{\gamma}_{in}$ and $\mathbf{S}_{out}$ is the vector spherical harmonic exterior basis with weights $\mathbf{x}_{out}$ calculated with the same origin and methodology as with SSS and mSSS.

3.2 Comparison Methodology and Metrics

3.2.1 SSS Variants

We first investigate the novel mSSS variant, which uses the novel multi-origin VSH (mVSH) implementation for the interior basis combined with single-origin VSH (sVSH) for the exterior, abbreviated mVSH/sVSH for the in/out expansions. We next replicate the spheroidal implementation for both interior and exterior basis, abbreviated to Spheroid/Spheroid. Finally, we implement a novel modified version of the spheroidal variant which combines spheroidal harmonics for the interior expansion and single-origin SSS for the exterior, abbreviated Spheroid/sVSH. All three variants are compared with single-origin SSS as outlined in Section 2.1, abbreviated sVSH/sVSH. Additionally, all harmonic expansions are calculated up to order $l = 8$ for the interior basis and $l = 3$ for the external basis.

Each SSS variant was implemented using a variety of established and novel MEG systems. First, we implement the traditional 306-channel MEGIN/Elekta Neuromag helmet array using the specification detailed in MNE-Python [31]. The 306-channel system contains 102 magnetometers and 204 gradiometers with the sensing direction of each sensor perpendicular to the plane defined by the pick-up loop. Additionally, a simulated OPM system was implemented using the 102 magnetometer channels from the MEGIN/Elekta Neuromag geometry with the same position and orientation. Next, we implement the Kernel Flux OPM system containing 349 OPM channels with coil sensing directions oriented perpendicular to the surface of the subject's head. The complete system contains 432 magnetometers, but after elimination of bad channels, 349 channels are used for the purposes of this investigation [31], [42]. Along with using the geometry of the Kernel system for each SSS variant with simulated data, we also test each SSS variant using auditory evoked data collected with the Kernel system. Finally, each SSS variant is implemented using 64 third generation triaxial QuSpin Zero Field Magnetometers in a lightly shielded magnetic room with data from a single participant performing right index finger abduction [23].

For consistency, here we implement spherical harmonics using the same external order, $L_{out} = 3$, as with the other SSS variants. The implementation of spheroidal harmonics only considers magnetometers, so when implemented with the MEGIN/Elekta Neuromag sensor system, we use the full 306-channels as well as only 102 magnetometers when calculating the spheroidal harmonics basis [56]. Similarly, when the augmented spheroidal/sVSH basis is implemented using the MEGIN/Elekta Neuromag geometry, one case is constructed with the full helmet and the other with only the 102-magnetometer channels to create both the $\mathbf{H}_{in}$ and $\mathbf{S}_{out}$ for a consistent combined basis. OPM sensors are typically modeled as magnetometers, so using the 102-magnetometer channels is a valid simulation to test each SSS variant on a simulated OPM-like system.

The creation of the mSSS basis is implemented in Matlab following the basic methodology and structure of the SSS functions and is used with the same pre- and post-processing steps when applied in a data processing pipeline [53], the most significant extra step required is the calculation of the two origins of the two interior VSH expansions. A typical implementation is to first use the sensor positions and MRI to calculate the optimized centers for the two VSH origins using MNE-Python. Next, calculate two interior SSS matrices, one for each origin, following the implementation details of SSS in Matlab, then combine into one interior mSSS basis using SVD and the thresholding process described in Section 3.1. Then, calculate one exterior SSS basis using the origin of the system. Then, the combined interior and exterior basis can then be used in the same fashion as the SSS method to estimate the multipole moments and reconstruct the internal brain signals as detailed in Section 2.1. Further implementation details and examples for constructing the mSSS basis on a variety of sensor systems and processing with data can be found online on GitHub, including details on where to locate the datasets and spheroidal harmonic functions used in this study.

3.2.2 Metric Comparisons

The ability of the SSS basis to functionally reconstruct the internal brain signal while removing any exterior signals can be quantified by various metrics and simulations. First, the

condition number of the basis details the stability of the SSS matrix, which can impact the reconstruction of the signal. Unstable matrices can amplify noise when inverted, diminishing the ability to accurately describe the internal signals.

Another common method for assessing the content and magnitude of a matrix is the Frobenius norm. For a rectangular matrix $\mathbf{A}$, the Forbenius norm is defined as [18], [48]:

$$||\mathbf{A}||_F = \sqrt{\sum_{i=1}^{m}\sum_{j=1}^{n}|a_{ij}|^2} = \sqrt{\mathrm{Tr}(\mathbf{A}^\dagger\mathbf{A})} \tag{3.10}$$

Here, the matrix $\mathbf{A}$ is calculated by finding the pairwise subspace angle (in radians) between each column of the interior SSS matrix for each variant, resulting in a square diagonal matrix with dimensionality equal to the number of harmonic order components kept and zero elements along the diagonal. Off-diagonal elements with pairwise subspace angles closest to 90 degrees show that the SSS basis contains maximally different information per column, thus, a larger Frobenius norm indicates that more different and relevant information is contained in the SSS basis

Next, in order to gain understanding of the level of similarity between each SSS expansion variant, we calculate the mean, minimum, and maximum principle angles arising from the subspace angle comparison between two SSS matrices up to the first 80 components, which is the typical dimension of the full SSS basis when $L_{in} = 8$ and $L_{out} = 3$ components of the vector spherical harmonic sums are kept. This is done using built-in functionality in Matlab where the subspace angle is specifically calculated between each vector of one basis and the full second basis. Mathematically, this calculation is the same as finding the principle angles between two matrices, but here we refer to them as subspace angles to maintain consistency with the naming of the Matlab function implementation [30], [13].

Finally, the minimum, mean, and maximum subspace angles are calculated to quantify the difference between each SSS basis and the data, both simulated and from human subjects. The angles are calculated between the full SSS basis matrix and the full data matrix for all

channels over all time points in a the same fashion as described above. A smaller angle means the two bases are more linearly dependent, which indicates a better match between the basis and the data, or a better ability to span the interior brain space to accurately reconstruct the brain signals.

3.2.3 Dipole Simulations

The condition number of the SSS basis does not necessarily correlate directly with the ability of the basis to reconstruct the internal signal. The ability of each SSS variant to reconstruct brain signals was tested with simulated data generated from a variety of different dipolar magnetic sources. We can begin with the equation for a magnetic dipole

$$\mathbf{B}_{dip}(\mathbf{r}) = \frac{\mu_0}{4\pi r^3}\left[3(\mathbf{m}\cdot\hat{\mathbf{r}})\hat{\mathbf{r}} - \mathbf{m}\right] \tag{3.11}$$

where $\mathbf{r}$ is the vector from the dipole to the location of each sensor in direction $\hat{\mathbf{r}}$, and $\mathbf{m}$ is the dipole moment. The magnetic flux through each of the 306 SQUID sensors in the MEGIN/Elekta Neuromag system was calculated as

$$\Phi_i = \int_{\mathbf{A}_i} \mathbf{B}_{dip}\cdot \mathrm{d}\mathbf{A}_i \tag{3.12}$$

where $\mathbf{A}_i$ is the area of the coil loop using standard gradiometer and magnetometer dimensions for SQUID sensors given in the MNE-Python documentation [31]. When numerically implemented, integration can be approximated over 9 points for magnetometers and 8 for gradiometers using a weighted numerical integration method [53]. Following this same procedure, the OPM sensors are modeled using the same 9-point integration method as a SQUID magnetometer, and the flux through gradiometers simulated here is calculated using 8 integration points. The implementation of the spheroidal harmonics used as the basis for one of the SSS variants discussed here only accounts for magnetometers, unlike the SSS and mSSS implementations, which are adapted to both gradiometers and magnetometers with the aforementioned loop integration method.

In order to model human brain signals specifically, each SSS variant was also tested using simulated data from one current dipole inside the brain. Current dipoles are a more accurate representation of human MEG data because they match the form of the primary current originating from neurons, completed by a distribution of volume currents that are shaped by the geometry of the electric conductor structure of the head. In the case of a spherically symmetric conductor, the forward field of a current dipole has an analytical form [45]:

$$\mathbf{B}(\mathbf{r}) = \frac{\mu_0}{4\pi F^2}\left(F\mathbf{Q} \times \mathbf{r}_0 - \mathbf{Q} \times \mathbf{r}_0 \cdot \mathbf{r}\nabla F\right) \tag{3.13}$$

$\mathbf{Q}$ is the current dipole defined as the primary current confined to a single point, where $\mathbf{r}$ is the vector from the origin to the location of each sensor, $\mathbf{r}_0$ is the location of the current dipole, and F is defined as $F = a(ra + r^2 - \mathbf{r}_0 \cdot \mathbf{r})$ with $\mathbf{a} = \mathbf{r}_0 - \mathbf{r}$ [45]. The magnetic flux measured by each SQUID or OPM sensor was calculated as detailed in the single magnetic dipole simulation.

We implement three different dipole simulations. One with a single interior current dipole source, one with a combination of an interior current dipole and exterior magnetic dipole simulating external noise, and a third with Gaussian noise added to the superposition of internal current dipole and external magnetic dipole signal with a value of 15 percent of the internal signal at each time point. Each simulation was generated using the same parameters. The signals are generated for 1 second with a timestep of 0.001 seconds. The internal and external signals are generated with different and varying frequencies with the internal varying faster than the external signal to both represent a realistic scenario and make it easier to visually distinguish between the two signals.The Gaussian noise is generated in Matlab with a constant seed, thus there is no need for different trials per simulation type as the results remain consistent.

3.2.4 Sensor Deviation Simulation

To demonstrate the adaptability of mSSS, two-origin mSSS and SSS are constructed using 306 magnetometers where each location has three orthogonal sensing directions based on the

MEGIN/Elekta Neuromag 306-channel SQUID helmet. The top sensors are deviated inward by 3 cm to simulate variable on-scalp placements as seen in Figure 3.4. Data is simulated with various equivalent interior current dipole positions from 4-7 cm radially outward from the center of the spherical conductor in the x-y plane in order to simulate brain signals originating from the motor cortex, giving a response representing a human subject sensory stimulus that induces motion, such as single finger abduction, specifically when the dipole is in the 5cm-7cm distance range. To simulate exterior interference, a magnetic dipole located at 1.5 m in the z-direction was added. This is not an exactly practical scenario but it offers a robust demonstration of the characteristics of the SSS variants in a geometry where a single sphere bounded by the sensor array may not be able to capture all of the brain volume.

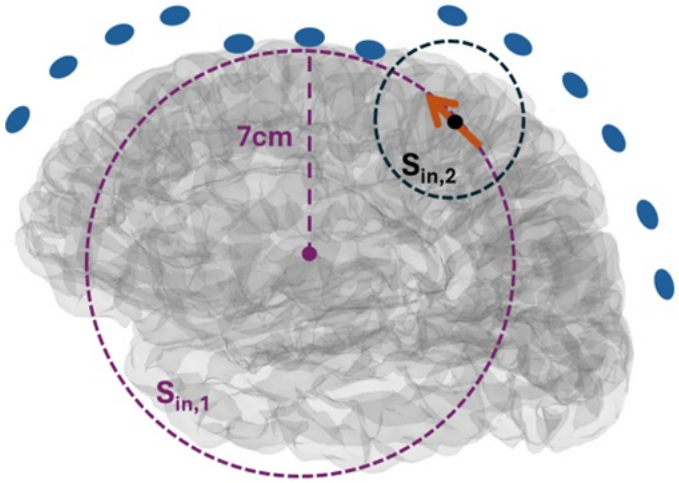

Figure 3.4: Visualization of the sensor deviation simulation where the top eight sensors (blue dots, cross sections shows 3) have been deviated radially inwards by 3 cm. The location of the simulated interior current dipole is placed at the same radius (7 cm) as the closest sensors. The origin of the first VSH labeled $\mathbf{S}_{in,1}$ is placed at the center of the system and the second VSH basis $\mathbf{S}_{in,2}$ is placed with an origin at the location of the current dipole.

For this demonstration, we used a modified methodology for obtaining the mSSS interior basis. The origin of the first VSH expansion is placed at the center of the system, and the second is placed at the location of the interior current dipole. Only the first $L_{in} = 1$

components of the second expansion are kept to lower the dimensions of the $\mathbf{S}$ matrix and improve stability. The two expansions are combined using orthonormal concatenation, $\mathbf{S}_m = \text{orth}([\mathbf{S}_{in,1}, \mathbf{S}_{in,2}])$. This mSSS basis is compared to the traditional SSS basis for each interior dipole location.

3.2.5 Lead Field Implementation for the Internal Basis

The forward problem in MEG calculates the expected magnetic field measured by the sensors for a given primary current source in space and is used as a way to interpret potential brain signals with varying complexities of conductivity profiles and head models. The signal measured by each sensor over time, $\mathbf{y}_i(t)$, is a function of the lead field, $\mathbf{L}(\mathbf{r})$, and the primary current, $\mathbf{J}^P(\mathbf{r}, t)$ as follows [29]:

$$\mathbf{y}_i(t) = \int_V \mathbf{L}_i(\mathbf{r}) \cdot \mathbf{J}^P(\mathbf{r}, t) dV \tag{3.14}$$

In this sense, the MEG measurements are the projection of the primary current into the discretized sensor space. The lead field, $\mathbf{L}(\mathbf{r})$, itself can be calculated using a variety of different head geometries and space discretization methods. Here, we implement a spherical conductor model with discretization based on seven layers of spherical surfaces with 600 points each. The lead field is calculated at each point in space as the origin of a current dipole, based on the Sarvas equation detailed earlier, with three different iterations of the moment [45]. The measured magnetic flux from the lead field dipole is then calculated through the 306-channel MEGIN/Elekta Neuromag helmet using the numeric integration method for gradiometers and magnetometers as discussed in the Dipole Simulation Section 4.3. The signal measured at each sensor, $\mathbf{y}_i$ becomes a matrix over all sensors $\mathbf{Y}$ representing the lead field basis.

The lead field basis spans the same internal brain space as the interior SSS basis, which to reiterate is a representation of the measured MEG data ϕ in matrix notation: This form of $\boldsymbol{\phi}$ can be expressed in matrix notation as:

$$\boldsymbol{\phi} = \mathbf{S}\mathbf{x} = \begin{bmatrix} \mathbf{S}_{in} & \mathbf{S}_{out} \end{bmatrix} \begin{bmatrix} \mathbf{x}_{in} \\ \mathbf{x}_{out} \end{bmatrix}. \tag{3.15}$$

$\mathbf{S}$ is the magnetic subspace containing separate subspaces for internal and external sources, and the corresponding multiple moments are contained in vector $\mathbf{x}$, with L moments of the interior and exterior expansions truncated at $L_{in} = 8$ and $L_{out} = 3$ as detailed in Section 2.1 [53]. We can compare the calculated lead field basis $\mathbf{Y}$ with each interior SSS variant basis ($\mathbf{S}_{in}$, $\mathbf{S}_{m,in}$, and $\mathbf{H}_{in}$) to investigate how well each variant encompasses the full interior basis by calculating the subspace angle between the two.

3.3 Results

3.3.1 Metric Comparisons

The condition numbers for the interior and interior/exterior combinations for each of the SSS variants were calculated for both sensor systems for comparison.

Table 3.1: Condition number of the internal and full SSS matrices for single origin VSH, spheroidal harmonics, and the three combination variants

SSS variant	306-SQUID	102-SQUID	432-Kernel OPM	192-QuSpin OPM
sVSH Interior	153	2460	377	364
mVSH Interior	1.00	1.00	1.00	1.00
Spheroidal Interior	5630	5630	139	110
sVSH/sVSH	186	8000	711	552
mVSH/sVSH	80.6	2100	30.1	8.50
Spheroid/Spheroid	2230	2230	280	215
Spheroid/sVSH	5990	1670	267	552

The condition number of the mSSS basis is 1 as seen in Table 3.1, which is expected due to the orthogonal properties of the matrix created during SVD as discussed in Section 2.3. The VSH expansions used in SSS are not orthonormalized in order to maintain the individual multiple moment to be used for signal transformations such as movement compensation [**?**]. mSSS is not needed for SQUID systems, and these systems are the only kind that require movement compensation, so implementing the mSSS basis for on-scalp systems does not result in the loss of any processing capability. For similar reasons, the spheroidal harmonic basis could also be normalized without a loss of information. We expect that the condition number for the spheroidal harmonics implemented with the 306-channel and 102-channel systems is the same because the spheroidal harmonic implementation does not take into account the gradiometers, so the 204-channels in the SQUID system provide redundant information to the basis.

Next, the pairwise angles between the columns of each SSS variant interior basis were calculated, and the Forbenius norm of the resulting matrix was investigated for two different sensor systems.

Table 3.2: Frobenius norm of the pairwise subspace angles for each interior SSS variant

SSS Variant In	306-SQUID	432-Kernel OPM	192-QuSpin OPM
sVSH	122	116	112
mVSH	180	160	125
Spheroid	122	120	122

Table 3.2 shows the interior mSSS basis has the highest Frobenius norm, indicating that the basis contains more different information in each column of the basis compared to the other SSS variants. In principle, this means the mSSS basis can capture more information about the signals located within the interior space. The Frobenius norm can also give insight into the sensor system's ability to capture information based on the physical geometry. For

example, the Kernel system may result in a smaller Frobenius norm because of the modular design, resulting in physical gaps in the coverage of the brain, which is evident in the lower norm.

A visualization of the pairwise subspace angle matrices used to calculate the Frobenius norm for each basis is included below in Figure 3.5

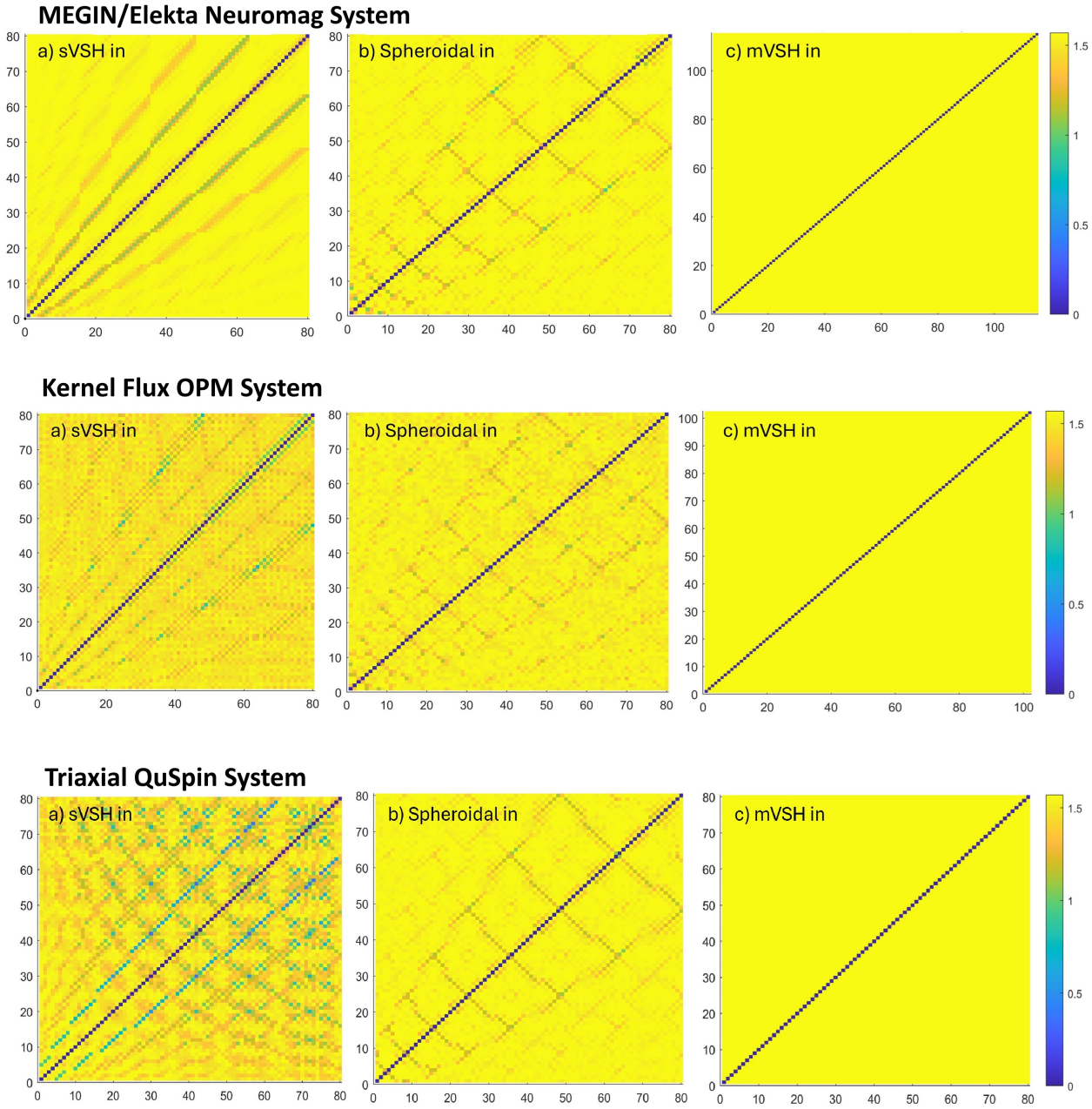

Figure 3.5: Pairwise angles between the columns of each SSS basis calculated using the 306-sensor MEGIN/Elekta Neuromag helmet, 432-channel Kernel Flux Helmet, and 192-Channel Triaxial QuSpin OPM helmet. Angles are in radians, where 1.57 radians is the maximum value possible (90 degrees) and is yellow. Subplot a) shows the interior sVSH (SSS) basis, Subplot b) shows the spheroidal harmonic interior basis, and Subplot c) shows the interior mVSH (mSSS) basis.

Each row of Figure 3.5 shows an upper triangular matrix where each i'th entry is the angle between the i'th column and the j'th column of each interior SSS variant. The diagonal entries are zero (dark blue) as expected, and the largest value is 1.57 radians or 90 degrees (yellow). An angle of 90 degrees indicates that each column in the respective SSS basis contains maximally different information from the next. The patterns of angles less than 90 degrees as seen is this visualizations may lend some insight into the consequences of the sensor geometry itself. For example, in the second set of figures showing the Kernel OPM system, there appear to be clumps and patterns of pairwise angles that are closer together, indicating the information in the nearby basis columns is more similar. This may be a consequence of the modular design of the helmet where sets of sensors are close together with larger gaps in between [42]. More investigation into the pairwise angle and Frobenius norm calculation could help with the optimization of channel location in novel on-scalp MEG systems.

To quantify the difference between each SSS variant, the subspace angle between each basis calculated using the Kernel geometry was calculated and is shown in Table 3.3. The angle between the interior and exterior basis also affects the condition number.

Table 3.3: Minimum, Mean, and Max subspace angle (in degrees) between the three SSS expansion variants.

First Basis Set	**Second Basis Set**	432-Chan Kernel	3cm Deviated 306-Chan
sVSH In	mVSH In	9.02/22.4/60.8	0.143/7.24/35.8
	Spheroid In	0.66/8.48/41.1	31.9/47.3/65.3
mVSH In	Spheroid In	9.85/27.9/57.3	19.7/42.5/58.1
sVSH/sVSH	mVSH/sVSH	0.016/3.77/15.4	2.76e-5/0.02/0.10
	Spheroid/Spheroid	0.831/7.76/21.9	13.9/42.4/65.2
mVSH/sVSH	Spheroid/Spheroid	7.53/23.7/53.7	17.6/42.5/56.9

The sVSH interior basis is the most similar to the spheroidal harmonic interior basis. As

the dimensions of the spheroid approach a sphere, the harmonics simplify exactly to the VSH expansion, so the similarities here in the Kernel system are mathematically expected. As the sensor system becomes less spherical, as with the 3cm-deviated 306 channels system described in the methods section, the spheroidal harmonics and spherical harmonics diverge. This can be seen with the much larger subspace angles between the sVSH combinations and Spheroid combinations in the table. The differences between the sVSH and mVSH basis can come from the orthonormalization process. The angle between the sVSH and mVSH expansions also increases for the deviated sensor system as the addition of the second sVSH expansion in the mVSH combination is able to span space that a the single origin VSH expansion cannot.

When combining two bases together as with the interior and exterior harmonic expansions to create each SSS variant, the subspace angle between the two bases can give some insight into the difference between them. This difference in spanning and information can be affect by the number of harmonic components kept in the expansion, and the type of harmonic expansion of each basis.

Table 3.4: Subspace angle (in degrees) between each interior and exterior harmonic basis combination

SSS Basis Variant	306-Chan SQUID	102-Chan SQUID	432-Kernel	192-QuSpin
sVSH/sVSH	23.1	5.18	51.0	79.0
mVSH/sVSH	20.5	2.51	52.7	82.8
Spheroid/Spheroid	4.48	4.48	48.3	80.4
Spheroid/sVSH	87.1	85.9	51.5	80.4

The largest subspace angles are between the spheroidal harmonic interior basis and the spherical harmonic exterior basis as seen in Table 3.6, likely due to the geometric differences in mathematical construction.

Finally, a note on the dimensions of the mSSS basis. The threshold value for determining

which components to include in the mSSS basis remains constant for each sensor system, but the number of column vectors included in the basis varies as listed in Table 3.5.

Table 3.5: Size of the interior mSSS basis for each different sensor system helmet given in number of channels by number of vector components

Helmet	Size of mSSS basis
306-SQUID	306 × 115
102-SQUID	102 × 93
432-Kernel OPM	348 × 102
192-Triaxial QuSpin OPM	183 × 80
86-Dual-Axis QuSpin OPM	86 × 65

For the Kernel and Triaxial QuSpin systems, the size of the mSSS basis is less than the number of channels. This indicates that these channels have been marked as bad channels and are not used in the construction of any basis throughout this investigation. Given the constant $L_{in} = 8$ and $L_{out} = 3$, the size of all the other interior SSS basis variants have dimensions of number of channels by 80.

3.3.2 A Note on the Subspace Angle Between Interior and Exterior Harmonic Expansions

When combining two bases together as with the interior and exterior harmonic expansions to create each SSS variant, the subspace angle between the two bases can give some insight into the difference between them. This difference in spanning and information can be affected by the number of harmonic components kept in the expansion, and the type of harmonic expansion of each basis.

Table 3.6: Subspace angle (in degrees) between each interior and exterior harmonic basis combination

SSS Basis Variant	306-Chan SQUID	102-Chan SQUID	432-Kernel	192-QuSpin
sVSH/sVSH	23.1	5.18	51.0	79.0
mVSH/sVSH	20.5	2.51	52.7	82.8
Spheroid/Spheroid	4.48	4.48	48.3	80.4
Spheroid/sVSH	87.1	85.9	51.5	80.4

The largest subspace angles are between the spheroidal harmonic interior basis and the spherical harmonic exterior basis as seen in Table 3.6, likely due to the geometric differences in mathematical construction.

3.3.3 Dipole Simulation Results

We begin with the simple case of a single current dipole placed 5cm from the origin on the x-axis and an initial current dipole $\mathbf{Q} = [0, 1, 0]$ along the positive y-axis which oscillates over with variable frequency. Table 3.7 shows the minimum, mean, and maximum subspace angle between the dipole signal vector and each SSS basis for all time points.

Table 3.7: Average Subspace angle (in degrees) between the internal current dipole simulated data and SSS basis for each variant.

SSS Basis variant	306-SQUID	102-SQUID	432-Kernel OPM	192-QuSpin OPM
sVSH/sVSH	0.15	0.02	0.30	0.43
mVSH/sVSH	0.24	8.50e-14	0.67	0.027
Spheroid/Spheroid	56.6	15.4	15.8	7.43
Spheroid/sVSH	16.5	0.11	3.25	7.57

Next, an exterior magnetic dipole was added to simulate external noise with a dipole

moment $\mathbf{m} = [1, 0, 0]$ located at $\mathbf{r} = [0, 0, 1.5m]$. The dipole signals are weighted individually to have approximately the same magnitude.

Table 3.8: Average subspace angle (in degrees) between the internal current dipole with external magnetic dipole simulated data and SSS basis for each variant.

SSS Basis variant	306-SQUID	102-SQUID	432-Kernel OPM	192-QuSpin OPM
sVSH/sVSH	0.12	0.02	0.27	0.40
mVSH/sVSH	0.19	8.98e-14	0.61	0.03
Spheroid/Spheroid	56.4	12.6	14.2	6.95
Spheroid/sVSH	13.6	0.086	2.9	7.02

Note that the small increase in subspace angle between the 102-SQUID and 306-SQUID systems as seen in Table 3.7 and Table 3.8 may be due to differences in magnetometers and gradiometers. The gradiometers are more sensitive to higher spatial frequencies, so any kind of numerical inaccuracies, for example with the VSH truncation or surface integral approximations, affect the gradiometers more than the magnetometers. In both cases, the very small numerical values of the subspace angles seen in the SSS and mSSS results are insignificant, and will not affect the performance of the methods in practice.

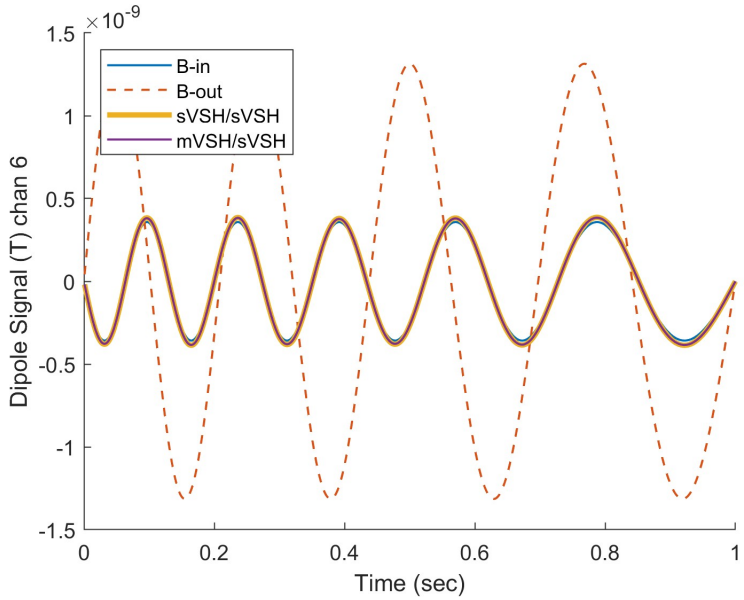

Figure 3.6: Visual comparison of reconstructed data from an interior current dipole located at [5cm,0,0] with an exterior dipole signal located at [0,1.5m,0] using the mSSS and SSS basis with the 306-Channel MEGIN/Elekta Neuromag helmet.

After SSS, the processed data clearly matches the interior current dipole signal, not the exterior signal as seen in Figure 3.7 and evidenced by the low subspace angles for both SSS and mSSS in Table 3.8. This shows that the multi-origin VSH implementation of SSS can successfully suppress exterior interference signals. The spheroidal harmonics produce better results when the sensing direction of the simulated on-scalp sensors are in the $\hat{r}$-direction. Across all of the sensor geometries, augmenting the internal spheroidal harmonic basis with the single-origin vector spherical harmonic exterior produces a better match with the internal data.

Next, Gaussian noise is added to the internal current dipole and external magnetic dipole signal with a value of 15 percent of the internal signal at each time point. Here, we focus on OPM sensor systems, both real and simulated.

Table 3.9: Minimum, Mean, and Max subspace angle (in degrees) between the noisy current dipole simulated data and SSS basis for each variant with OPM systems.

SSS Basis variant	102-SQUID	432-Kernel OPM	192-QuSpin OPM
sVSH/sVSH	0.0024/1.46/3.96	0.023/6.34/9.57	0.035/3.48/7.30
mVSH/sVSH	7.12e-14/8.95e-14/1.14e-13	0.023/6.34/9.41	0.035/1.88/3.18
Spheroid/Spheroid	0.0023/12.6/18.4	3.61/15.7/21.3	1.43/8.57/13.2
Spheroid/sVSH	0.0015/1.77/5.15	0.025/7.24/10.6	0.036/8.63/13.5

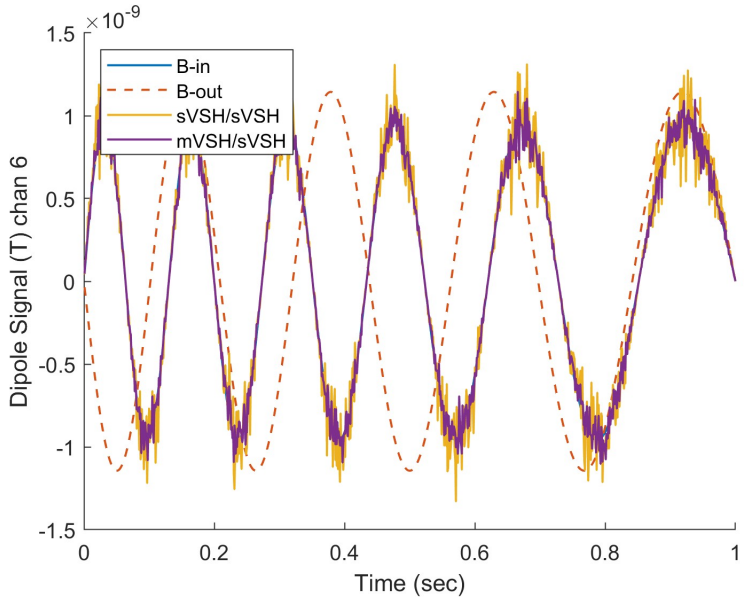

Figure 3.7: Visual comparison of reconstructed data from an interior current dipole located at [5cm,0,0] with an exterior magnetic dipole signal located at [0,1.5m,0] and Gaussian noise at 15% of the peak amplitude using the mSSS and SSS basis with the 192-Channel QuSpin Triaxial OPM helmet.

In the noisy current dipole simulations, the mSSS and SSS basis behave very similarly across all sensor systems, but the mSSS basis can lower the minimum subspace angle in

some cases as seen in Table 3.9, indicating a better match than the other variants with OPM sensor systems. Additionally, this investigation shows that the mSSS remains stable when reconstructing noisy data and can suppress noise more than the SSS basis as seen in Figure 3.7. Across all simulations, the subspace angles between the mSSS reconstruction and the simulated data are very small for the 102-channel magnetometer SQUID system. This could partly be due to the fact that the internal mSSS basis is almost square with dimensions of 102×93, forcing the subspace angle to approach numerical zero. In each case, the augmented spheroidal harmonic basis with sVSH exterior dramatically improves the reconstructed data on both simulated and real OPM systems with noisy simulated data.

3.3.4 Sensor Deviation Comparison Results

For reference, the condition number of each SSS basis calculated using the 306 channel magnetometer sensor system with the top eight sensors deviated radially inward by 3cm as detailed previously are listed in Table 3.10.

Table 3.10: Condition number of the internal and full SSS matrices for single origin VSH, spheroidal harmonics, and the three combination variants

SSS variant	sVSH/sVSH	mVSH/sVSH	Spheroid/Spheroid	Spheroid/sVSH
Condition Number	1460	20.3	425	387

The condition number for the mSSS basis is expected to be very low due to the modifications made to the calculation of the second VSH basis as discussed in the Methodology section.

Table 3.11: Average subspace angle between each SSS variant and the interior current dipole data for increasing radial positions with 306-point magnetometer, sensor deviated helmet.

SSS Basis variant	1cm	3cm	5cm	7cm
sVSH/sVSH	1.78e-7	0.002	0.27	6.62
mVSH/sVSH	0.006	0.004	0.17	0.95
Spheroid/Spheroid	15.0	22.6	33.2	41.6
Spheroid/sVSH	12.3	19.5	30.5	39.2

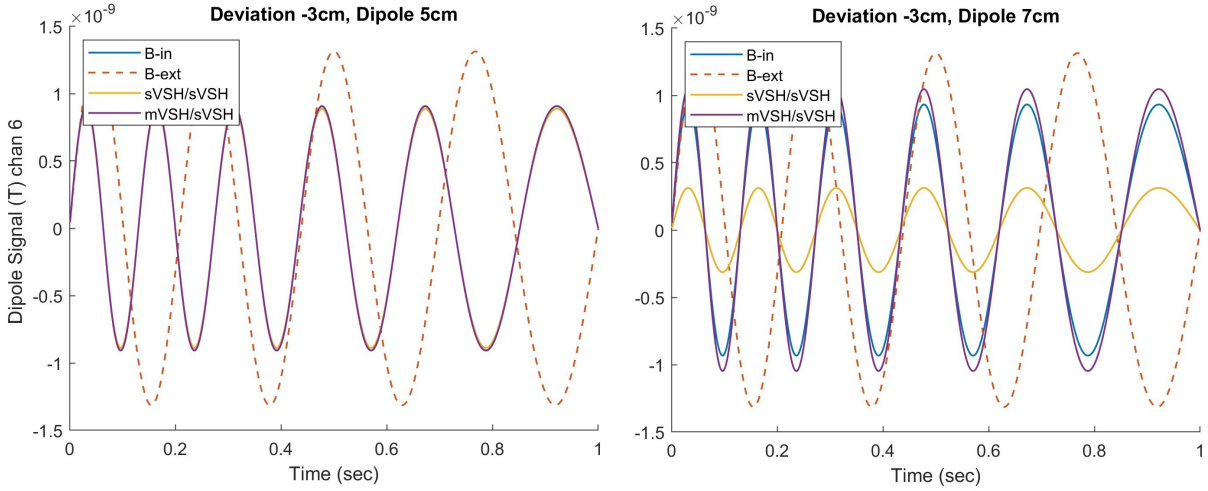

Figure 3.8: Visual comparison of reconstructed data from an interior current dipole with an exterior dipole signal using the mSSS and SSS basis with the top 8 sensors deviated inwards by 3cm. The location of the current dipole is moved from 5cm away (left panel) from the origin to 7cm away from the origin (right panel).

When the dipole is closest to the most inward sensor, at 7cm, the angle between the SSS basis is 14 degrees, compared to mSSS which stays very low regardless of dipole location as seen in Table 3.11, indicating a better reconstruction. The mSSS basis visually matches interior dipole signal at 7cm where single origin basis does not as seen in Figure 3.8. The

inability of the SSS basis to reconstruct the full signal is confirmed by a sharp increase in the subspace angle between the SSS basis and the dipole signal when the dipole is moved from 5cm to 7cm, indicating that some of the signal can no longer be encompassed by the SSS basis. Thus, mSSS is better suited for sensor systems with variable/nonuniform sensor positions at different distances from the origin, especially when the interior signal source is aligned along the same axis as the sensor deviation and when the signal originates near the closest sensor. Additionally, this simulation exemplifies the effectiveness of mSSS to process brain signals that originate from the motor cortex.

3.3.5 Lead Field implementation results

The subspace angle between the interior basis for each SSS variant and the lead field basis was calculated by comparing each column of the SSS interior basis with the full lead field matrix and are shown in Table 3.12. The lead field and SSS basis were all constructed using the 306-Channel MEGIN/Elekta Neuromag system detailed on MNE-Python [31].

Table 3.12: Average subspace angle between the interior SSS basis for each variant and the lead field basis

SSS Variant In	Subspace angle (degrees)
sVSH	6.82e-14
mVSH	7.14e-14
Spheroid	5.83e-14

All of the interior SSS variants match the lead field basis extremely well as indicated by the very low subspace angles. No one is meaningfully better than the others in this metric comparison, but the results show that each basis successfully spans the interior brain space and all possible fields generated by interior current dipoles.

3.4 Verify with OPM Subject Data

3.4.1 Lightly Shielded MSR with QuSpin OPM system

Each SSS construction was tested using data collected in both a standard 5-Layer MSR and a lightweight MSR in order to investigate the abilities of each basis to reduce noise and external interference. Previously acquired empty-room data was collected at the University of Nottingham using 64 third generation triaxial QuSpin Zero Field Magnetometers, comprising a total of 192 channels, in a lightly shielded MSR constructed of one layer of MuMetal and one layer of copper [23]. After removal of bad channels, 183 channels are used.

The mSSS basis is implemented with the expansion origins for the two VSH bases using the optimized centers obtained with MNE-Python as described in Section 3.1. The raw data was processed using each SSS variant, and the subspace angle between each SSS basis and the data was calculated to check the data and processing. In addition, the power spectral density (PSD) of each data reconstruction is compared to the raw data to investigate the noise reduction capabilities.

Table 3.13: Minimum, Mean, and Maximum Subspace angle (in degrees) between the QuSpin OPM raw data and SSS basis for each variant.

Data Type	5-Layer MSR	Lightweight MSR
sVSH/sVSH	8.72/10.1/12.1	7.77/10.87/13.50
mVSH/sVSH	7.92/9.99/11.7	7.44/11.61/14.11
Spheroid/Spheroid	8.34/11.3/16.4	9.42/11.40/15.06
Spheroid/sVSH	7.10/8.09/11.8	8.90/10.40/12.88

The subspace angles seen in Table 3.13 between each SSS variant and the reconstructed data are all slightly higher than would be expected from previous results. One possible explanation for this is inaccurate system calibration, which has been quantified [19]. Despite

this systematic issue, the subspace angle results still confirm adequate matching between each basis and the data.

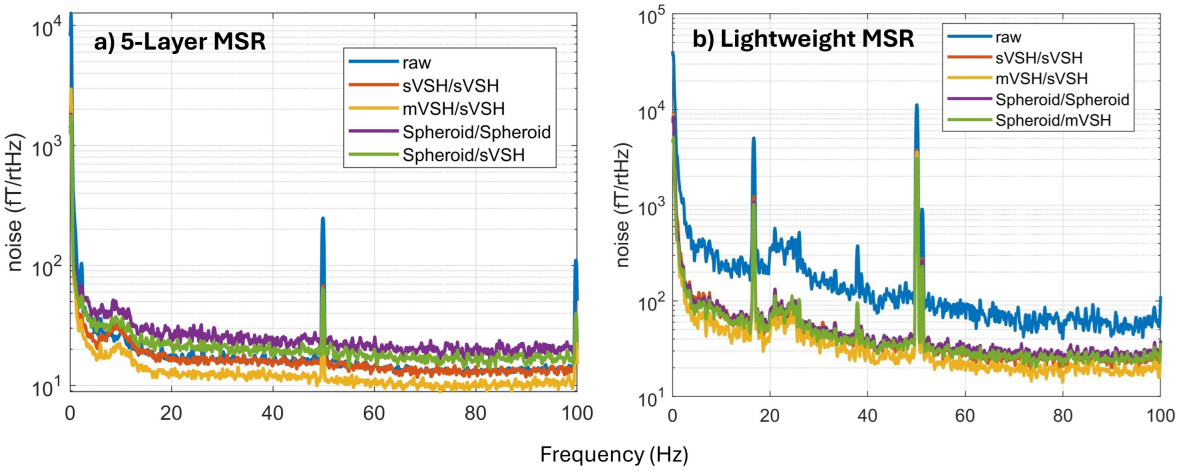

Figure 3.9: Reconstructions of QuSpin 192-channel OPM empty-room data with a) 5-Layer MSR and b) lightly shielded MSR. Data was collected at the University of Nottingham and was processed using each SSS variant with varying VSH expansion origins for the mSSS method.

Each of the SSS variants shows ability to lower the noise floor of the collected data successfully. The mSSS method has the lowest minimum subspace angle of any variant. Visually, in Figure 3.9, the mSSS basis lowers the noise floor of the data more than the other variants in both the 5-layer MSR and Lightweight MSR, highlighting its capabilities with a variety of different MSR setups. Additionally, using the augmented spheroidal harmonic basis with the single-origin VSH exterior improves the reconstruction of the data as seen by a reduction in the subspace angle between the basis and the data.

3.4.2 Kernel Flux OPM Data

Each of the SSS reconstruction variants was used to process the Kernel Flux OPM data, collected at the University of Washington (UW) using 432 channels with coil sensing directions oriented perpendicular to the surface of the subject's head. Single-subject audio response data

were collected using the Kernel Flux OPM system in accordance with the UW institutional review board (IRB) human subjects testing guidelines [34]. After the exclusion of bad channels, 349 channels were kept for analysis. We focus on the evoked data, approximately 1 s long, averaged over 180 trials of the audio tone response, obtained using epoching and evoked preprocessing functions in MNE-Python [31]. First, we compare the minimum, mean, and maximum subspace angle between the evoked data and each SSS basis in Table 3.14.

Table 3.14: Minimum, Mean, and Maximum Subspace angle (in degrees) between the Kernal OPM Evoked data and SSS basis for each variant.

SSS Basis variant	349-Channel ($\hat{r}$)
sVSH/sVSH	6.43/13.0/32.7
mVSH/sVSH	5.53/12.4/30.6
Spheroid/Spheroid	6.74/13.3/32.4
Spheroid/sVSH	6.72/12.7/31.6

Each SSS basis variant reconstructs the raw data similarly as indicated by the range of subspace angles, between 5.53° and 31.6° as seen in Table 3.14. In this case, the mSSS matches the raw data the best with an average subspace angle of 12.4° and a minimum angle reduction by about 1° over the single-origin SSS method. Next, we calculate the signal-to-noise ratio (SNR) by taking the ratio of the average standard deviation of peak signal over 0.1 seconds and the average standard deviation of the noise over the first 0.1 seconds of data collection.

Table 3.15: Signal to Noise Ratio of the evoked and SSS processed Kernel OPM data.

Data Type	349-Channel ($\hat{r}$)
Evoked Data	3.81
sVSH/sVSH	4.50
mVSH/sVSH	4.50
Spheroid/Spheroid	4.29
Spheroid/sVSH	4.59

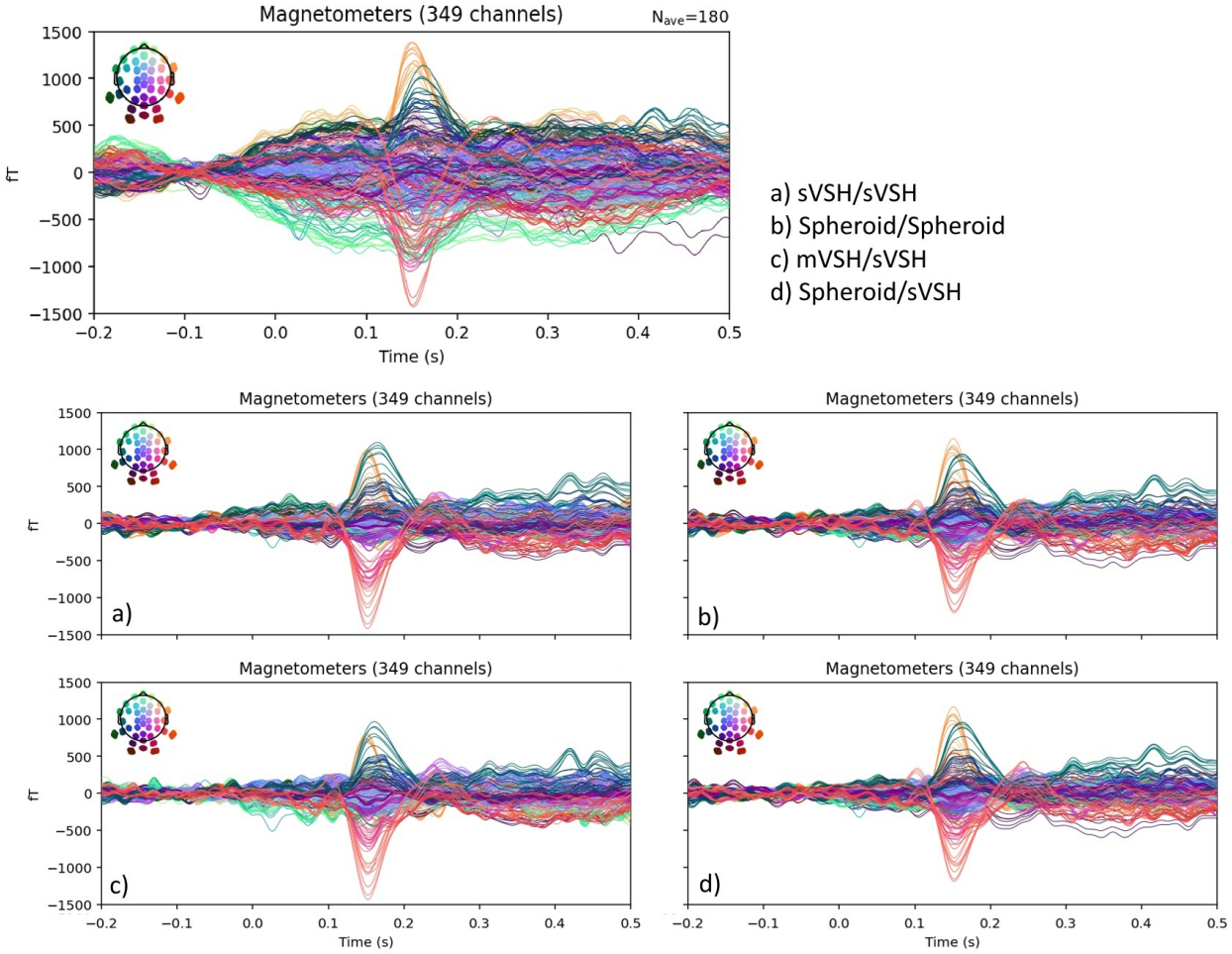

Figure 3.10: Reconstructions of Kernel OPM Audio Evoked data processed using each of the four different SSS geometric variants. The unprocessed evoked data is compared to Subplot a) mVSH/sVSH processed evoked signal, b) sVSH/sVSH processed evoked signal, c) Spheroid/sVSH processed evoked data, d) Spheroid/Spheroid processed evoked data.

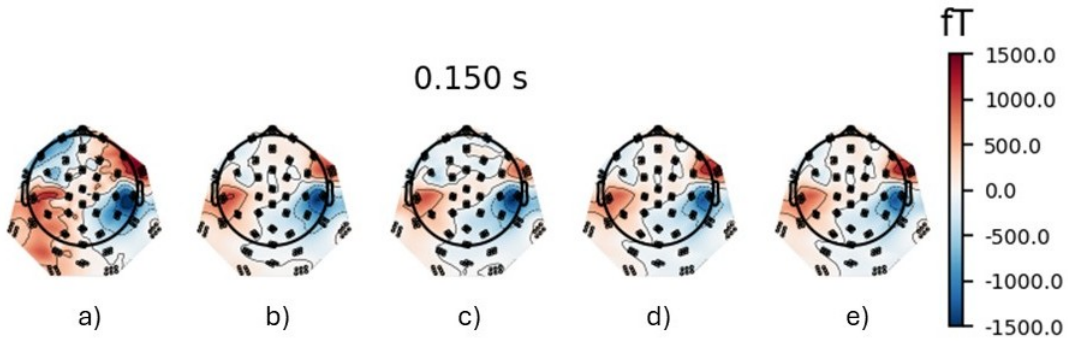

Figure 3.11: Topographic visualizations of the peak time at 0.15s of the Kernel OPM Audio Evoked data processed using each of the four different SSS variants. Panel a) shows the unprocessed evoked data, b) shows the SSS-processed evoked auditory response, c) is the mSSS processed signal, d) is the spheroidal harmonic processed, e) is the augmented spheroidal interior with sVSH exterior. Note that only radial-sensing channels are shown in this figure

Each SSS variant does not visually exhibit a biasing of the evoked signal during data reconstruction (see Figure 3.10). Each SSS variant improves the signal to noise ratio by a similar factor, where the novel augmented spheroidal interior and VSH exterior basis has the highest SNR as seen in Table 3.15. The reduction in noise is also seen in the topographic visualizations of the peak brain response at 0.15 seconds in Figure 3.11, where all SSS variants show good localization of the expected audio stimulus response, cleaned from drifts, and without bias.

3.4.3 University College London (UCL) OPM Audiovisual Example Data Set

The UCL OPM previously acquired and publicly available audiovisual dataset is used as an example for interference suppression techniques on low-channel-count OPM systems [47]. Using a 4-layer MSR, single-subject audiovisual OPM data was acquired at UCL using 43 Dual-Axis QuSpin QZFM Gen-2 OPM sensors placed evenly around the head. The sensors measure both tangential and radial components of the magnetic field, resulting in 86 channels of data. No preprocessing steps were done to the raw data before reconstruction with each SSS variant [31], [47].

The stability of SSS relies on the oversampling of the spatial field when the channel count is much higher than the number of spatial components kept in the VSH expansions. With the typical and optimal orders kept, the SSS basis comprises 95 vectors (80 interior and 15 exterior), but here the channel count is less than the spatial components [51]. One way to reduce the spatial dimensions of the SSS basis is to reduce the number of interior L_{in} components kept from the optimal 8 down to 6, reducing the dimensionality of the interior basis from 80 to 48 spatial components. Of course, such a low order could lead to some brain signal bias due to the relatively low spatial frequency cut-off. Further noise reduction could be achieved with other computational methods, such as with iterative SSS as mentioned previously [21]. Here, we implement each SSS variant with $L_{in} = 6$ internal components kept in both spherical and spheroidal harmonic expansions to process the UCL OPM dataset. First, the condition number for each SSS variant was calculated and is listed in Table 3.16.

Table 3.16: Condition number of each SSS variant for the 86-Channel UCL QuSpin OPM system with different interior harmonic orders kept

SSS Variant	$L_{in} = 6$
sVSH interior	125
mVSH interior	1.00
Spheroidal interior	41.0
sVSH/sVSH	326
mVSH/sVSH	113
Spheroid/Spheroid	131
Spheroid/sVSH	112

Next, the minimum, mean, and maximum subspace angle between the raw data matrix for all channels at all times and each SSS variant was calculated and the results are shown in Table 3.17. The raw data and each set of SSS variant processed data was converted

to an evoked response for visual comparison. The evoked responses were calculated using MNE-Python after a 50 Hz and 251 Hz notch filter was applied to remove interference from power lines. Results were processed using both the bandpass filter from the tutorial at 2 to 40 Hz and one modified to be between 0 and 40 Hz. OPM sensors are more sensitive to DC and low frequency fields, so the impact of these fields is typically captured in the 0 to 2Hz range. No other processing was performed on the raw and SSS-reconstructed data to create the evoked response [31] [47].

Table 3.17: Minimum, Mean, and Maximum Subspace angle (in degrees) between the UCL QuSpin OPM Raw data and SSS basis for each variant.

SSS Basis variant	$L_{in} = 6$
sVSH/sVSH	2.47/3.13/4.50
mVSH/sVSH	1.20/1.73/2.59
Spheroid/Spheroid	2.54/12.3/23.2
Spheroid/sVSH	2.32/3.03/4.37

Keeping the threshold value consistent for the calculation of the mSSS basis, the mSSS basis is 86×80 for $L_{in} = 6$. The mSSS basis is more square than the SSS basis and is overdetermined, but only by 6 vectors as opposed to 23 vectors as with the SSS basis at the same L_{in} value. This suggests that the threshold value may need to be updated depending on the channel count of the OPM system. Raising the threshold value restricts the number of spatial vectors kept in the mSSS basis based on the ratio of significant values obtained from SVD. We investigated the impacts of raising the threshold from 0.005 to 0.05 to adapt to the lower channel count.

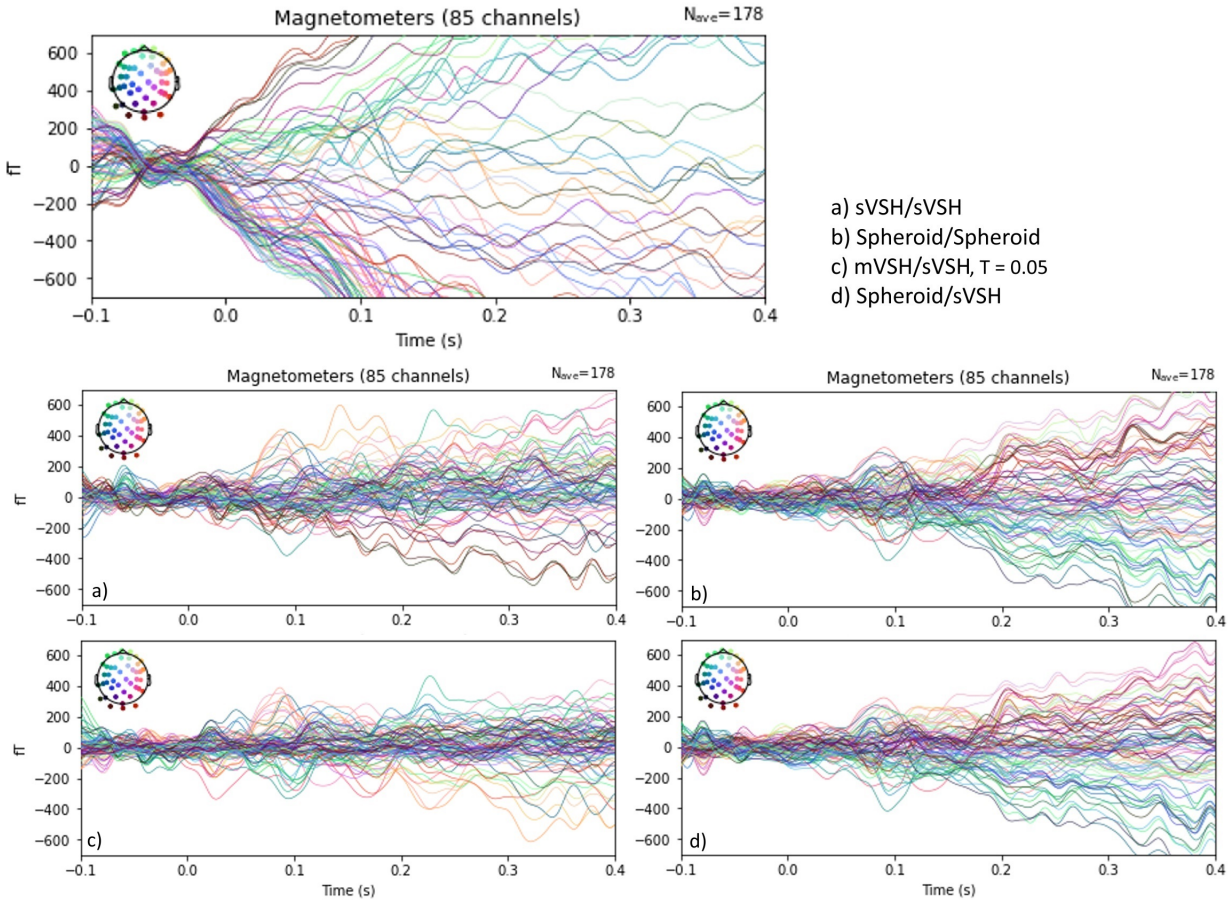

Figure 3.12: Reconstructions of the UCL QuSpin OPM auditory evoked data after processing with each SSS variant for $L_{in} = 6$ and a bandpass filter from 0 to 40 Hz. The top left subplot shows the unprocessed by SSS evoked response. Subplot a) shows the sVSH/sVSH processed evoked response, b) shows the vector spheroidal harmonic interior and exterior processed evoked response, c) shows the mVSH/sVSH processed evoked response with the threshold set to 0.05 (updated from the value of 0.005 used previously), and subplot d) shows the augmented interior spheroidal harmonic basis with the sVSH exterior basis.

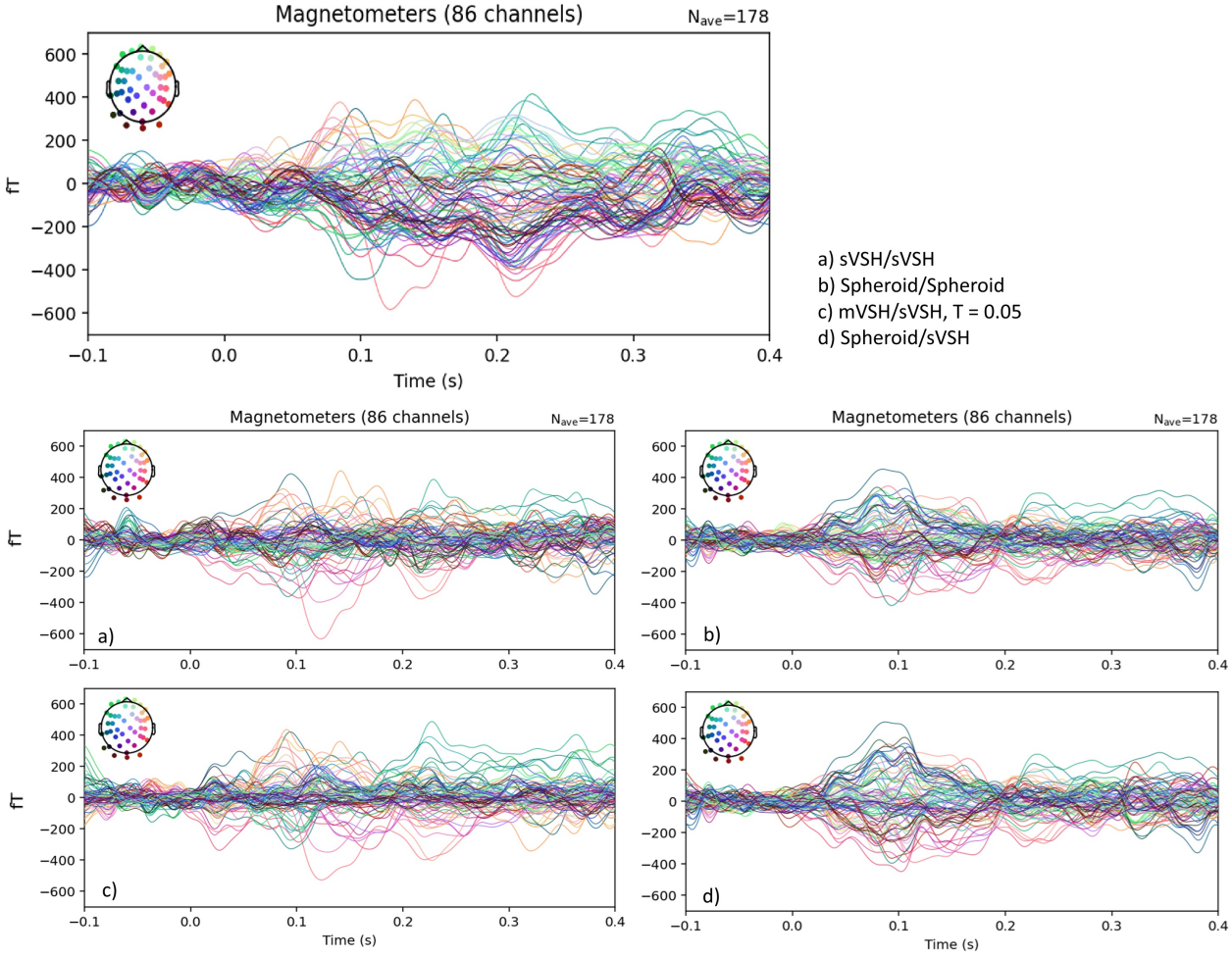

Figure 3.13: Reconstructions of the UCL QuSpin OPM auditory evoked data after processing with each SSS variant for $L_{in} = 6$ and a bandpass filter from 2 to 40Hz. The top left subplot shows the unprocessed by SSS evoked response. Subplot a) shows the sVSH/sVSH (SSS) processed evoked response, b) shows the vector spheroidal harmonic interior and exterior processed evoked response, c) shows the mVSH/sVSH (mSSS) processed evoked response with the threshold set to 0.05 (updated from the value of 0.005 used previously), and subplot d) shows the augmented interior spheroidal harmonic basis with the sVSH exterior basis.

The noise levels in the SSS reconstructions are much lower than in the raw data as seen in Figure 3.12, and is the most effectively reconstructed by the mSSS basis. Note that the threshold value for the mSSS basis construction is 0.05 instead of 0.005 for visualization

purposes. The effect of changing the threshold on the metric comparison values for the mSSS basis is investigated in Table 3.18 and Figure 3.14 below.

Table 3.18: Minimum, Mean, and Maximum Subspace angle (in degrees) between the UCL QuSpin OPM Raw data and SSS basis for each variant.

SSS Basis variant	Thresh=0.05	Thresh=0.005
Dimensions	86×66	86×80
Condition Number	49.5	113
Mean Subspace Angle	4.77	2.60

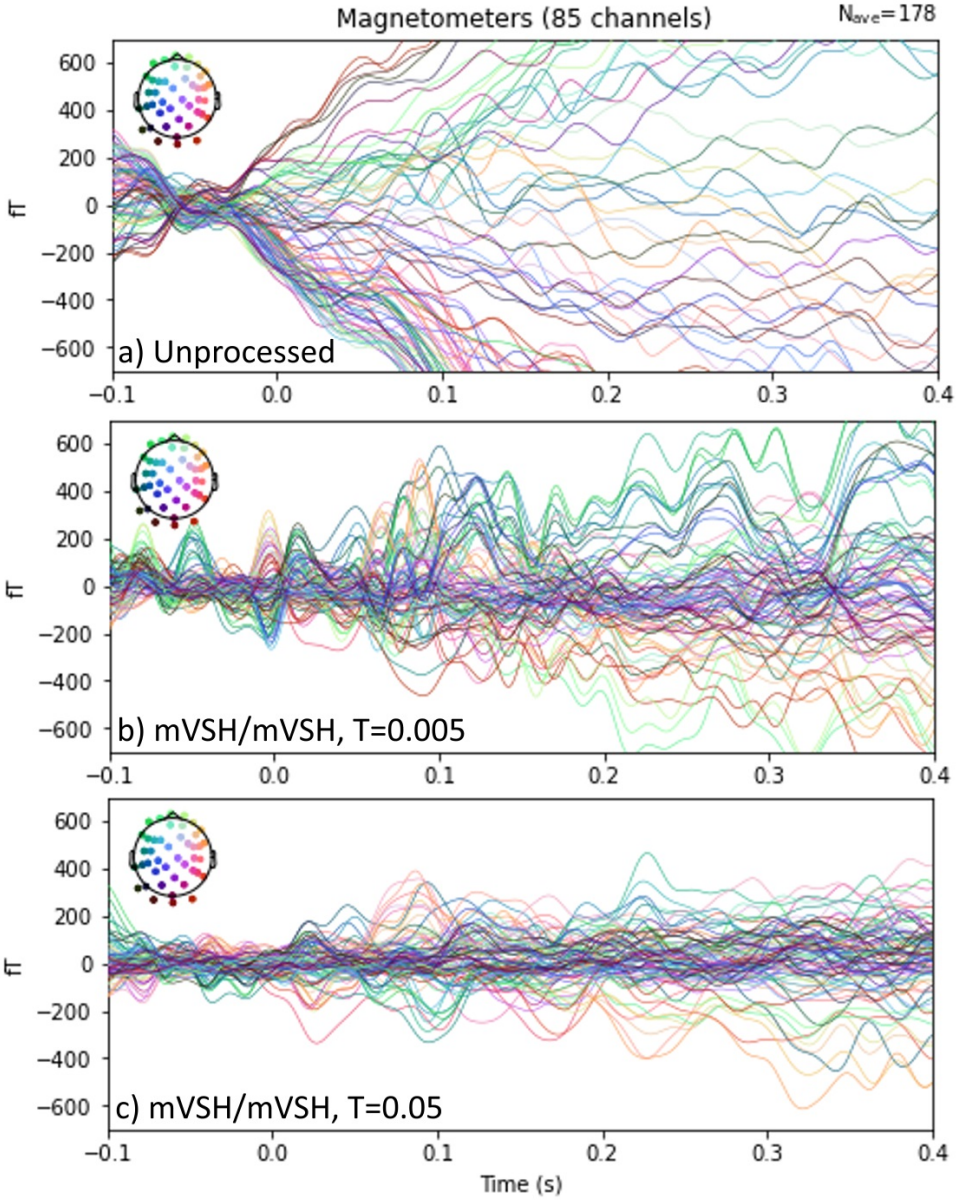

Figure 3.14: mSSS Reconstructions of the UCL QuSpin OPM auditory evoked response after processing with $L_{in} = 6$ and bandpass filter of 0 to 40Hz for two different threshold values curing construction of mSSS. Panel a) shows the SSS-processed evoked auditory response, b) is the mSSS processed signal with a significant value threshold of 0.005 (or 0.5% of the max significant value), and c) is the mSSS processed signal using a threshold of 0.05 (or 5%).

Raising the threshold, and thus reducing the dimensions of the mSSS basis, improves the noise levels of the reconstructed mSSS data as evidenced in 3.14. Finally, we plot topographic maps of the evoked data for each SSS variant at the calculated peak time of 0.09 seconds using MNE-Python [31].

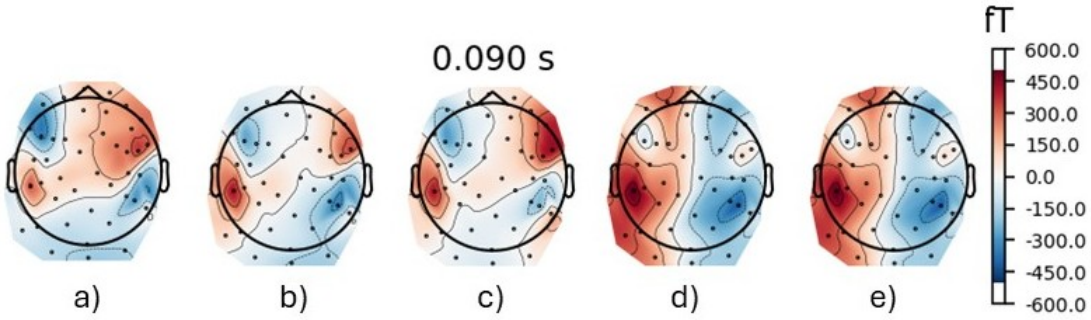

Figure 3.15: Topographic visualizations of the peak time at 0.09s on the UCL QuSpin OPM auditory evoked response after processing with each SSS variant with $L_{in} = 6$ and bandpass filter of 2 to 40Hz. Panel a) shows the unprocessed evoked data, b) shows the SSS-processed evoked auditory response, c) is the mSSS processed signal with a significant value threshold of 0.05 (or 5% of the max significant value), d) is the spheroidal harmonic processed, e) is the augmented spheroidal interior with sVSH exterior.

Regardless of threshold, the mSSS basis gives the best or second best match to the raw signal when considering the subspace angle between the raw and processed data, as seen in Tables 3.17 and 3.18, and the best reduction in noise and drift in the visualization of the evoked data as seen in Figure 3.12, showing the method can help reconstruct internal brain signals even in the presence of low frequency and DC fields. Additionally, augmenting the spheroidal harmonic interior basis with the sVSH exterior basis results in a more stable reconstruction with less drift than the spheroidal exterior basis. mSSS is able to uncover the expected spatial patterns of MEG from an auditory stimulus as seen in Figure 3.15 with strong visual localization and magnitude of the peak brain response.

3.5 Conclusions and Comments

The mSSS method provides adaptability and improved results with the addition of on-scalp MEG sensor systems. The procedure for creating the mSSS basis follows traditional SSS, but used multiple optimized origins to span the brain space with overlapping bases. To improve stability, the bases are combined following similar techniques to eSSS. When mSSS is optimized for two VSH bases, the condition number of the resulting matrix is lower than the other SSS variants due to the orthonormality of the combination, indicating a more stable inverse when mSSS is used to reconstruct MEG data. This conclusion is also supported by the higher Frobenius norm of the mSSS basis, showing that the basis contains more unique information about the interior brain space.

We have also shown that the mSSS method performs as well as SSS, and better, when separating out interior and exterior simulated dipole signals. The adaptability of mSSS is showcased when the sensor helmet geometry has some deviations from the more uniform MEGIN/Elekta Neuromag SQUID helmet setup. In these cases, optimizing multiple spheres allows for a more dynamic span of the brain space than with SSS, resulting in a twofold improvement in data reconstruction. The improvement seen in simulation is reflected in the verification with OPM subject data, where mSSS offers a better data reconstruction with less noise than other SSS basis variants. Across simulations and data, the mSSS basis outperforms with visual, audiovisual, and simulated motor response recordings. The performance of the mSSS basis can be further improved if a priori knowledge about the location of the expected brain signal is known so the origin of the second VSH expansion can be placed in an optimal location to encompass these signals. In practice, the precise location of the brain signal is often unknown, in which case the mSSS basis can be optimized using a subject MRI (general or specific) and MNE-Python to select the location for the expansion origins. Finally, the mSSS basis remains stable when used to process audiovisual data collected on a low-channel count on-scalp systems, which can be further improved by adjusting the threshold for including spatial components in the combined interior basis to adapt.

When applied to evoked data, raw data, and noisy MSR data, the spheroidal harmonics perform comparatively to the other SSS variants when the sensor systems are radially-sensing magnetometers, indicating that their ability to span the interior brain space and exclude exterior noise sources is similar to other variants. To further the applications of the spheroidal harmonic basis, extending the implementation to include gradiometers as well as other sensing directions will allow it's use with SQUID and on-scalp MEG systems more broadly. Additionally, modifying the prolate spheroidal harmonic basis with the single-origin VSH basis for the exterior offers better results than geometrically constraining the exterior basis to spheroidal geometry. This methodology is mathematically concise and represents a valid modification to traditional SSS. Finally, all of these variants can be combined with the tSSS and eSSS extensions for improved suppression of artifacts that cannot be satisfactorily modeled by the external VSH basis.

Chapter 4

OPTIMIZATION OF BASIC MAGNETIC FIELD COMPONENT EXTRACTION

In order to leverage the potentially improved spatial resolution provided by the on-scalp MEG sensors, the basic component extraction of the measured magnetic field need to be optimized to account for increased noise in higher components, allowing for the measurement of more spatially precise magnetic fields. As discussed in Chapter 2, the discrete expansion of the magnetic field measured by MEG sensors is truncated at orders of L (Equation 2.22) for the interior and exterior basis based on factors such as the number of sensors and the distance from the sensors to the scalp, two parameters that have changed in the transition from cryogenic-MEG systems to on-scalp systems [53]. An illustration of the different vector spherical harmonic topographies is included in Figure 4.2.

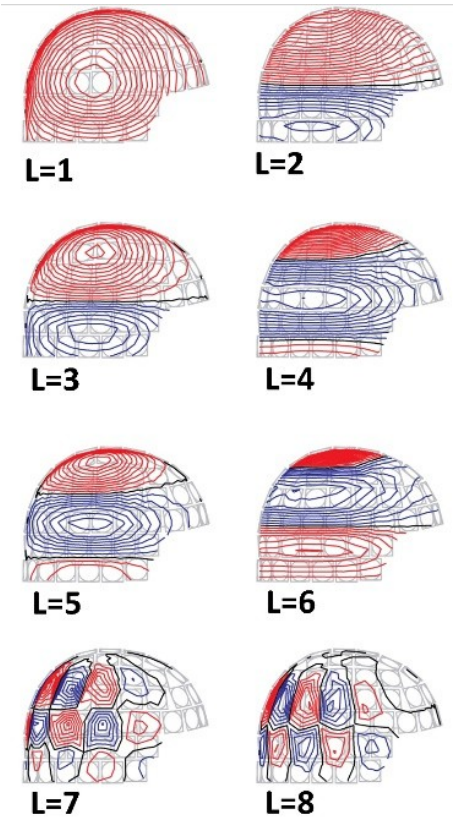

Figure 4.1: Low to high spatial frequency topographies of the interior VSH expansion of the discrete magnetic field $\boldsymbol{B}$ as seen in Chapter 2, Equation 2.22. Increase in L corresponds to an increase in spatial complexity.

The MEG signal measurement $\boldsymbol{\phi}$ appears to be spatially smooth at the sensor location because the higher spatial frequencies decay faster as a function of distance, leaving the terms of lower spatial frequency as the leading measured signals. Additionally, multiple dipole source configurations can result in the same lower order topography, so new and improved understanding of higher spatial frequencies is vital to accurately reconstructing brain signals. The potential to include order of L_{in} greater than the typical 8 can help distinguish between sources with similar lower order components, a result that is well studied across other fields using VSH discretizations such as astronomy [10]. Therefore, improving the basic component extraction accounting for higher noise with higher spatial frequencies is important for being

able to obtain more precise measurements with on-scalp MEG sensors.

Some existing methods, such as the iterative SSS method as discussed in Chapter 2, improve the SSS reconstruction by exploiting the hierarchical nature of the VSH expansion. As the reconstruction of brain signals using these methods requires the inverse of the spatial matrix S, the task of reducing noise in the higher components becomes a linear algebra problem of matrix inversion to find solutions to a simultaneous linear equation. Other than noise from external factors typically attenuated by the MSR and artifacts from nearby sources, the sensor systems themselves are a source of random noise intrinsic to the devices. The contribution of sensor noise is taken into account during data processing in the form of a covariance matrix, which makes obtaining correct measurements or estimates of the covariance extremely important [54]. Specifically in SSS, the inverse of the S matrix must be used to estimate the multipole moments to reconstructed the data, a step that can become unstable in the presence of noise. Thus, we must explore new methods for account for sensor noise in the SSS method in order to extract higher-order components of the magnetic field that allow for higher precision source localization.

In this chapter, we explore an application of the Wiener-Kolmogorov smoothing theory to matrix inversion, called Foster's inverse after the author Manus Foster [11], and the method's ability to reduce noise when applied to the reconstruction of MEG data. We first establish the meaning of noise covariance, and discuss current proposed methods for measuring, estimating, and calculating noise covariance profiles. Next, we implement Foster's inverse with SSS on both simulated and single-subject MEG data, while also investigating the effects of different methods of estimating sensor noise covariance matrices on the Foster's inverse method. The noise covariance matrix $\mathbf{N}$ is an important variable in the implementation of Foster's Inverse for SSS, as well as in minimum-norm estimate (MNE) methods for dipole localizations in MEG, so understanding the impacts of different noise profiles is paramount. Additionally, sensor noise reduction methods for processing OPM-MEG data remain relatively unstudied, so we present our investigations into Foster's inverse in SSS as a tool for dealing with noisy OPM data.

4.1 Sensor Noise Covariance Profile Estimation

By definition, covariance is the measurement of how two random variables change together. In the context of MEG measurements, sensor noise levels and the spatial covariance of noise between sensors are part of data measured. There are a variety of ways to quantify or estimate the level of noise in the sensor array, which impacts the noise covariance profile used in data processing steps such as beamformers and MNE dipole localizations [31]. The goal is to obtain a measurement of the noise covariance without including any magnetic signals, such as fields from external sources to the brain signals like eye blinks, movement artifacts, or other remnant fields. These fields are classified as part of the signal in the SSS method, but will be a part of the exterior basis expansion that is mathematically removed from the data during reconstruction as detailed in Chapter 2. The noise covariance profile for the sensors includes any noise that is unique to each sensor itself, perhaps due to differences with manufacturing, as well as any interactions between sensors from spatially correlated noise which may be from fluctuations in sensors themselves or some magnetic impurity near the sensors that effects multiple sensors at once.

The simplest noise covariance profile is a diagonal matrix which represents a case where there is no spatially correlated noise between the sensors, where purely sensor related noise can be modeled as a diagonal matrix if the noise is assumed to be independent across sensors [9]. In practice, however, off-diagonal elements occur, which has been widely characterized for SQUID sensors and occurs in OPM sensors due to quantum, optical, and magnetic effects [58]. Additionally, spatially correlated noise increases with higher sensor count as sensors are closer together, which impacts the noise in OPM systems more than SQUID systems due to the potential for higher channel count designs [37]. Noise covariance profiles that are not assumed to be purely diagonal (not containing spatially correlated noise) must therefore be estimated in some fashion. Practically, some methods for measuring sensor noise involve taking an empty-room recording in the MSR pre-clinical testing, then calculate the covariance of this noise recording [31]. A similar result can be obtained by using resting-state time

segments of a data collection, or from pre-stimulus baselines, which should include minimal brain activity. Other methods, which we will delve into in the next section, calculate the sensor noise of MEG measurements without needing empty-room recordings, which can be then used to develop a noise covariance profile.

4.1.1 MNE-Python Compute Covariance Functions

MNE-Python is a powerful tool for analyzing MEG, EEG, and MRI data, and contains various built in functions for estimating the noise covariance from raw and epoched MEG data. These different methods are mostly characterized by Engemann and Gramfort, and can be called in MNE-Python with the corresponding key to each method: empirical, regularized, Ledoit-Wolf estimator, shrunk covariance, probabilistic PCA, and factor analysis [31], [9]. All of these techniques assume that the amplitudes of the sources and measured data are Gaussian due to linear mixing, therefore the additive noise is also assumed to be Gaussian such that the total MEG measured signal can be characterized with the combination of a mean vector and the corresponding covariance matrix [9].

The empirical covariance matrix $\mathbf{N}$ of data matrix $\mathbf{Y}$, dimensions $N \times M$ can be calculated as $\mathbf{N}_E = \frac{1}{M}\mathbf{Y}\mathbf{Y}^T$ [9]. If the number of data points M is very large, the empirical covariance model becomes a better estimator of the true covariance. However, in the absence of empty room recordings, the number of baseline periods for noise estimation during data collection may be too small to obtain a good estimation. This method is implemented in MNE-Python's compute covariance functionalities [31], and is one of the methods we test here in our Foster's inverse investigation.

4.1.2 Sensor Noise Suppression Methods

Noise from the sensors can be removed from data using a process called the Sensor Noise Suppression (SNS) method, where we assume that sensor noise is uncorrelated with brain activity, and that brain activity measured by one sensor can be reconstructed from any of its neighbors [7]. The first assumption allows us to write the measured sensor signal $\boldsymbol{\phi}$ as

$$\boldsymbol{\phi}(t) = \mathbf{B}(t) + \mathbf{n}(t) \tag{4.1}$$

where $\mathbf{B}$ is the brain activity over time and $\mathbf{n}$ represents the noise from the sensors. Following the second assumption, the denoising algorithm replaces each noisy channel by the regression of the subspace of the other channels. The set of signals $[\boldsymbol{\phi}_{k' \neq k}]$ for each channel k is orthogonalized using PCA to find an orthogonal basis spanned by the other k' channels. Then, the channel $\boldsymbol{\phi}_k$ is replaced by its projection onto this orthogonal basis [7]. Mathematically, the SNS process sums these steps over all channels

$$\tilde{\boldsymbol{\phi}}_k(t) = \sum_{k'=1, k' \neq k}^{K} \alpha_{kk'} \boldsymbol{\phi}_{k'}(t) \tag{4.2}$$

where $\tilde{\boldsymbol{\phi}}_k(t)$ is the denoised sensor signal, the set of all $[\alpha_{kk'}] = \mathbf{A}$ minimizes $||\phi_k(t) - \tilde{\phi}_k(t)||$. In matrix from, $\mathbf{A}$ will have zeros along the diagonal. The SNS method can be used to calculate the sensor noise $\mathbf{n}$, where $\mathbf{n} = \phi_k(t) - \tilde{\phi}_k(t)$. However, this method assumes some knowledge of the spatial and temporal structures of the noise.

4.1.3 Oversampled Temporal Projection

Alternative methods for reducing the effects of sensor noise, such as the Oversampled Temporal Projection (OTP), only require that the signals of interested are spatially over sampled by the number of sensor channels and that the signals of interest are statistically independent from the noise [32]. In this method, we define a matrix $\mathbf{D}$, which is composed of N sensor channels with data over n_s temporal samples. The data matrix can be expanded as:

$$\mathbf{D} = \mathbf{M}_a \mathbf{X}_a + \mathbf{M}_b \mathbf{X}_b + \mathbf{E}_u + \mathbf{E}_c \tag{4.3}$$

where $\mathbf{M}_a$ defines the subspace for signals of interest and $\mathbf{M}_b$ defines the subspace for external interference signals, and $\mathbf{X}_{a,b}$ define the respective coordinates. Matrix $\mathbf{E}_u$ contains uncorrelated artifacts and individual sensor noise, whereas $\mathbf{E}_c$ contains correlated artifacts

that are set to zero and not included in the OTP model [32]. We can then combine this equation into a compact matrix equation

$$\mathbf{D} = \mathbf{MX} + \mathbf{E}_u \tag{4.4}$$

Where matrices $\mathbf{M}$ and $\mathbf{X}$ contain both the a and b subspaces concatenated. The contribution of $\mathbf{E}_u$ can be suppressed using a spatial cross-validation (CV) operator $\mathbf{K}$ such that the denoised data is $\tilde{\mathbf{D}} = \mathbf{KD}$. The properties of $\mathbf{K}$ can be tuned, but for spatially oversampled data, $\mathbf{K}$ is an $N \times N$ matrix with zeros along the diagonal that minimizes spatial bias and spatial spreading of artifacts while maximizing sensor noise suppression [32]. In practice, this can be done using the SVD of $\mathbf{MX} = \mathbf{U\Sigma V}^T$ and requiring that the matrix $\mathbf{K} - \mathbf{I}$ belongs to the left null space panned by the column vectors of $\mathbf{U}$ corresponding to zero singular values. OTP is performed through MNE-Python on MEG data using a constant overlap-add approach with a given time window size to minimize edge artifacts [31], [32].

Once OTP is performed, the difference in the raw data and the OTP processed data is the effect of the sensor noise. The covariance of the sensor noise can thus be calculated as

$$\mathbf{N}_{OTP} = \text{covar}(\mathbf{D} - \tilde{\mathbf{D}}) \tag{4.5}$$

,

where the covariance of the residual noise is performed using the empirical covariance method.

4.2 Foster's Inverse for processing MEG data

4.2.1 Presentation of Foster's Inverse

Given some data vector $\mathbf{y}$ can be written $= \mathbf{Ax} + \boldsymbol{\eta}$, where $\boldsymbol{\eta}$ is the noise vector and $\mathbf{x}$ is the solution or "signal" vector being estimated. We can solve for an estimate of the signal vector

$\bar{\mathbf{x}}$ by performing the inverse operation [11].

$$\bar{\mathbf{x}} = \mathbf{B}\mathbf{y} + \mathbf{b} \tag{4.6}$$

Where the task is to determine the matrix $\mathbf{B}$ and signal vector $\mathbf{b}$ such that we get the optimal estimate of the signal vector. The solution depends on what is known about the noise and signal vector. If we assume that the noise and signal vector are independent, then the information needed is the covariance of the matrices $\mathbf{S}$ and $\mathbf{N}$ made up of the signal and noise vector components respectively.

$$\mathbf{S}_{ij} = \langle (\mathbf{x}_i - \langle \mathbf{x}_i \rangle)(\mathbf{x}_j - \langle \mathbf{x}_j \rangle) \rangle \tag{4.7}$$

$$\mathbf{N}_{ij} = \langle (\eta_i - \langle \eta_i \rangle)(\eta_j - \langle \eta_j \rangle) \rangle \tag{4.8}$$

Using these matrices, an optimum inverse $\mathbf{B}$ of matrix $\mathbf{S}$ is given by the Foster's inverse

$$\mathbf{B} = \mathbf{S}\mathbf{A}^*(\mathbf{A}\mathbf{S}\mathbf{A}^* + \mathbf{N})^\dagger \tag{4.9}$$

which uses the Penrose-Moore pseudoinverse. In fact, Foster's inverse generalizes to the Penrose-Moore psuedoinverse in the absence of noise [11]. An optimal estimate of $\mathbf{x}$ solution vector is given by

$$\boldsymbol{b} = \langle \mathbf{x} \rangle - \mathbf{B}\mathbf{A}\langle \mathbf{x} \rangle \tag{4.10}$$

such that $\mathbf{b}$ is constant over the time course of the data collection.

4.2.2 Adaptation of Foster's Inverse with the SSS Method

In the context of MEG and SSS, $\mathbf{y}$ is the measures signal vector $\boldsymbol{\phi}$, matrix A is the VSH basis obtained from SSS, and $\boldsymbol{\eta}$ is the sensor noise. Other sources of magnetic interference are classified as signal, whether these sources pertain to brain activity or not. We want to write the signal vector $\boldsymbol{\phi}$ using the SSS basis, multipole moment coefficients, and noise as described in the Theory section

$$\boldsymbol{\phi} = \mathbf{S}\mathbf{x} + \boldsymbol{\eta} \tag{4.11}$$

Where we want to optimize the inverse equation

$$\hat{\mathbf{x}} = \mathbf{S}^{\dagger}\boldsymbol{\phi} + \mathbf{S}^{\dagger}\boldsymbol{\eta} \tag{4.12}$$

by instead using Foster's inverse:

$$\bar{\mathbf{x}} = \mathbf{B}\boldsymbol{\phi} + \mathbf{b}. \tag{4.13}$$

Matrix $\boldsymbol{B}$ is Foster's Inverse of the SSS matrix denoted as $\boldsymbol{S}$ [11]

$$\mathbf{B} = \mathbf{X}\mathbf{S}^{*}(\mathbf{S}\mathbf{X}\mathbf{S}^{*} + \mathbf{N})^{\dagger} \tag{4.14}$$

and

$$\mathbf{b} = \langle \mathbf{x} \rangle - \mathbf{B}\mathbf{S}\langle \mathbf{x} \rangle \tag{4.15}$$

Then, the improved estimate $\bar{\boldsymbol{x}}$ can be used to reconstruct the interior signal in the same fashion as traditional and iterative SSS.

$$\boldsymbol{\phi}_{in} = \mathbf{S}_{in}\bar{\mathbf{x}}_{in} \tag{4.16}$$

The matrix $\mathbf{X}$ is determined using the covariance of the multipole moments found using SSS as

$$\mathbf{X}_{ij} = \langle (\mathbf{x}_i - \langle \mathbf{x}_i \rangle)(\mathbf{x}_j - \langle \mathbf{x}_j \rangle) \rangle. \tag{4.17}$$

Alternatively, if the location of the current dipole source is exactly known, perhaps in a forward model calculation or otherwise, the multipole moment coefficients α_{lm} can be calculated directly using Equations 2.25, 2.26, and 2.27 as presented in Chapter 2. The α_{lm}

coefficients must be normalized against the corresponding orders of the SSS basis such that

$$\boldsymbol{x}_{lm} \approx \int_{v'} \lambda_{lm}^{\alpha}(\mathbf{r}') \cdot \mathbf{J}^{P}(\mathbf{r}')dv', \tag{4.18}$$

where $\mathbf{J}^{P}$ is the primary current described by the Sarvas current dipole formula.

In the context of MEG, the noise covariance matrix $\mathbf{N}$ requires more investigation and can be estimated, calculated, or measured. It must correspond to sensor noise, so any magnetic signal features in matrix $\mathbf{S}$ should not be included in the noise matrix. $\mathbf{N}$ will be diagonal if the sensor noise is uncorrelated, but can have some off-diagonal color corresponding to spatial correlation in noise, eddy currents, and random noise from close to sensors in the hardware that effect multiple sensors. Here, we test the novel method for isolating the sensor noise covariance profiles using the OTP-processed data to determine the sensor noise, then calculating the covariance, as well as the empirical method implemented in MNE-Python. Once the correct form for matrix $\mathbf{N}$ is determined, we can then compare SSS, iterative SSS, and Foster's inverse methods in terms of achieving the best signal reconstruction.

In principle, the matrix $\mathbf{S}$ can be obtained from any SSS method, including tSSS, eSSS, and mSSS. Here, we focus on the traditional SSS basis, where either the internal basis or full basis can be used with Foster's inverse.

4.2.3 The Case of Minimum Information

The aforementioned presentation of Foster's inverse in SSS requires knowledge about the noise covariance matrix $\mathbf{N}$ in order for the method to function as stated. In practice, knowing the exact profile of the MEG sensor noise can be quite difficult. In the minimum information case, the full profile of the noise is unknown, but the covariance matrix can be written as $\mathbf{N} = \sigma_N^2\mathbf{I}$ where σ_N^2 is the noise power and $\mathbf{I}$ is an identity matrix the same size as $\mathbf{N}$ [11]. Similarly, the covariance of multipole moments can be written as $\mathbf{X} = \sigma_X^2\mathbf{I}$ where σ_X^2 is the signal power. Using these variables, we can rewrite Equation 4.14 as

$$\mathbf{B} = \mathbf{S}^{*}(\mathbf{S}\mathbf{S}^{*} + r^2\mathbf{I})^{\dagger} \tag{4.19}$$

where $r^2 = \sigma_N^2/\sigma_X^2$ is the noise-to-signal power ratio [11]. Specifically in the context of SSS, σ_X^2 corresponds to the signal-to-noise ratio (SNR) of the multipole moments. Note that the minimum-information inverse operator $\mathbf{B}$ has the same structure as the regularized Tikhonov operator $\mathbf{T}$ which gives solutions to noisy linear equations, given by

$$\mathbf{T} = \mathbf{A}^T(\mathbf{A}\mathbf{A}^T + \lambda\mathbf{I})^{-1} \tag{4.20}$$

where λ is some positive regularization parameter [29]. By comparing $\mathbf{B}$ with $\mathbf{T}$, we see that the ratio $r^2 = \sigma_N^2/\sigma_X^2$ functions as a regularization parameter in the minimum-information case of Foster's inverse. In fact, choosing $\lambda = \sigma_N^2/\sigma_X^2$ is the unbiased, linear, and minimum mean square error estimator of $\mathbf{x}$ [29]. Using Foster's inverse in this fashion means that the maximum amplification factor from any one large instance of sensor noise impacts the solutions by a factor of $1/(2r)$ regardless of the amplitudes of the SSS basis expansion [11]. Estimating or calculating the noise-to-signal power ratio may be simpler than finding the full noise covariance profile, especially for on-scalp MEG systems that have not been widely characterized.

In the context of SSS and MEG data, using a diagonal matrix for $\mathbf{N}$ in Equation 4.14 represents the minimum information case as the noise-to-signal ratio must be calculated using the multipole moments as well as the noise. The impact of different magnitudes of noise covariance along the diagonal is investigated here using current dipole simulations in the following sections.

4.2.4 Analogy to the Linear Wiener Estimate in Noise-Normalized MNE Methods

As mentioned here and extensively studied, the inverse problem of mapping collected MEG (and EEG) data into the location and time of brain currents creating the signal has, in principle, infinite solutions. Thus, many have developed methods to constrain the most likely solutions to the inverse problem using what we know about biology, brain structure, and the underlying physics of the signals. One large category of these solutions are MNEs, which on a simple level, solve the noiseless equation $\mathbf{y} = \mathbf{A}\mathbf{x}$ with the MNE estimate for

the solution $\bar{\mathbf{x}} = \mathbf{A}^T(\mathbf{A}\mathbf{A}^T)^{-1}\mathbf{y}$, where $\mathbf{y}$ is the measurement vector, $\mathbf{A}$ is some mixing matrix showing the mapping of the currents onto the sensors, and $\mathbf{x}$ are the unknown current sources [29]. MNE methods can be improved using noise-normalization techniques, such as dynamic statistical parameter mapping (dSPM) [6] and standardized low resolution brain electromagnetic tomography (sLORETA) [39], which weight the MNE solution to combat the fact that MNE methods are biased to locate sources superficially on the cortex that in reality originated from deeper activity [29]. Both methods begin with the same data vector $\mathbf{y} = \mathbf{A}\mathbf{x} + \boldsymbol{\eta}$ as discussed previously in the Foster's Inverse section. Estimates for the brain current sources $\hat{\mathbf{x}}$ are obtained using the Linear Wiener estimate $\mathbf{W}$ [59] where

$$\hat{\mathbf{x}} = \mathbf{W}(\mathbf{A}\mathbf{x} + \boldsymbol{\eta}) = \mathbf{W}\mathbf{A}\mathbf{x} + \mathbf{W}\boldsymbol{\eta} \tag{4.21}$$

The Wierner estimator is written in terms of the spatial covariance of the dipole strengths $\mathbf{R} = \langle \mathbf{x}(t)\mathbf{x}(t) \rangle$ and the covariance of the sensor noise vector $\mathbf{N} = \langle \boldsymbol{\eta}(t)\boldsymbol{\eta}(t) \rangle$ as [6],[29]:

$$\mathbf{W} = \mathbf{R}\mathbf{A}^T(\mathbf{A}\mathbf{R}\mathbf{A}^T + \mathbf{N})^{-1} \tag{4.22}$$

Comparing this equation to Equation 4.14, we can see that this form of $\mathbf{W}$ shares similar mathematical composition with $\mathbf{B}$ from Foster's Inverse, where the covariance of the multipole moments matrix $\mathbf{X}$ is analogous to the spatial covariance of the dipole strength matrix $\mathbf{R}$, and the SSS matrix $\mathbf{S}$ is analogous to the forward matrix operator $\mathbf{A}$ [6], or mixing matrix [29].

The full Foster's inverse solution for the current multipole moments $\bar{\mathbf{x}}$ can written as follows by plugging in $\mathbf{B}$ and $\mathbf{b}$ in Equation 4.13:

$$\mathbf{x} = \mathbf{B}\boldsymbol{\phi} + \langle \mathbf{x} \rangle - \mathbf{B}\mathbf{s}\langle \mathbf{x} \rangle = \mathbf{B}(\mathbf{S}\mathbf{x} + \boldsymbol{\eta}) + \langle \mathbf{x} \rangle - \mathbf{B}\mathbf{S}\langle \mathbf{x} \rangle \tag{4.23}$$

Where the first term $\mathbf{B}(\mathbf{S}\mathbf{x} + \boldsymbol{\eta})$ matches the Wierner estimate for the brain currents $\hat{\boldsymbol{x}}$ in Equation 4.21. The complete Foster's solution in Equation 4.23 contains extra terms

pertaining to the average multipole moments found during SSS, which are further weighted by the SSS matrix itself in the term **b**.

4.3 Verify with Current Dipole Simulation

To test the feasibility and performance of using Foster's Inverse with SSS, a simulation was conducted in Matlab first with a current dipole located at 5cm along the x-axis using the Sarvas formula as discussed in Chapter 2 [45]. The moment of the dipole varies sinusoidally in time. Before the dipole is activated, the simulation includes a baseline period to represent the time when a brain is less active before experiencing the onset of a stimulus, and Gaussian noise is added at a level of 20% of the maximum simulated signal amplitude. Finally, the magnetic flux through each of the sensors was calculated using standard gradiometer and magnetometer dimensions for the 306-channel MEGIN/Elekta Neuromag SQUID sensors given in the MNE-Python documentation [31].

Optimizing the multipole moments $\bar{\boldsymbol{x}}$ is more straightforward in simulations because the initial multipole moments $\boldsymbol{x}$ can be calculated directly using the location and moment of the simulated dipole up to the internal expansion order L_{in}, then the covariance of the multipole moments can be calculated as well. We then calculate the diagonal noise covariance matrix **N** from the generated Gaussian noise.

4.3.1 Single Current Dipole Simulation Results

The Foster's inverse implementation of SSS is compared to the raw simulated signal, the traditional SSS reconstruction, and the iterative SSS reconstruction by first calculating the SNR for each simulated dataset as:

$$SNR = \frac{\mathrm{E}[s^2]}{\mathrm{E}[n^2]} \tag{4.24}$$

where the expected value E is the mean square, or mean of the standard deviation squared, equivalent to the mean of the variances, of the signal s or noise n. The SNR calculation

results using the baseline period before 5ms as the noise period ad the signal period after 5ms are shown in Table 4.1.

Table 4.1: Signal to Noise Ratio (SNR)

SSS Variant	SNR
Simulated Data	6.08e+3
SSS	1.15e+4
Iterative SSS	1.10e+4
Foster's SSS	5.48e+5

Foster's inverse provides over a tenfold increase in SNR compared to the iterative and traditional SSS reconstructions of the simulated data as evidenced in Table 4.1. These results are also seen visually when the simulated current dipole is plotted with the SSS-processed and Foster's-processed data along the same axis.

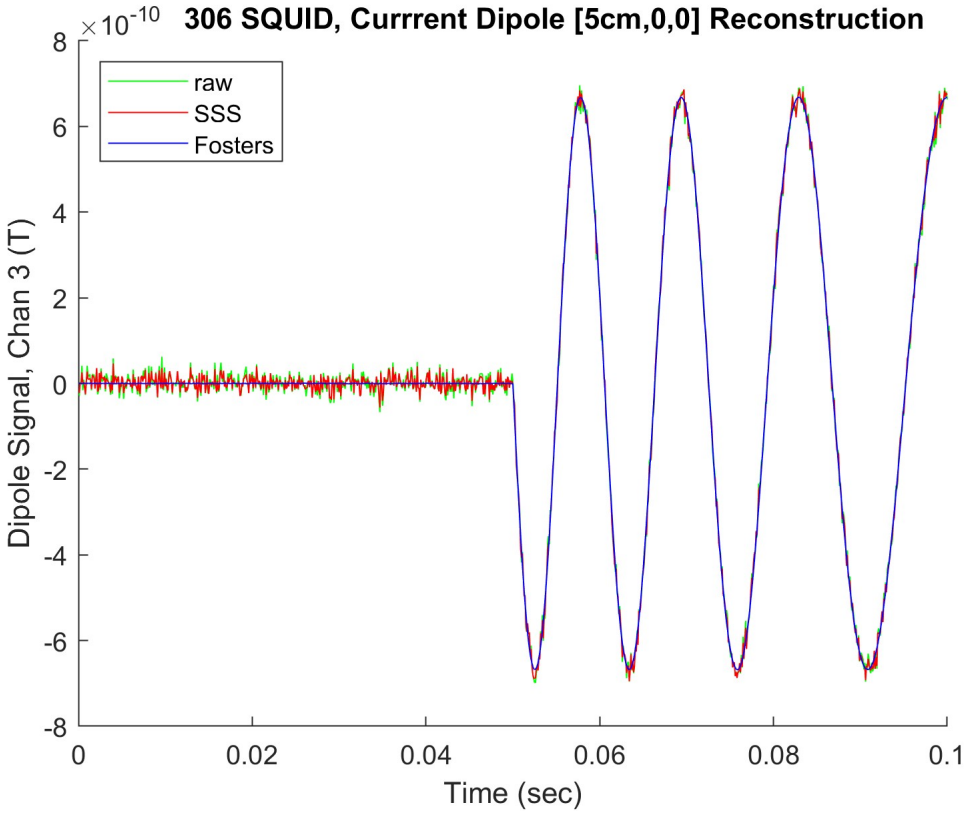

Figure 4.2: Comparison of raw noisy current dipole data and data after Foster's inverse SSS reconstruction generated using the Sarvas current dipole formula with Gaussian noise added at 20% of the maximum signal.

As seen in Figure 4.2, the Foster's inverse reconstruction of the simulated MEG data has vastly reduced the amplitude of noise compared to the unprocessed and SSS processed data. This result can be further seen in the PSD periodogram plots of the three datasets in Figure 4.3

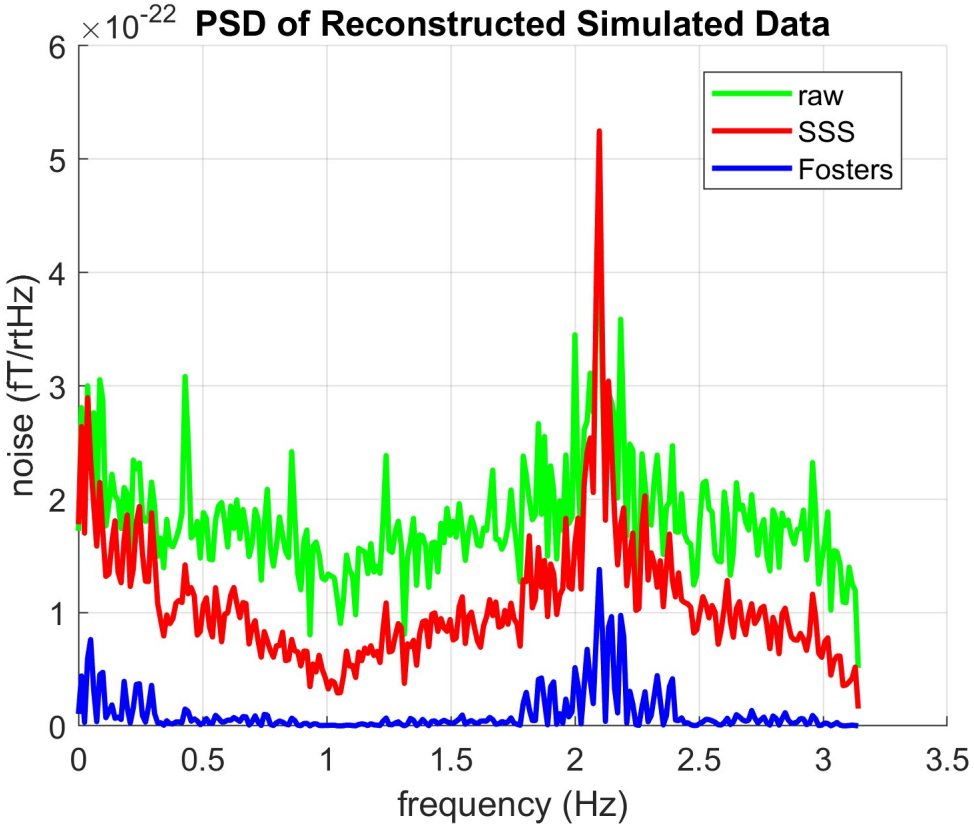

Figure 4.3: PSD plots of the simulated current dipole signal, SSS reconstructed signal, and Foster's Inverse SSS reconstructed signal. Plots are generated and calculated in Matlab

The dramatic decrease in signal reconstruction noise seen in Figures 4.2 and 4.3 is a promising result and shows the potential for the Foster's inverse method to provide noise reduction on higher order terms when applied to both Phantom and human MEG data recordings. As mentioned, when the location of the dipole is known, the multipole moments can be calculated directly as in this simulation. In reality, the location of the current dipole source in the brain is unknown, but can be estimated using the SSS reconstruction as described in Chapter 2.

4.3.2 Simulated Noise Covariance Investigation

To investigate the impacts of noise covariance profiles, we can start with simple, simulated covariance matrices with different properties representing possible physical profiles simulated in conjunction with the single current dipole simulation. The simplest $\mathbf{N}$ matrix is an $m \times m$ square matrix of zeros, $\mathbf{N}_0$, representing a scenario where no information is known about the noise profile. Next, we investigate a diagonal matrix $\mathbf{N}_{\mathrm{D,mean}}$ where each diagonal element has the same value calculated using the mean of an example covariance profile for the MEGIN/Elekta Neuromag system, which is 3.67e-25 [31]. The diagonal matrix is also investigated with varying magnitudes along the diagonal, such as $\mathbf{N}_{\mathrm{D,max}}$ using the maximum value (5.63e-21) of the sample noise covariance profile. As these values are quite small and very near the case of $\mathbf{N}_0$, diagonal values incrementing from 1e-15 to 1e-5 are also investigated. Finally, we construct a diagonal matrix with off-diagonal color $\mathbf{N}_{\mathrm{Dc}}$, which is diagonal but contains other components that represent spatially correlated noise or a more complex noise profile. Each of these covariance matrices are implemented with Foster's inverse applied to simulated current dipole data.

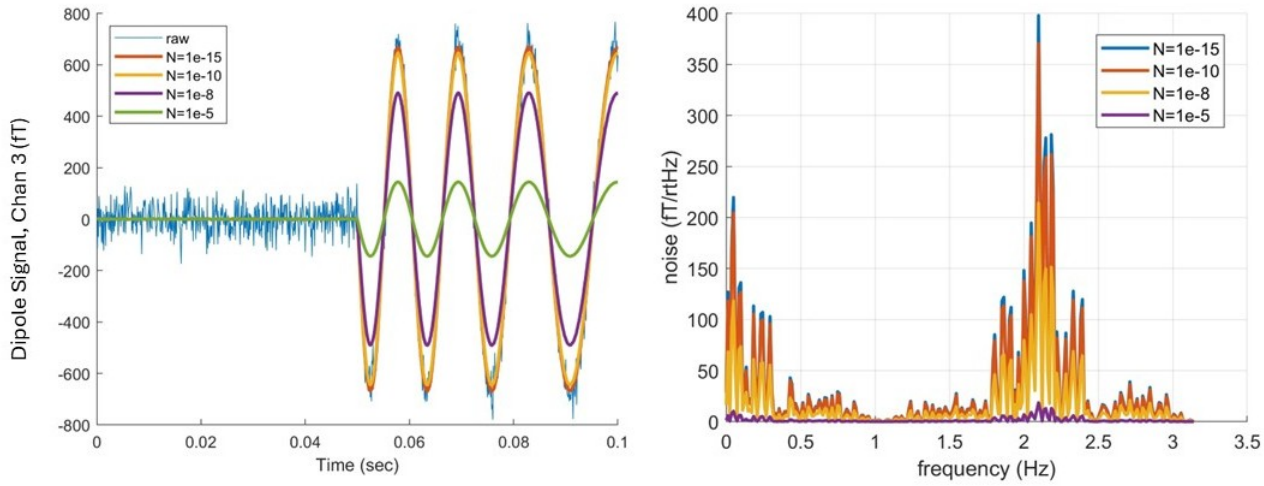

Figure 4.4: Left: Simulated dipole reconstructions for different simulated diagonal **N** matrices with varying amplitudes along the diagonal plotted against the noisy simulated raw signal. Right: Corresponding PSD spectrum of the reconstructed signals for varying simulated diagonal **N** matrices.

Despite the SNR of the reconstructed data staying consistent and the subspace angle between the raw data and the reconstructed data for each **N** remaining computationally zero (below 1e-13 degrees), Figure 4.4 shows different magnitudes along the diagonal **N** matrices dramatically impacts the amplitude of the reconstructed signal. Furthermore, this effect is nonlinear, where larger values of **N** create bigger drops in amplitude, as seen in the difference between **N** =1e-15 to **N** =1e-10 compared to **N** =1e-10 to **N** =1e-5. Increases in **N**, corresponding to a decrease in reconstruction amplitude, also create an artificial reduction in SNR as seen in Figure 4.4 in the sense that the noise may not be reduced in a way that is non-biased towards the signal itself. The results of this investigation highlight the importance of obtaining the correct **N** profile and how differences in noise covariance magnitude may impact the reconstructed results.

4.4 Verify with Phantom and Single-Subject MEG Data

4.4.1 Phantom Head Results

The dry Phantom head manufactured by MEGIN/Elekta Neuromag comes with the SQUID sensor system as a diagnostic tool. The head is made of a plastic hollow sphere with radius 87.5 mm containing 32 artificial current dipoles that can be activated independently in series with four HPI coils for head position tracking. The current dipoles themselves are made using equilateral triangles of current lines to produce a magnetic field distribution equivalent to a current dipole oriented tangentially to the surface of a spherical conductor [29], [8]. Since the orientations and locations of the 32 dipoles are exactly known, the data measured by the SQUID system when each dipole is activated can be treated as an evoked set and used to check the localization of the dipole.

Here, we focus on four different Phantom datasets taken with the 306-channel SQUID sensor MEGIN/Elekta Neuromag MEG system. These datasets were taken at I-LABS over the past few years, with varying dipole field strengths, reflecting the input current or voltage levels, and internal active shielding (IAS) settings. The file names listed in Table 4.2 contain the exact date as year-month-day, followed by the dipole field strength relating to the current passed through the wires, and the IAS system either on or off. The datasets are numbered 1) through 4) in the first column for ease of reference. Datasets 1) and 2) were recorded on the same day with two different dipole field strengths, 1000 nAm and 200 nAm, respectively. Similarly, datasets 3) are 4) from the same day, both using 1000 nAm levels in the current dipoles, with the IAS system off, then on. 1000 nAm corresponds to an unrealistically high signal whereas 200 nAm are used to represent a more realistic strength close to human brain activity.

Each dataset was processed with the internal components of the traditional SSS basis with Foster's Inverse using the empirical method of calculating the noise covariance $\mathbf{N}_E$ implemented in MNE-Python. The Foster's inverse calculation is implemented in Python for

the Phantom analysis. Here, we focus on only the SSS method compared to Foster's inverse. Each of the 32 dipoles is activated multiple times, and the resulting data is averaged into epochs, which are then used to localize the dipole location in MNE-Python [31]. To quantify the success of the dipole localization calculation, the mean and maximum error in position and orientation are calculated, as well as an overall goodness of fit (GOF) percentage where a higher GOF indicates the dipole localization was the most accurate across each of the 32 Phantom dipoles. This data is shown in Table 4.2 and is visualized in Figure 4.5.

Table 4.2: Mean and Maximum Dipole Localization Errors and GOF Metrics for Each Phantom Dataset

Dataset	Method	Position E (mm) mean/max	Orientation E (°) mean/max	GOF (%) mean/max
1) 24-07-08, 1000 nAm	Raw	2.8/12.2	3.3/16	83.0/99.8
	SSS	10.5/58.2	9.4/48	86.7/99.8
	Foster's $\mathbf{N}_E$	2.1/5.8	2.7/9.2	98.7/99.6
2) 24-07-08, 200 nAm	Raw	14/103.4	14.8/81.1	63.4/97.9
	SSS	21.6/98	24.2/84.7	73.0/99.1
	Foster's $\mathbf{N}_E$	7.2/19.9	8.2/24.8	83.6/98.7
3) 23-12-07, 1000 nAm, IAS off	Raw	2.1/4.2	2.4/6.3	98.3/99.9
	SSS	3.5/9.0	3.4/13.6	98.3/99.9
	Foster's $\mathbf{N}_E$	3.8/8.5	3.9/12.8	98.8/99.7
4) 23-12-07, 1000 nAm, IAS on	Raw	2.9/7.9	3.4/13.5	98.4/99.8
	SSS	3.1/7.1	3.3/9.7	99.2/99.9
	Foster's $\mathbf{N}_E$	2.7/6.0	2.9/8.8	99.0/99.7

Table 4.3: Average Mean Dipole Localization Errors and GOF Metrics Across Each Phantom Dataset

Method	Position E (mm)	Orientation E (°)	GOF (%)
Raw	5.45	5.98	85.8
SSS	9.68	10.1	89.3
Foster's $\mathbf{N}_E$	3.98	4.43	95.7

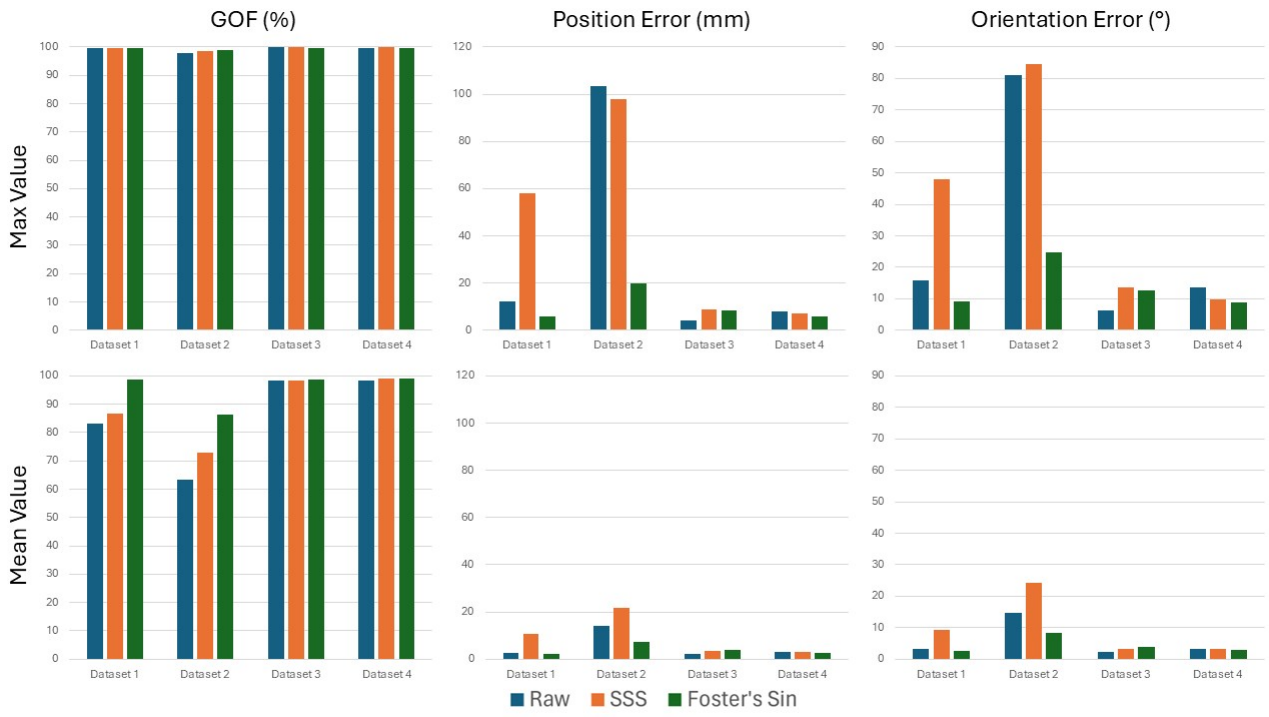

Figure 4.5: Mean and Max dipole localization and GOF metrics for each Phantom dataset, a visualization of the data in Table 4.2

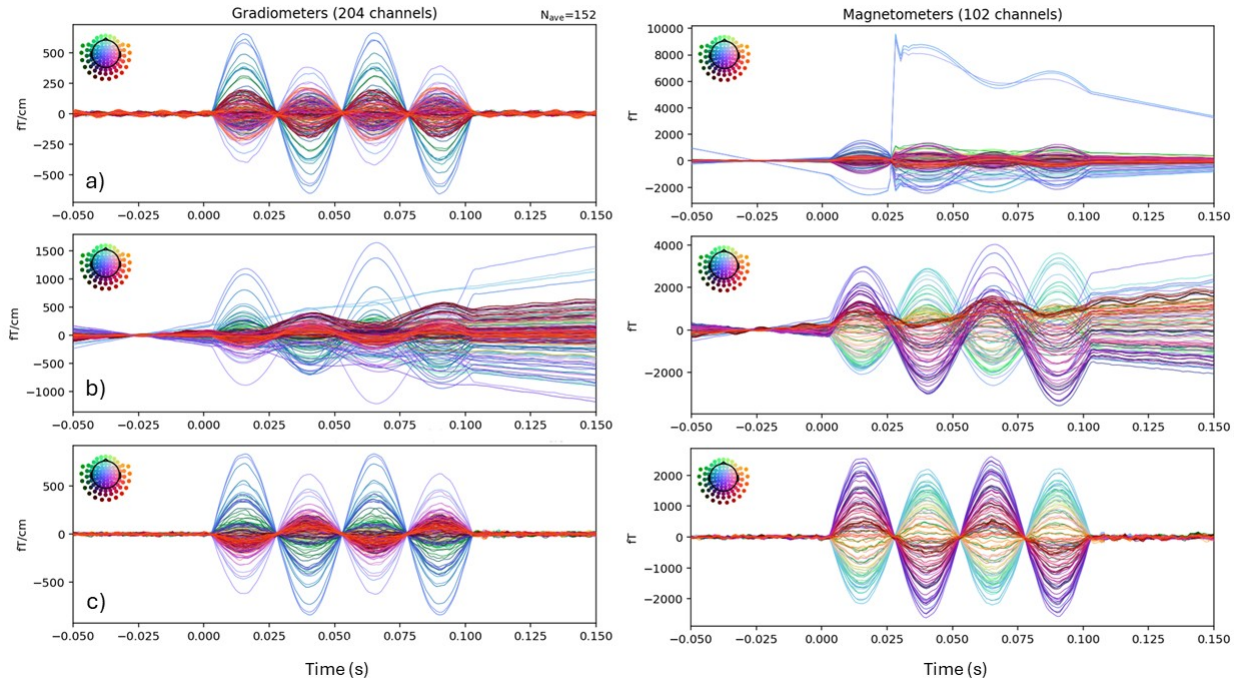

Figure 4.6: Butterfly evoked plots for Phantom dataset 1) generated using MNE-Python where row a) shows the unprocessed evoked data, b) shows the SSS processed data, and c) shows the Foster's processed data.

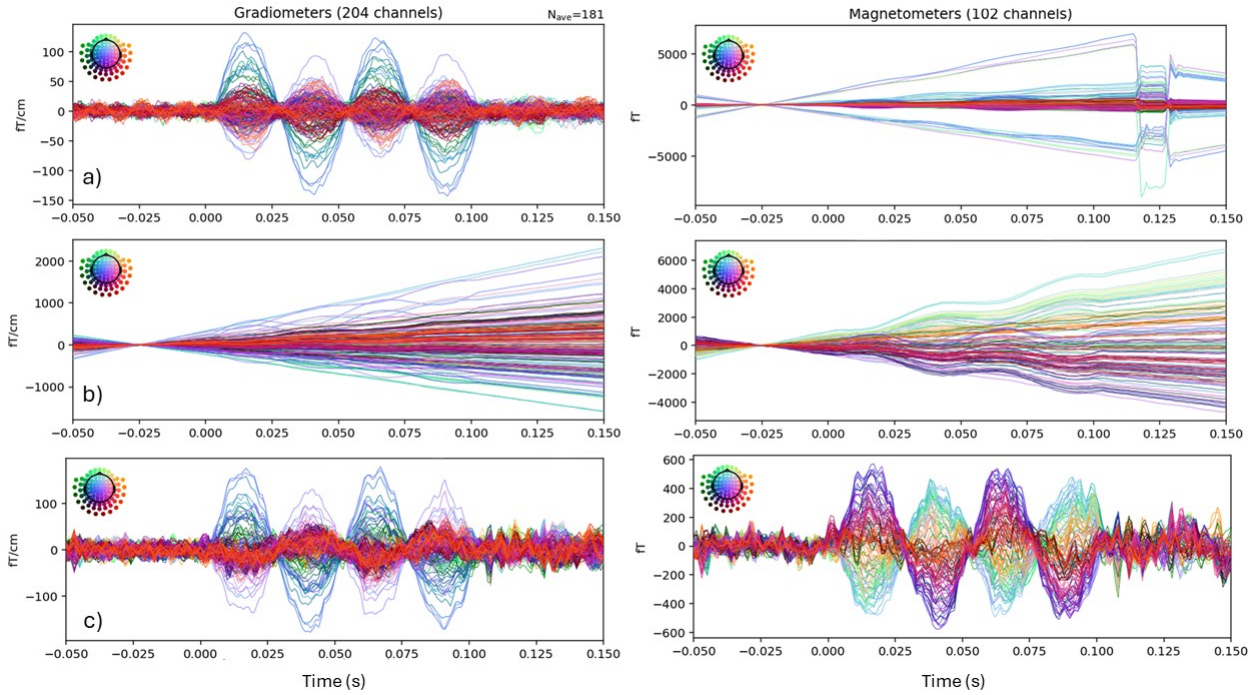

Figure 4.7: Butterfly evoked plots for Phantom dataset 1) generated using MNE-Python where row a) shows the unprocessed evoked data, b) shows the SSS processed data, and c) shows the Foster's processed data.

Evoked plots of Dataset 1) and 2) are visualized to showcase a dataset with some abnormalities in the data, as seen by the artifact specifically in the magnetometer channels in row a) of Figure 4.6 and 4.7. With no other artifact removal procedures, the SSS processed data does improve the GOF from an average of 83% to 86.7% (see Table 4.2), the method suffers from some noise and spreading due to the original artifact. As seen in row c) of Figure 4.6, Foster's inverse with SSS is able to recover the expected dipole plots with a GOF of 98.7%. Similarly, in row c) of Figure 4.7, Foster's inverse is able to recover the expected dipole oscillations despite the large magnetometer artifacts while the SSS reconstruction is not able to recover and the artifact spreads to impacting the gradiometer channel reconstructions as well. Overall, as seen in 4.5, Foster's inverse either matches or improves the GOF of the

dipole localization results, specifically by increasing the mean GOF and especially in datasets with larger noise and artifacts like set 1) and 2). Table 4.3 show that, overall and on average, Foster's inverse with SSS reduced the dipole localization error by 2 mm and improved the goodness of fit percentage by 10%, showing that even in datasets with large artifacts, data processed with Foster's inverse results in precise and accurate dipole localizations.

4.4.2 Kernel Flux OPM Data

As introduced in Chapter 3, the Kernel Flux OPM data, collected at the University of Washington (UW), used 432 OPM channels with coil sensing directions oriented perpendicular to the surface of the subject's head to collect single-subject audio response data in accordance with the UW institutional review board (IRB) human subjects testing guidelines [34]. 349 channels were kept for analysis. Here, we use the same process for creating evoked data approximately 1 s long, averaged over 180 trials of the audio tone response. Sets of evoked data are obtained using epoching and evoked preprocessing functions in MNE-Python [31]. The first has no other preprocessing done, the second is processed using SSS through the Maxwell Filtering function in MNE-Python, the third is processed using the iterative SSS method in Matlab with 10 iterations then transferred to Python, and the fourth is Foster's inverse with the full SSS basis calculated using the MNE-Python implementation [53]. For Foster's inverse, the sensor noise covariance matrix is calculated from an empty-room recording before the single-subject test using the empirical method, $\mathbf{N}_E$, and is compared to the novel covariance calculation using the OTP method $\mathbf{N}_{OTP}$ [47], [31]. Butterfly plots of the evoked waveforms and topographic plots at the peak activity time are visualized for comparison. The SNR is calculated in the same fashion as previously described for the current dipole simulation.

Table 4.4: Signal to Noise Ratio (SNR) of Kernel Flux OPM Evoked Dataset

SSS Variant	SNR
Evoked	11.8
SSS	23.1
Iterative SSS	29.4
Foster's $\mathbf{N}_{OTP}$	21.5
Foster's $\mathbf{N}_{E}$	31.4

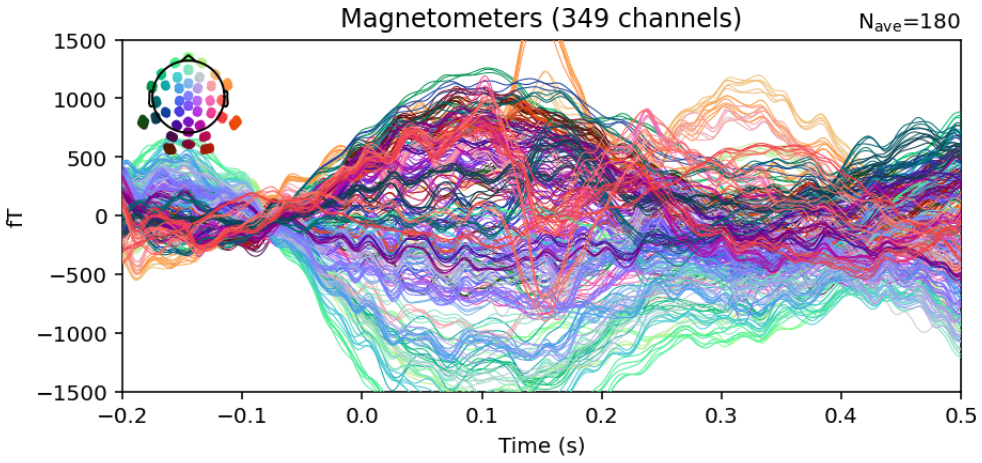

Figure 4.8: Kernel OPM Audio Evoked with no preprocessing.

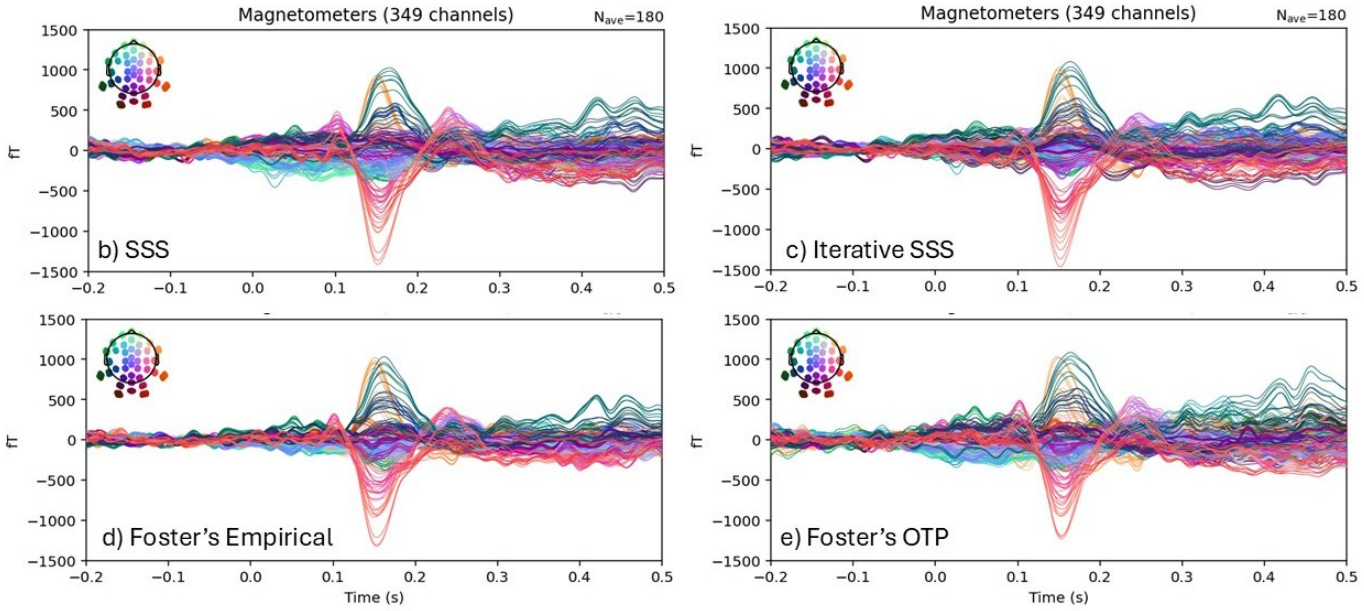

Figure 4.9: Reconstructions of Kernel OPM Audio Evoked where the unprocessed evoked data is compared to Subplot b) showing the SSS processed evoked signal, Subplot c) Foster's inverse using empirical sensor noise covariance $\mathbf{N}_{OTP}$, and Subplot c) Foster's inverse using empirical sensor noise covariance $\mathbf{N}_E$.

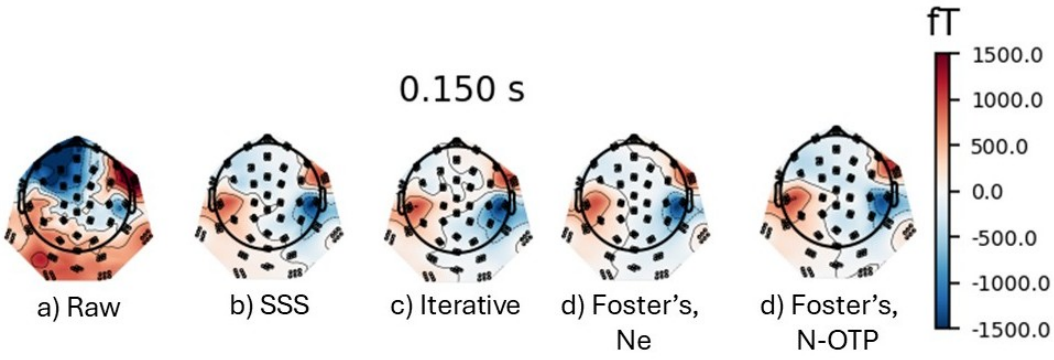

Figure 4.10: Topographic visualizations of the peak time at 0.15 s of the Kernel OPM Audio Evoked data shown in Panel a) compared to Panel b) showing the SSS-processed evoked auditory response, Panel c) Iterative SSS with 10 iterations, Panel d) Foster's inverse using empirical sensor noise covariance $\mathbf{N}_E$, and Panel e) Foster's inverse using the OTP sensor noise covariance $\mathbf{N}_{OTP}$. Note that only radial-sensing channels are shown in this figure

Foster's inverse applied to SSS is able to reduce the noise levels in the data to clearly isolate the peak brain response as seen in Figure 4.9. Furthermore, the locations of peak activity are localized even more precisely when SSS is used with Foster's inverse than SSS alone, as seen in the smaller areas of peak activity in Figure 4.10.

4.4.3 University College London (UCL) OPM Audiovisual Example Data Set Results

As previously discussed and tested with the mSSS method in Chapter 3, the UCL OPM audiovisual data set is utilized here to investigate the results of the Foster's inverse method. For reference here, the dataset was acquired at UCL using 43 Dual-Axis QuSpin QZFM Gen-2 OPM sensors placed evenly around the head inside a 4-layer MSR, totaling 86 measurement channels of radial and tangential components of the field, and is included as an example dataset in MNE-Python [31]. Due to the lower channel count compared to other MEG systems discussed in this dissertation, the internal expansion for the SSS basis is set at $L_{in} = 6$ to insure that the basis is stable. As mentioned in Chapter 3, lower internal orders can lead to a bias towards the brain signal during reconstruction, but further noise reduction could be

achieved with methods like the mSSS method [35].

Here, we test the implementation of Foster's inverse with SSS using two different methods for calculating the sensor noise covariance matrix $\mathbf{N}$: one using the empirical method $\mathbf{N}_E$, which is the default to the MNE-Python's compute raw covariance functionality [9], and one using the OTP method described in Section 4.1.3 of this Chapter, labeled $\mathbf{N}_{OTP}$. First, we calculate the subspace angles between the raw data and the reconstructed data for both the SSS and both variations of Foster's inverse SSS. Then, we visualize the evoked plots and topographic maps of the reconstructed data at the peak time.

Table 4.5: Minimum, Mean, and Maximum Subspace angle (in degrees) between the UCL QuSpin OPM Raw data and Reconstructions

Method	SSS	Iterative	Foster's $\mathbf{N}_E$	Foster's $\mathbf{N}_{OTP}$
Min	0	0	0	0
Mean	1.58	5.17	1.89	0.956
Max	18.6	22.18	22.0	21.8

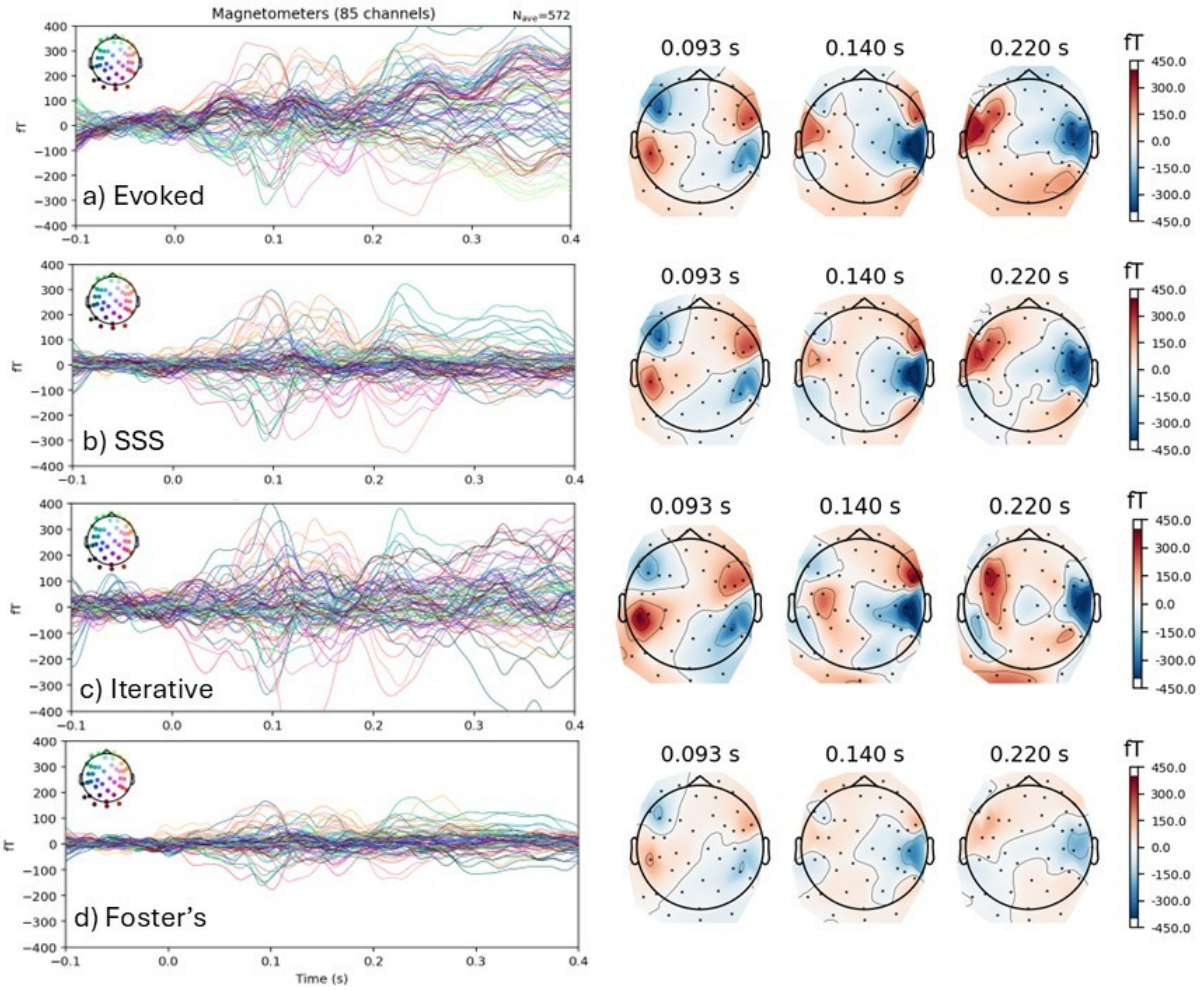

Figure 4.11: Reconstructions of the UCL QuSpin OPM auditory evoked data and corresponding topographic visuals at peak time after processing with each SSS variant for $L_{in} = 6$ and a bandpass filter from 0 to 40 Hz. Row a) shows the unprocessed evoked data, b) shows the SSS reconstructed data, c) shows the iterative SSS reconstructed data, and d) shows the Foster's Inverse reconstruction using $\mathbf{N}_E$

Figure 4.11 shows that both Foster's inverse implementations, regardless of the methodology used to obtain matrix $\mathbf{N}$, can further reduce the noise present in the data more than SSS alone. Foster's inverse with SSS can also recover higher spatial frequencies as seen in 4.11, the locations of the peak activity are more precisely localized in the auditory cortex on both

sides of the brain. There is a slight variation in the topographies between the two methods for finding the noise covariance matrix **N**, but both exhibit tighter peak localization than the unprocessed evoked and SSS reconstruction.

4.5 Comments and Conclusions

In this chapter, we explored the Foster's matrix inverse method applied to SSS for an improved extraction of higher spatial frequencies of the magnetic fields generated by brain activity. Foster's inverse relies on an accurately obtained or measured covariance matrix **N** that captures the sensor noise levels only. We discussed a number of different methods for calculating the sensor noise covariance, including multiple methods already implemented in the MNE-Python package, as well as other novel possibilities including the use of OTP to isolate the sensor noise from the measured data [31], [32]. Foster's also offers an adaptation to the optimized inverse method that can be used when the full noise covariance is unknown, and the noise-to-signal ratio of the data can be used instead in the so-called minimum information case.

Through noisy current dipole simulations, it was found that Foster's inverse with SSS drastically improves the SNR of the reconstructed data by two orders of magnitude as seen in Table 4.1 when the noise covariance matrix is calculated from the Gaussian noise generated in the simulation, and the multipole moments are calculated from the current dipole. In practice, the exact location of the current dipole is unknown, but any a priori information about the location of the source is a powerful asset for Foster's inverse. Additionally, simulated **N** profiles showed that the magnitude of the diagonal elements, representing individual sensor noise levels, appear to have the largest effect on the reconstructed data in the form of noise reduction and bias introduction as seen in Figure 4.4.

Finally, Foster's inverse was tested with both phantom and single-subject datasets taken with both SQUID and OPM MEG systems. We showed that Foster's inverse with SSS provides improved Phantom dipole localization and GOF on all datasets, and can overcome

significant sensor artifacts and noise where traditional SSS fails. Across the UCL and Kernel OPM results, Foster's with both empirical covariance and the novel OTP covariance method provide SNR improvements and sharper topographic localization of peak brain activity. Unlike SSS and the Iterative SSS method, Foster's inverse when used with SSS drastically reduces noise even in low channel count systems. However, unlike with other systems, the results with low-channel count systems reveal amplitude bias, the exact origin of which requires further investigation.

Here, we focused on the implementation of Foster's inverse with both the internal and full SSS basis, but in principle, other VSH expansion methods can be used, such as the mSSS method. Combining more adaptable SSS basis sets to Foster's may offer further improved results when analyzing on-scalp sensor systems [35]. Due to the importance of the noise covariance profile on the functionality of Foster's inverse with SSS, methods for obtaining the profile specifically for OPM and other on-scalp systems will need to be further investigated as the technology becomes more prevalent. However, preliminary investigations and results here demonstrate the functionality and power of Foster's inverse to reduce impacts from sensor noise and uncover higher spatial frequencies that are expected to be measured in more detail with on-scalp MEG systems.

Chapter 5

REMNANT MAGNETIC FIELD COMPENSATION FOR ON-SCALP MEG SYSTEMS

For the magnetic field to be measured using a linear relationship with laser amplitude modulation during optical pumping, OPM sensors must be operating in a specific regime with minimal low-frequency and DC fields present. The presence of remnant magnetic fields with nonzero gradients around the OPM sensors creates hard to remove artifacts when the patient moves through these fields, creating signals that vary in space and time similarly to how neuronal currents do. Most MSRs have a remnant field of 100 nT [54]. Even in an MSR with a much smaller background field of 30 nT, a small head rotation during data collection push the OPM sensors out of their operable range and create artifacts as the sensors move through the remnant field [3]. Therefore, new MSR technology is needed to further reduce the remnant fields as low as 5 nT, allowing for the operation of OPM sensor systems and the investigation of more naturalistic neuroscience. In this chapter, we begin with a discussion and theory of the magnetic field components inside the MSR that must be compensated. Then, we review recent coil compensation designs that have been developed and researched at, for example, the University of Nottingham. Finally, we describe the theory, modeling, design, and construction efforts towards implementing a coil compensation system for the MEG imaging center at the Institute for Learning and Brain Sciences (I-LABS), UW, Seattle. Here, we have the unique opportunity to measure human interaction simultaneously recording on a SQUID MEG and OPM MEG system in the same room; however, the fields generated from the SQUID MEG system itself are a unique problem that must be compensated for with the design of the I-LABS compensation system.

5.1 Components of the Magnetic Field

We can find the components and first-order gradients of the magnetic field inside the MSR by first asserting that the area is a current free volume ($\mathbf{J} = 0$). The remnant field can be written in terms of a magnetic scalar potential $\mathbf{B}(x, y, z) = -\nabla V(x, y, z)$, such that V is a solution to Laplace's equation $\nabla^2 V(x, y, z) = 0$. As discussed in Chapter 2, solutions to Laplace's equations can be expresses as a summation of spherical harmonics up to an n^{th} order. Due to the field having zero gradient and curl, we can approximate the remnant magnetic field as a summation of three spatially uniform components $\mathbf{B}_U$ and five linearly dependent gradient components $\mathbf{B}_G$ as [43]

$$\mathbf{B}(x, y, z) = \mathbf{B}_U + \mathbf{B}_G(x, y, z). \tag{5.1}$$

Using the spherical harmonic expansion, the first-order terms of V correspond to the three spatially uniform $\mathbf{B}$ components with corresponding weights α_n as

$$\mathbf{B}_U = \mathbf{B}_x + \mathbf{B}_y + \mathbf{B}_z = \alpha_1 \hat{\mathbf{x}} + \alpha_2 \hat{\mathbf{y}} + \alpha_3 \hat{\mathbf{z}}. \tag{5.2}$$

Similarly, the first-order gradients making up $\mathbf{B}_G(x, y, z)$ have the following symmetries based on the requirements of the form of V and $\mathbf{B}$ in a current-free volume [43], [25].

$$\begin{aligned}
\frac{dB_x}{dy} &= \frac{dB_y}{dx} \\
\frac{dB_x}{dz} &= \frac{dB_z}{dx} \\
\frac{dB_y}{dz} &= \frac{dB_y}{dy} \\
\frac{dB_x}{dx} &= -\frac{dB_y}{dy} \\
\frac{dB_z}{dz} &= -\frac{1}{2}\left(\frac{dB_x}{dx} + \frac{dB_y}{dy}\right)
\end{aligned} \tag{5.3}$$

Thus, there are eight degrees of freedom, from the three components and five gradient conditions of the magnetic field described above. Any compensation system must have enough coils or tunable components to compensate for these degrees of freedom to achieve a null magnetic field free from first-order gradients.

5.2 Current Coil Compensation Systems

The general concept behind each different coil compensation design is the same: create some magnetic field that can null each of the components of the magnetic field and their first-order gradients within the room. This compensation field can be created from any number of wound coils with current flowing through them in any shape at any location surrounding the sensors. The trick is to find the most optimal position, shape, and current for each coil, while maintaining physically possible configurations and safe operating conditions for the MEG sensors. Magnetic field compensation can also be controlled in real time, where reference sensors are used to measure the magnetic field around the MEG helmet, and in-time updates can be made to the current through the coils in order to dynamically null the magnetic field in the MSR [23]. Field nulling is particularly important when allowing the patient to move around as much as possible, thus necessitating a volume of null magnetic field that can move around to keep the helmet within it with the addition of an infrared camera system to track head position [23],[25]. Here, we discuss a few proposed current coil compensation system designs, focusing on the mathematical and physical basis for the coil shapes and specifications, as well as the necessary hardware for successfully implementing each design during data collection.

5.2.1 Bi-Planar Coil Systems

A simpler starting place to the coil compensation problem is the bi-planar design, where compensation coils are confined to two symmetrical planes on either side of the MEG sensor system. Bi-planar designs have been successfully employed for MRI design to generate tunable

field gradients in just one component of the magnetic field. The goal is to create coils that generate magnetic fields to compensate and null the three cartesian magnetic field components B_x, B_y, B_z and the three first-order gradients dB_x/dz, dB_y/dz, and dB_z/dz, which are the dominant components of the expansion [43], [22]. Bi-Planar coils can be designed by finding the stream function $S(x, y)$, which is the two-dimensional surface current density $\mathbf{J}$. The magnetic vector potential $\mathbf{A}(\mathbf{r})$ generated from the current density $\mathbf{J}(\mathbf{r}')$ is given by [29]

$$\mathbf{A}(\mathbf{r}) = \frac{\mu_0}{4\pi} \int \frac{\mathbf{J}(\mathbf{r}')}{|\mathbf{r} - \mathbf{r}'|} \mathrm{d}^3\mathbf{r}' \tag{5.4}$$

.

Given that $\nabla \mathbf{J} = 0$, the stream function confined to the xy-plane is defined as $\nabla S \times \hat{\mathbf{z}}$. Stream functions are generally used to describe the flow of liquids, but can be used in electromagnetism when current is considered the flow of liquid. Then, the stream function can be parameterized as a two-dimensional Fourier series on the two bi-planar coil planes as

$$S(x, y) = \sum_{n=1}^{N} \left[\alpha_n \cos\left(\frac{\pi x}{2L}(2n-1)\right) + \beta_n \sin\left(\frac{\pi n x}{L}\right) \right] \times \sum_{m=1}^{M} \left[\gamma_m \cos\left(\frac{\pi y}{2L}(2m-1)\right) + \delta_n \sin\left(\frac{\pi m x}{L}\right) \right] \tag{5.5}$$

where L is half the side of one square plane, $|x|, |y| < L$, and $\alpha_n, \beta_n, \gamma_m$, and δ_m are the harmonic components weights [22]. The next step is to exploit the expected symmetries that arise from the bi-planar design. For example, for a coil tuning the x-component of the field (B_x-coil), the stream function must be symmetric in x and y, but anti-symmetric in z. Thus, the stream function becomes

$$S(B_x) = \sum_{n=1}^{N} \sum_{m=1}^{M} \left[\lambda_{nm} \sin\left(\frac{\pi n x}{L}\right) \cos\left(\frac{\pi y}{2L}(2m-1)\right) \right] \tag{5.6}$$

From here, the two-dimensional Fourier transform of $S(B_x)$ can be used to find the coil's contribution to the field. The values for λ_{lm}, related to the currents through each coil,

are found by minimizing the difference between the desired field B_x at position $\mathbf{r}_i$ and the calculated field $b_x(\mathbf{r}_\mathrm{i})$ based on the functional F shown below.

$$F = \sum_{i=1}^{I} |B_x(\mathbf{r}_i) - b_x(\mathbf{r}_i)|^2 + \omega P \tag{5.7}$$

where P and ω are tunable power dissipation terms used to reduce the complexity of the coil designs to make construction straightforward [22]. Once the stream function is optimized, the compensation coil wire paths are placed along the contours of the stream function across each plane. An example of the B_x coil for one side of the bi-planar system, calculated in Matlab using methodology developed by Holmes et al. [22] is included in Figure 5.1.

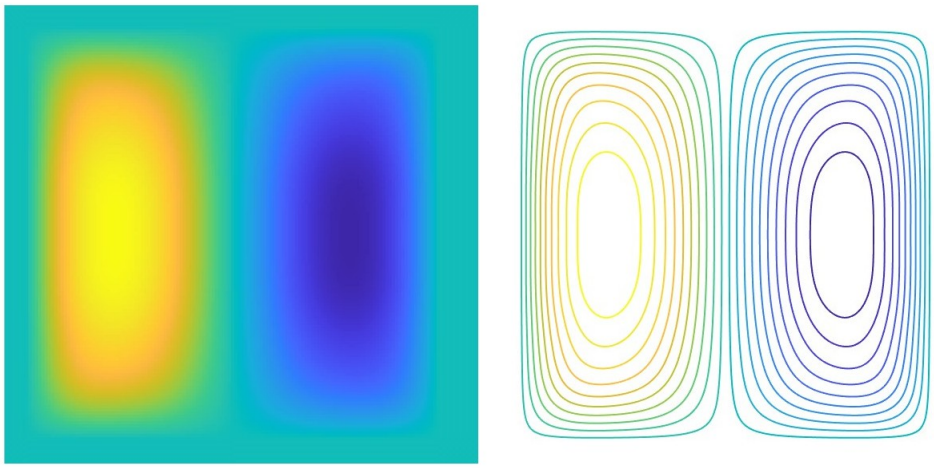

Figure 5.1: Left: The stream function contour used to create magnetic fields that tune the x-component of the field. Right: The optimized coil compensation wire paths following the contours of the stream function. Plots are generated using Matlab code provided by and adapted from Holmes et al. [22]

Similar calculations are done for the B_y and B_z coils, and first-order gradients, resulting in a total of six coils for the bi-planar construction. When the length of one side of the square bi-planar coil is 1.6 m (L =0.8 m) and the planes are 1.5 m apart, the bi-planar system creates a null magnetic field volume that is 0.4 m^3, which is large enough to fit an on-scalp

MEG sensor system and accounts for some natural head movement [22], but is primarily a static field compensation design using consistent currents driving the compensation coils throughout the measurement.

By exploiting further symmetries expected due to the bi-planar system, the six coil design can be reduced to three coils where each coil pair is designed to simultaneously produce a homogeneous field and homogeneous gradient in the central null volume [25]. This can be done by adding another term to the functional F which explicitly minimizes the spatial deviations of the gradients g_x

$$F = \sum_{i=1}^{I} |B_t(\mathbf{r}_i) - b_x(\mathbf{r}_i)|^2 + \alpha \sum_{i=1}^{I} |g_t z_i - g_x(\mathbf{r}_i)|^2 + \omega P \tag{5.8}$$

where $g_t z_i$ is the desired target gradient for $G_x \approx dB_x/dz$ and $g_x(\mathbf{r}_i) = \sum_j \lambda_j g_{xj}(\mathbf{r}_i)$ is the calculated field at position $\mathbf{r}_i$ [25]. The parameter α can be adjusted to balance the relative strength of the gradient components with the field components, and the coefficients λ_j are used for minimization by solving for $dF/d\lambda_j = 0$ [25]. Adding the additional gradient terms into the functional for minimization simplifies the final coil design; however, the bi-planar systems still cannot handle subject movement that takes the OPM helmet outside of the 0.4 m^3 null volume. Additionally, stream function designs are limited by the discretization of the wire topographies over the continuous stream on each plane. Finally, bi-planar designs compensate for uniform magnetic fields, whereas fields in the MSR may contain nonuniform characteristics. But, it has been shown that bi-planar coil designs are effective with remnant fields with less than 5% non-uniformity [60].

5.2.2 Dynamic, Full Room Compensation Systems

New MSR and coil compensation designs go a step further than the bi-planar design with the goal of creating a dynamic system where a null magnetic field with zero first-order gradients is maintained around the OPM helmet during recording, even as the subject is free to do large movements like walk around, catch a ball, and even play instruments. Full rooms of this design are more lightweight than traditional MSR designs, and are constructed specifically

with OPM measurements in mind. Perhaps the most successful implementation of fully portable and dynamic shielding systems have been recently designed at the Sir Peter Mansfield Imaging Center at the University of Nottingham [46], [24], [23]. In order to create a 2.4m ^{3} lightweight MSR with dynamic field compensation, the optimal current through each coil of wire was found using the Biot-Savart law, given the number, location and dimension of the coils, to first simply calculate the field generated by each coil

$$\mathbf{b}_m(\mathbf{r}_n) = \frac{\mu_0}{4\pi} \int_C \frac{I d\mathbf{l} \times \mathbf{r}'_n}{|\mathbf{r}'_n|^3} \tag{5.9}$$

which can then be superimposed to find the total magnetic field $\mathbf{B}_m(\mathbf{r}_n)$ at each location $\mathbf{r}_n$ from each of the m coils [24] as

$$\mathbf{B}_m(\mathbf{r}_n) = \sum_{m=1}^{M} i_m \mathbf{b}_m(\mathbf{r}_n). \tag{5.10}$$

From here, a forward field matrix $\mathbf{A}$ can be calculated from the measured magnetic field at each of the n points generated from the superposition of each of the m coils in the form $\mathbf{A}\boldsymbol{I} = \mathbf{b}_t$, where $\boldsymbol{I}$ is the current vector describing the current through each coil and $\mathbf{b}_t$ is the target magnetic field [24]. In order to create a volume of null magnetic field, the target field should be equal and opposite to the fields generated by the currents, which can be found using norm$\|\mathbf{A}\boldsymbol{I} - \mathbf{b}_t\|_2^2$ Constrained quadratic programming is used to solve for the minimum currents in the form of [24]

$$\min_i \left[\frac{\boldsymbol{I}^T (\mathbf{A}^T \mathbf{A}) \boldsymbol{I}}{2} + \left(-\mathbf{A}^T \mathbf{b}_t\right)^T \boldsymbol{I} \right]. \tag{5.11}$$

An additional challenge of full-room coil compensation systems is accounting for the polarization induced in the MuMetal inside the MSR walls as a response to the current driven through the compensation coils. This type of interaction causes additional magnetic fields to be produced from the MSR walls themselves, which can be large enough ($<$5 nT) to push the OPM sensors outside of their operable range unless also accounted for in the design of the

compensation system [25], [23], [3], [60]. Inside the MuMetal material with some magnetic permeability μ_r, the magnetic field $\mathbf{B}$ can be written as $\mathbf{B} = \mu_0\mu_r\mathbf{H}$ [20]. The permeability for MuMetal can be >80,000, but the permeability of the air is approximately 1, so the magnetic field must undergo an abrupt change when it reaches the MSR walls, and the tangential components of both $\mathbf{B}$ and $\mathbf{H}$ must be approximately zero at the boundary. Considering the required boundary conditions, the polarization in the MuMetal can be calculated using the method of images, where the reflected field from each coil is calculated recursively through the MuMetal [25]. The method of images can also be combined with a boundary element method using triangular meshes along the planes of the coils [60]. During simulations, the prototype coils can create reflected fields up to 10 nT in strength even when placed approximately 0.5 m away from the MSR wall, so these interactions are important to take into account when designing the full compensation system.

5.2.3 Construction and Implementation

Once the coils themselves are designed using the aforementioned methods (or others, which all utilize electromagnetism at a fundamental level), the construction involves using copper wire to trace out the paths, and wooden/plastic structures are used for support. The final step is to fine tune the current going into the coils when they are in the presence of the real remnant field inside the MSR, which may be slightly different than in simulation. This tuning can be done before the patient data collection starts by measuring the remnant field in the room and adjusting the current until the field is as close to zero as possible, or this tuning can be done continuously throughout the data collection process. Both methods require hardware to measure the field in the MSR, which is typically done using a Fluxgate or extra sets of OPM sensors used as a reference [22]. Continuous measurement and adjustment also requires tracking of the OPM helmet during measurement, which can be done using an infrared camera using markers on the helmet itself, so that the null magnetic field zone follows the position of the head Current parts for dynamic nulling are manufactured by companies like QuSpin, which is compatible with the QuSpin OPM sensors and includes compensation

coils, movement tracking systems, and current drivers [24], [23]. Fully integrated systems like this are costly, but are lightweight and overcome many barriers to entry in terms of collected human subject data with OPM systems. Dynamic nulling may be needed for data collection processes involving a lot of expected head movement, but is more complicated and expensive than static nulling.

5.3 I-LABS MEG Center Coil Compensation System Development

In this section, we draw inspiration from current field compensation techniques to develop a coil compensation system and protocol for collecting OPM data with the Flux helmet at the MEG Center, Institute for Learning and Brain Sciences, University of Washington. This chapter represents a step in the long-term, multidisciplinary goal of taking simultaneous MEG recordings of two interacting people, one wearing the MEGIN Elekta/Neuromag SQUID MEG helmet and the other wearing the Kernel Flux OPM helmet. A visualization of the two sensor systems inside the MSR at I-LABS is included in Figure 5.2 as the physical setup motivates and constrains the development of a coil compensation system specific to the I-LABS MEG center.

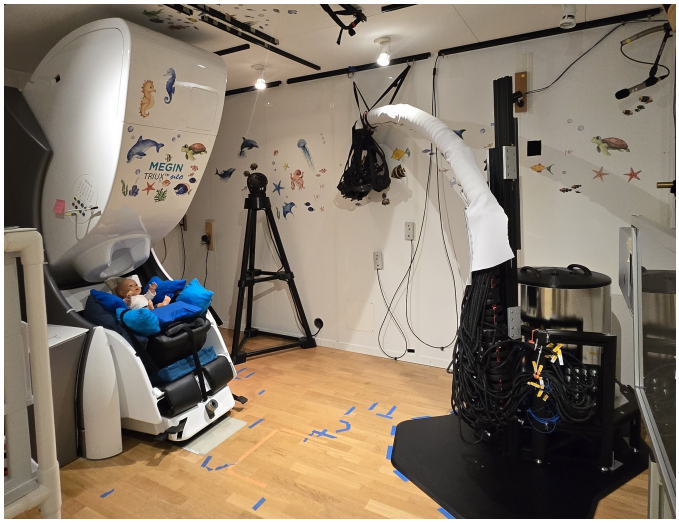

Figure 5.2: Inside the MSR at the I-LABS MEG Center, taken standing at the MSR door and looking to the left at the MEGIN Elekta/Neuromag system, with a baby doll situated in the gantry underneath the sensor helmet. On the right is the Kernel Flux OPM helmet, with a support arm and electronics doc for the laser control circuit boards.

5.3.1 Biot-Savart Modeling of Compensation Coils

In order to simulate how many compensation coils would be needed to create a null magnetic field in both first and second order components, each coil can simply be modeled using the Biot-Savart law [29]

$$\mathbf{B}(\mathbf{r}) = \frac{\mu_0}{4\pi} \int_C \frac{I d\mathbf{l} \times \mathbf{r}'}{|\mathbf{r}'|^3} \tag{5.12}$$

where I is the current through each segment or closed loop of the coil, and $\mathbf{r}'$ is the distance from the origin to the segment of current. The current, position, and shape of the compensation coils can all be simulated and optimized in order to null the magnetic field in a simulated volume around the OPM sensor system.

5.3.2 Least-Squares Minimization of Compensation Coil Design

Given a set of coils with specified size and location, we can use the least-squared minimization method to drive the magnetic field and first gradients generated by the coil set to zero by optimizing the current through each loop. Minimizing the current is ideal for ease of implementation, as well as keeping the fields are minimal as possible to not risk any adverse damage to the MSR, OPM sensor system, or other hardware within the room. Given some measured signal $\mathbf{y}$ at a point in the room, either measured with Fluxgate sensors or some MEG sensor, we can decompose the measurement into two components:

$$\mathbf{y} = \mathbf{A}\mathbf{x} + \mathbf{b} \tag{5.13}$$

where $\mathbf{A}$ is a linear transformation matrix from the coils to the sensors similar to a lead field representation, vector $\mathbf{x}$ is the coil level (current or voltage), and $\mathbf{b}$ is the remnant field inside the MSR. We can use this equation to find the least-squares solution for the optimal coil levels $\mathbf{x}_{opt}$ such that they cancel out the ambient field:

$$\mathbf{A}\mathbf{x}_{opt} = -\mathbf{b} \tag{5.14}$$

In practice, the components of matrix $\mathbf{A}$ are calculated using the magnetic field $\mathbf{B}(\mathbf{r})$ measured at several points inside the volume of interest equal to the superposition of the magnetic fields generated by each compensation coil. At each point in the volume, matrix $\mathbf{A}$ contains entries for each component of the field $\mathbf{B}_x$, $\mathbf{B}_y$, and $\mathbf{B}_z$. In practice, the components of matrix $\mathbf{A}$ are calculated using the magnetic field $\mathbf{B}(\mathbf{r})$ measured at several points inside the volume of interest equal to the superposition of the magnetic fields generated by each compensation coil. At each point in the volume, matrix $\mathbf{A}$ contains entries for each component of the field $\mathbf{B}_x$, $\mathbf{B}_y$, $\mathbf{B}_z$ and first order gradients as described in Equation 5.3. Including the gradients explicitly means they will be minimized directly, whereas not including them may still minimize them as the components themselves are driven to zero, but even small

gradients may create artifacts in the OPM sensors due to movement through the fields that are hard to remove.

5.3.3 Simulated Coil Compensation System

Due to spatial constraints inside the MSR at I-LABS, the size and location of the potential compensation coils are relatively predetermined to be 1 m^2 in size and about 2 m apart maximum in order to provide enough room around the MEGIN Elekta/Neuromag MEG system, seating area for patient parents/guardians, and room for the Flux OPM hardware. Thus, optimization of the location and size of the coils can be done, but must be heavily constrained. The largest area for optimization is to determine the currents that should be applied through each compensation coil. Additionally, the spatial restrictions pose a problem for the number of independent coils that can fit in the MSR. In principle, with the eight degrees of freedom listed in Section 5.1, eight or more independent coils are required to fully compensate the expected magnetic field in the MSR. To reduce the number of necessary compensation coils, the six active shielding coils inside the walls of the MSR as seen in Figure 5.3, manufactured by Imedco, can be used as a part of the coil compensation system. In principle, this means only three extra coils are needed to fully compensate the remnant field. An example showing the placement of these three coils is seen in Figure 5.4.

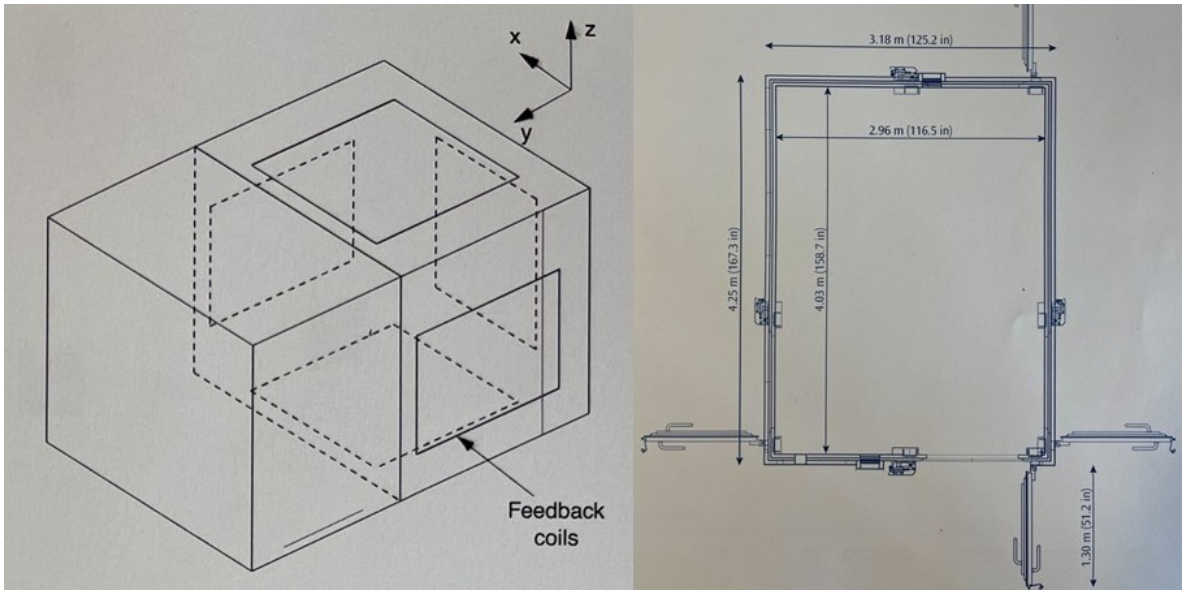

Figure 5.3: Left: The approximate location of the six active compensation coils located inside the Imedco MSR walls. Right: dimensions of the MSR walls showing the size of the coils (not including the front coil, due to the MSR door). Schematics are from the Imedco installation notes at the I-LABS archives.

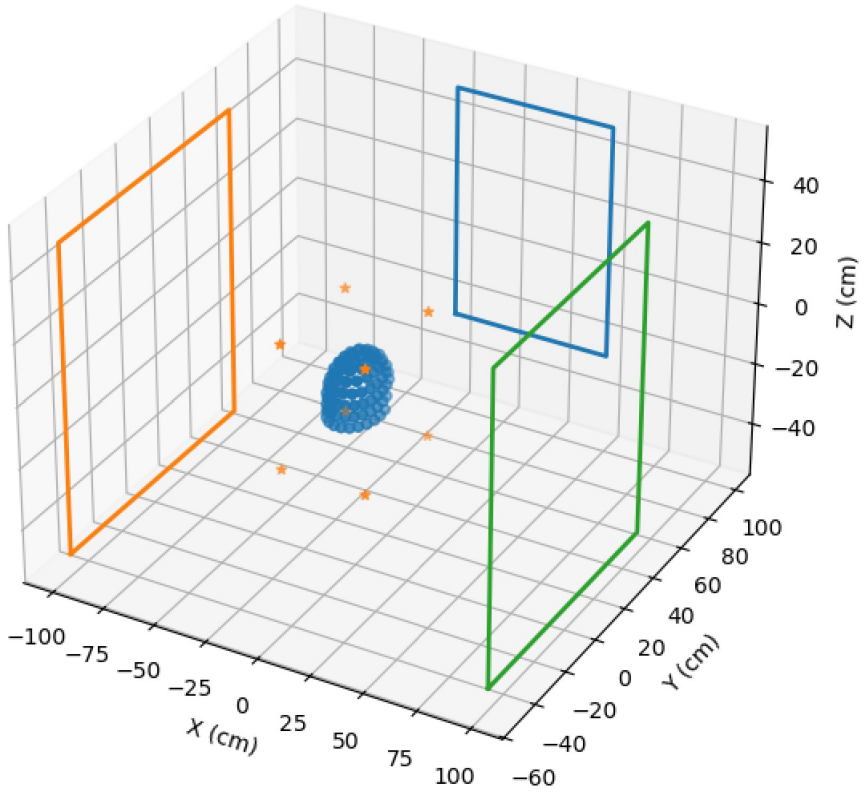

Figure 5.4: Visualization of the simulated three compensation coils to be used in conjunction with the six MSR wall coils. The right and left coils (orange and green) are 1 m^2 in area and are 2 m apart from each other. The front coil (blue) is 0.5 m^2 to accommodate the arm of the OPM helmet. The fields produced by the coils are optimized to create a null magnetic field within a 0.4 m^3 volume outlined by the orange points, surrounding the sensor helmet (blue circles).

The optimal currents through the least-squares optimization of Equation 5.14 were found for the three-coil design shown in Figure 5.4 using a background field of $\boldsymbol{b}$ = 100 nT in Python. These currents are -46.5 mA through the left coil, 0.29 mA through the front coil, and 175 mA through the right coil. For safety reasons, the current through each coil wire should be maximum 100 mA, but the calculated fields can also be achieved by increasing the number of turns of wire through the coil. As a basic check, the least-squares method of

solving the currents through the 3-coil design gave reasonable results for a system capable of compensating remnant magnetic fields of around 100 nT.

5.3.4 Construction of Coil Compensation System

Regardless of the final pattern of the compensation coil wires, we need multiple stands to mount the coils. The stands are designed to be lightweight, easy to move, adjustable in height, and utilize a plastic plane for ease of adjusting the wire patterns as they may evolve with further design iterations. The frame is made of aluminum for compatibility and safe use within the magnetically shielded room. An example of one of the three stands and the three contours of magnetic field lines on the plane can be seen in Figure 5.5. The contours are calculated based on the stream function method, using the fields and gradients directly measured from the magnetically shielded room to specify the target function.

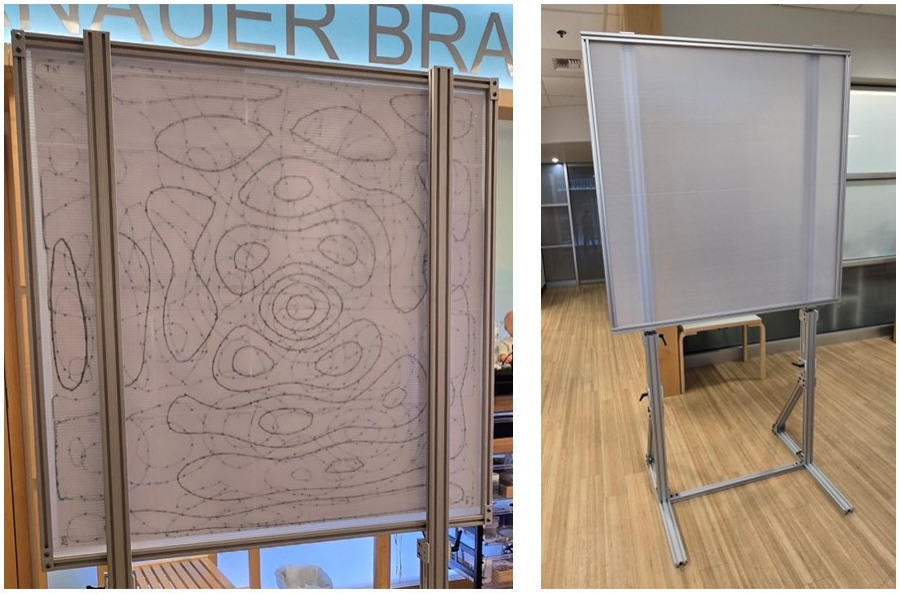

Figure 5.5: One of the three planned coil stands used to mount the compensation coil wire. This stand houses a plane of 1 m^2 and will be placed on either side of the Kernel Flux OPM helmet. The contours for the wire paths are printed and taped to the stand to be traced with wire.

The next step is to transfer the contour lines of the magnetic fields generated by each plane into one contiguous line to be followed by wire. This is done for each of the three contours per plane (black, green, and blue) for a total of three wires and three different currents per plane. An example of the black contour and resulting wire pattern is shown in Figure 5.6

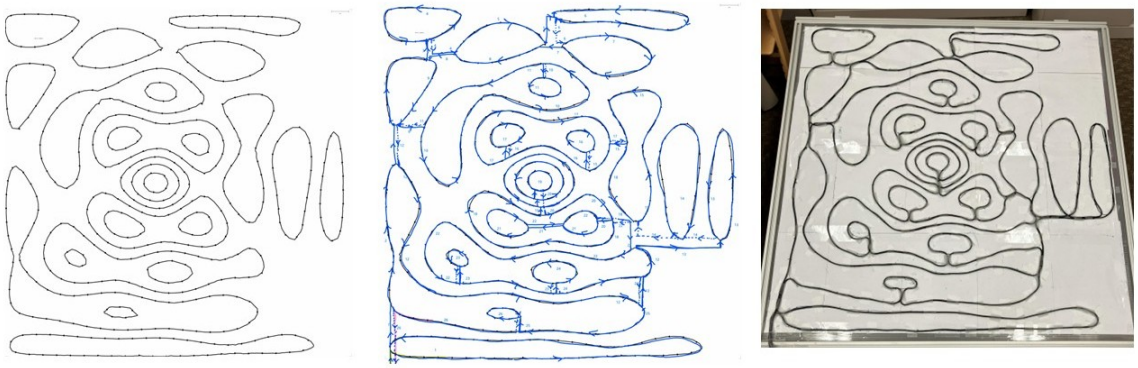

Figure 5.6: Example of the wiring process from left to right: contour of the necessary magnetic field, connected the contours with one continuous line, following the line with wire.

Connections between contour lines with the wire are kept perpendicular and as close together as possible to mitigate any introduction of extra magnetic fields generated by the final plane. In this fashion, the other three wires per plane, totaling in 9 paths across 3 planes, can be created and tested to verify functionality and field suppression capabilities.

5.4 Further Comments

In this chapter, we have compiled the most recent designs for coil compensation systems that are able to lower the magnetic fields inside the MSR to below 5 nT. Each design is unique with its own advantages and disadvantages, but they all can assist in OPM measurements with movement through the remnant fields. From these current designs, we have drawn inspiration for a coil compensation system designed specifically for the constraints and

projects at the MEG Imaging Center, I-LABS. By using a combination of the steam function method with a least-squares optimization with a 3-coil design, compensation of a typical 100 nT MSR background field was successfully compensated in simulation with reasonable optimized currents through each coil. However, this design does not account for any potential interactions with the MuMetal walls. As mentioned previously, simulations with the coil prototypes revealed that the MuMetal responds with significant magnetic fields, which additionally add to the remnant field in the MSR that must be compensated for. These fields are a function of the current going through the prototype coils, which needs to be taken into account when optimizing and constraining the currents through the compensation coils. This effect can be accounted for in the least-squares paradigm by expanding matrix $\mathbf{A}$ to include the MuMetal response

$$(\mathbf{A}_{MSR} + \mathbf{A}(\mathbf{x}_{opt}))\,\mathbf{x}_{opt} = -\mathbf{b} \tag{5.15}$$

Where $\mathbf{A}_{MSR}$ is the lead field of the six wall coils in the MSR, which remain constant during optimization, while $\mathbf{A}(\mathbf{x}_{opt})$ is the lead field of the three additional compensation coils, which includes the added field generated by the MuMetal walls as a function of the current $\mathbf{x}_{opt}$. Future work with coil compensation designs should include this interaction, and may also need to utilize the method of images to fully characterize the interactions with the MuMetal. Furthermore, the coil design may need to be optimized for more complex forms of inhomogeneous magnetic fields within the MSR to account for the expansion of OPM measurements that require a large null volume and dynamic compensation.

As the exact coil design may be subject to change, the stands used to mount the coils were created to maximize the ease of use for testing different potential patterns or making future adjustments. The first constructed stand and beginnings of wiring and testing featured in Figure 5.5 and Figure 5.6 marks the first step from simulation to reality with the implementation of the coil compensation system at I-LABS.

Chapter 6

CONCLUSION

In this dissertation, we presented novel solutions to address the new challenges and capitalize on new opportunities that are unique to on-scalp MEG sensor systems. On-scalp systems are an exciting frontier in naturalistic neuroscience investigations; however, we require improvements to the methodology and instrumentation of MEG to realize the full potential of on-scalp systems.

First, we presented the novel mSSS method, a straightforward mathematical adaptation to the SSS method that ensures the full brain space is represented by the interior basis, even when the MEG sensors are on the scalp. A single-origin VSH expansion fails to encompass the full brain when the sensors are too close to the scalp, a problem which is solved using multiple origins of overlapping VSH expansions to dynamically span the brain through the mSSS method. Through simulation, we demonstrated that the mSSS method accurately reconstructs internal current dipole signals originating close to the sensors whereas the traditional SSS basis fails to capture the full signal, as seen in a six-fold increase in subspace angle between the SSS basis and the surface current dipole while the mSSS subspace angle remains stable below 1° for all dipole locations. Through the analysis of empty-room MSR recordings, we showed that the mSSS basis has the best ability to lower the noise floor of the data for both a 5-layer and lightweight MSR construction at the University of Nottingham. Finally, using single-subject data collected with the Flux OPM system at UW and with the QuSpin OPM system at UCL, we concluded that the novel mSSS basis results in the best reconstruction of internal brain activity compared to the SSS basis and the spheroidal harmonic constructions. Therefore, the mSSS method is a successful and novel adaptation to reconstruct sources from the brain recorded using on-scalp MEG systems.

Second, we focused on the optimization of the basic magnetic field components extraction by adapting Foster's matrix inversion protocol to the SSS method. Sensor noise covariance profiles may be hard to obtain for newer OPM sensor systems, but we discussed the importance of obtaining an accurate representation of the sensor noise covariance profile in order to obtain the best component extraction while avoiding signal biasing, as well as examined possible methods for obtaining estimates of noise covariance profiles. The functionality of Foster's inverse with SSS was verified using current dipole simulations, where we showed a 10-times increase in SNR between the traditional and iterative SSS reconstruction and the Foster's reconstructed data. Next, the investigation of four Phantom datasets collected with the MEGIN/Elekta Neuromag system at I-LABS showed that Foster's inverse offers the smallest errors when localizing known current dipole sources, and is able to overcome sensor noise and artifacts when traditional SSS fails. Finally, Foster's inverse with two methods for estimating the sensor noise covariance matrix were tested with two single-subject investigations taken with two OPM systems: the UCL OPM system and the Kernel Flux system. The first method, the empirical covariance, is found using the default compute covariance functionality in MNE-Python, and the second method uses the residual signal from subtracting the OTP cleaned data from the noisy raw data, leading just the sensor noise. In this investigation, with both methods of covariance, the Foster's inverse with SSS recovers more fine spatial topographies from the higher frequency components of the neuronal magnetic fields than SSS alone, and offers improved SNR. Our investigation highlights the importance of exact knowledge of the sensor noise, so future work may be needed to sufficiently estimate the sensor noise, specifically with the additions of new and different on-scalp MEG systems.

Finally, we addressed the sensitivity of OPM sensors to low-frequency and DC magnetic fields that are present in the MSR despite the active and passive shielding hardware. These fields are not an issue for traditional SQUID MEG systems, so new field compensation methods are needed to reduce the fields in the MSR further, down as low as 5 nT, into the operating range of OPM sensors. At I-LABS, we have a unique opportunity to take simultaneous recordings between two people, one in the SQUID system and one in the OPM

system, but we also have the unique problem of accounting for the extra fields generated by the SQUID system itself. We discussed various state of the art coil compensation systems developed recently, then presented a simulated compensation system designed for the MSR at I-LABS to compensate for the 100 nT remnant field inside the MSR. Three coils mounted to the right, left, and front of the OPM system were simulated using the Biot-Savart law and the optimal currents through each coil were found using the least-squares method. The design and beginning construction of the coil compensation system is an important step towards more successful subject studies using the Kernel Flux OPM system at I-LABS.

Each chapter of this dissertation presents improvements to the methodology and instrumentation of on-scalp MEG systems for the larger goal of expanding the precision and breadth of human brain studies.

BIBLIOGRAPHY

[1] Felix M. Arscott. CHAPTER VIII - THE SPHEROIDAL WAVE EQUATION. In Felix M. Arscott, editor, *Periodic Differential Equations*, pages 153–190. Pergamon, January 1964.

[2] Elena Boto, Niall Holmes, James Leggett, Gillian Roberts, Vishal Shah, Sofie S. Meyer, Leonardo Duque Muñoz, Karen J. Mullinger, Tim M. Tierney, Sven Bestmann, Gareth R. Barnes, Richard Bowtell, and Matthew J. Brookes. Moving magnetoencephalography towards real-world applications with a wearable system. *Nature*, 555(7698):657–661, March 2018. Publisher: Nature Publishing Group.

[3] Matthew J. Brookes, James Leggett, Molly Rea, Ryan M. Hill, Niall Holmes, Elena Boto, and Richard Bowtell. Magnetoencephalography with optically pumped magnetometers (OPM-MEG): the next generation of functional neuroimaging. *Trends in Neurosciences*, 45(8):621–634, August 2022.

[4] Maggie Clarke, Alexis Bosseler, Julia Mizrahi, Erica Peterson, Eric Larson, Andrew Meltzoff, Patricia Kuhl, and Samu Taulu. Human Brain Mapping | Neuroimaging Journal | Wiley Online Library, March 2022.

[5] B. Neil Cuffin and David Cohen. Magnetic Fields of a Dipole in Special Volume Conductor Shapes. *IEEE Transactions on Biomedical Engineering*, BME-24(4):372–381, July 1977.

[6] Anders M Dale, Arthur K Liu, Bruce R Fischl, Randy L Buckner, John W Belliveau, Jeffrey D Lewine, and Eric Halgren. Mapping: Combining fMRI and MEG for High-Resolution Imaging of Cortical Activity. 2000.

[7] Alain de Cheveigné and Jonathan Z. Simon. Sensor noise suppression. *Journal of neuroscience methods*, 168(1):195–202, February 2008.

[8] ELEKTA. Elekta Neuromag Technical Manual, Revision G, September 2005.

[9] Denis A. Engemann and Alexandre Gramfort. Automated model selection in covariance estimation and spatial whitening of MEG and EEG signals. *NeuroImage*, 108:328–342, March 2015.

[10] K. B. Fisher, O. Lahav, Y. Hoffman, D. Lynden-Bell, and S. Zaroubi. Wiener reconstruction of density, velocity and potential fields from all-sky galaxy redshift surveys. *Monthly Notices of the Royal Astronomical Society*, 272(4):885–908, February 1995.

[11] Manus Foster. An Application of the Wiener-Kolmogorov Smoothing Theory to Matrix Inversion. *Journal of the Society for Industrial and Applied Mathematics*, 9(3):387–392, September 1961. Publisher: Society for Industrial and Applied Mathematics.

[12] Toshio Fukushima. PROLATE SPHEROIDAL HARMONIC EXPANSION OF GRAVITATIONAL FIELD. *The Astronomical Journal*, 147(6):152, May 2014. Publisher: The American Astronomical Society.

[13] Gene Howard Golub and Charles F. Van Loan. *Matrix Computations*. JHU Press, February 2013. Google-Books-ID: X5YfsuCWpxMC.

[14] Alexandre Gramfort, Martin Luessi, Eric Larson, Denis Engemann, Daniel Strohmeier, Christian Brodbeck, Roman Goj, Mainak Jas, Teon Brooks, Lauri Parkkonen, and Matti Hämäläinen. MEG and EEG data analysis with MNE-Python. *Frontiers in Neuroscience*, 7, 2013.

[15] Laura Gwilliams, Graham Flick, Alec Marantz, Liina Pylkkänen, David Poeppel, and Jean-Rémi King. Introducing MEG-MASC a high-quality magneto-encephalography dataset for evaluating natural speech processing. *Scientific Data*, 10(1):862, December 2023. Publisher: Nature Publishing Group.

[16] Riitta Hari, Sylvain Baillet, Gareth Barnes, Richard Burgess, Nina Forss, Joachim Gross, Matti Hämäläinen, Ole Jensen, Ryusuke Kakigi, François Mauguière, Nobukatzu Nakasato, Aina Puce, Gian-Luca Romani, Alfons Schnitzler, and Samu Taulu. IFCN-endorsed practical guidelines for clinical magnetoencephalography (MEG). *Clinical Neurophysiology: Official Journal of the International Federation of Clinical Neurophysiology*, 129(8):1720–1747, August 2018.

[17] Liisa Helle, Jukka Nenonen, Eric Larson, Juha Simola, Lauri Parkkonen, and Samu Taulu. Extended Signal-Space Separation Method for Improved Interference Suppression in MEG. *IEEE Transactions on Biomedical Engineering*, 68(7):2211–2221, July 2021. Conference Name: IEEE Transactions on Biomedical Engineering.

[18] Roland Herzog, Frederik Köhne, Leonie Kreis, and Anton Schiela. Frobenius-Type Norms and Inner Products of Matrices and Linear Maps with Applications to Neural Network Training, November 2023. arXiv:2311.15419.

[19] Ryan M. Hill, Gonzalo Reina Rivero, Ashley J. Tyler, Holly Schofield, Cody Doyle, James Osborne, David Bobela, Lukas Rier, Joseph Gibson, Zoe Tanner, Elena Boto, Richard Bowtell, Matthew J. Brookes, Vishal Shah, and Niall Holmes. Determining sensor geometry and gain in a wearable MEG system, October 2024. arXiv:2410.08718 [physics].

[20] J.F. Hoburg. Principles of quasistatic magnetic shielding with cylindrical and spherical shields. *IEEE Transactions on Electromagnetic Compatibility*, 37(4):574–579, November 1995.

[21] Niall Holmes, Richard Bowtell, Matthew J. Brookes, and Samu Taulu. An Iterative Implementation of the Signal Space Separation Method for Magnetoencephalography Systems with Low Channel Counts. *Sensors*, 23(14):6537, January 2023. Number: 14 Publisher: Multidisciplinary Digital Publishing Institute.

[22] Niall Holmes, James Leggett, Elena Boto, Gillian Roberts, Ryan M. Hill, Tim M. Tierney, Vishal Shah, Gareth R. Barnes, Matthew J. Brookes, and Richard Bowtell. A bi-planar coil system for nulling background magnetic fields in scalp mounted magnetoencephalography. *NeuroImage*, 181:760–774, November 2018.

[23] Niall Holmes, James Leggett, Ryan M. Hill, Lukas Rier, Elena Boto, Holly Schofield, Tyler Hayward, Eliot Dawson, David Woolger, Vishal Shah, Samu Taulu, Matthew J. Brookes, and Richard Bowtell. Wearable magnetoencephalography in a lightly shielded environment. *IEEE Transactions on Biomedical Engineering*, pages 1–10, 2024. Conference Name: IEEE Transactions on Biomedical Engineering.

[24] Niall Holmes, Molly Rea, James Chalmers, James Leggett, Lucy J. Edwards, Paul Nell, Stephen Pink, Prashant Patel, Jack Wood, Nick Murby, David Woolger, Eliot Dawson, Christopher Mariani, Tim M. Tierney, Stephanie Mellor, George C. O'Neill, Elena Boto, Ryan M. Hill, Vishal Shah, James Osborne, Rosemarie Pardington, Peter Fierlinger, Gareth R. Barnes, Paul Glover, Matthew J. Brookes, and Richard Bowtell. A lightweight magnetically shielded room with active shielding. *Scientific Reports*, 12(1):13561, August 2022. Publisher: Nature Publishing Group.

[25] Niall Holmes, Tim M. Tierney, James Leggett, Elena Boto, Stephanie Mellor, Gillian Roberts, Ryan M. Hill, Vishal Shah, Gareth R. Barnes, Matthew J. Brookes, and Richard Bowtell. Balanced, bi-planar magnetic field and field gradient coils for field compensation in wearable magnetoencephalography. *Scientific Reports*, 9(1):14196, October 2019. Publisher: Nature Publishing Group.

[26] Mingxiong Huang, Mårten Risling, and Dewleen G. Baker. The role of biomarkers and MEG-based imaging markers in the diagnosis of post-traumatic stress disorder and blast-induced mild traumatic brain injury. *Psychoneuroendocrinology*, 63:398–409, January 2016.

[27] Matti Hämäläinen, Riitta Hari, Risto J. Ilmoniemi, Jukka Knuutila, and Olli V. Lounas-

maa. Magnetoencephalography—theory, instrumentation, and applications to noninvasive studies of the working human brain. *Reviews of Modern Physics*, 65(2):413–497, April 1993.

[28] Risto Ilmoniemi. The triangle phantom in magnetoencephalography. *J Jpn Biomagn Bioelectromagn Soc*, 22:44–45, January 2009.

[29] Risto J. Ilmoniemi and Jukka Sarvas. *Brain Signals: Physics and Mathematics of MEG and EEG*. MIT Press, May 2019. Google-Books-ID: wZiWDwAAQBAJ.

[30] Andrew V. Knyazev and Merico E. Argentati. Principal Angles between Subspaces in an A -Based Scalar Product: Algorithms and Perturbation Estimates. *SIAM Journal on Scientific Computing*, 23(6):2008–2040, January 2002.

[31] Eric Larson, Alexandre Gramfort, Denis A Engemann, Jaakko Leppakangas, Christian Brodbeck, Mainak Jas, Teon L Brooks, Jona Sassenhagen, Daniel McCloy, Martin Luessi, Jean-Rémi King, Richard Höchenberger, Roman Goj, Clemens Brunner, Guillaume Favelier, Marijn van Vliet, Mark Wronkiewicz, Alex Rockhill, Chris Holdgraf, Mathieu Scheltienne, Joan Massich, Stefan Appelhoff, Yousra Bekhti, Alan Leggitt, Andrew Dykstra, Romain Trachel, Robert Luke, Lorenzo De Santis, Asish Panda, Mikołaj Magnuski, Britta Westner, Dan G Wakeman, Daniel Strohmeier, Hari Bharadwaj, Tal Linzen, Alexandre Barachant, Emily Ruzich, Christopher J Bailey, Adam Li, Clément Moutard, Luke Bloy, Fede Raimondo, Jussi Nurminen, Martin Billinger, Jair Montoya, Marmaduke Woodman, Scott Huberty, Ingoo Lee, Martin Schulz, Nick Foti, Cathy Nangini, José C García Alanis, Dimitri Papadopoulos Orfanos, Olaf Hauk, Ross Maddox, Roan LaPlante, Ashley Drew, Christoph Dinh, Guillaume Dumas, Martin, Johann Benerradi, Thomas Hartmann, Eduard Ort, Martin Billinger, Paul Pasler, Stefan Repplinger, Alexander Rudiuk, Ana Radanovic, Brad Buran, Jacob Woessner, Mathurin Massias, Matti Hämäläinen, Praveen Sripad, Valerii Chirkov, Christopher Mullins, Félix Raimundo, Michiru Kaneda, Phillip Alday, Ram Pari, Simon Kornblith, Yaroslav Halchenko, Yu-Han Luo,

Alexandre Gramfort, Johannes Kasper, Keith Doelling, Mads Jensen, Tanay Gahlot, Thomas S Binns, Adonay Nunes, Dirk Gütlin, Erkka Heinila, Kristijan Armeni, kjs, Alejandro Weinstein, Camilo Lamus, Catalina María Galván, Cristóbal Moënne-Loccoz, Dmitrii Altukhov, Erica Peterson, Jevri Hanna, Jon Houck, Natalie Klein, Paul Roujansky, Rob Luke, Santeri Ruuskanen, Simon Kern, Antti Rantala, Burkhard Maess, Carina Forster, Christian O'Reilly, Dominik Welke, Henrich Kolkhorst, Hubert Banville, Jack Zhang, Kostiantyn Maksymenko, Maggie Clarke, Matteo Anelli, Nikolai Chapochnikov, Pierre-Antoine Bannier, Saket Choudhary, Cora Kim, Felix Klotzsche, Fu-Te Wong, Ivana Kojcic, Jesper Duemose Nielsen, Kaisu Lankinen, Kambiz Tabavi, Louis Thibault, Moritz Gerster, Nabil Alibou, Nathalie Gayraud, Nick Ward, Sophie Herbst, Victor Férat, Ana Radanovic, Andrew Quinn, Antoine Gauthier, Basile Pinsard, Dominik Welke, Emily Stephen, Erik Hornberger, Evan Hathaway, Evgenii Kalenkovich, Fahimeh Mamashli, Gennadiy Belonosov, George O'Neill, Giorgio Marinato, Hafeza Anevar, Hamza Abdelhedi, Jan Sosulski, Jeff Stout, Joshua Calder-Travis, Judy D Zhu, Larry Eisenman, Lorenz Esch, Marian Dovgialo, Nicolas Barascud, Nicolas Legrand, Nikolai Kapralov, Qian Chu, Rotem Falach, Samuel Deslauriers-Gauthier, Silvia Cotroneo, Steve Matindi, Steven Bierer, Thomas Samuel Binns, Tristan Stenner, Victoria Peterson, Zvi Baratz, Alessandro Tonin, Alexander Kovrig, Annalisa Pascarella, Apoorva Karekal, Carlos de la Torre, Chetan Gohil, Christina Zhao, Dominik Krzemiński, Dominique Makowski, Ezequiel Mikulan, Florian Hofer, Jean-Baptiste Schiratti, Jen Evans, John Veillette, Jordan Drew, Joshua Teves, Kyle Mathewson, Laura Gwilliams, Lenny Varghese, Liberty Hamilton, Lukas Gemein, Lukas Hecker, Lx37, Mats van Es, Matt Boggess, Matthias Eberlein, Michal Žák, Mohamed Sherif, Nataliia Kozhemiako, Naveen Srinivasan, Niklas Wilming, Oleh Kozynets, Peter J Molfese, Pierre Ablin, Proloy Das, Quentin Bertrand, Reza Shoorangiz, Richard Scholz, Rodrigo Hübner, Sara Sommariva, Sena Er, Sheraz Khan, Sumalyo Datta, Theodore Papadopoulo, Thomas Donoghue, Thomas Jochmann, Timon Merk, Tod Flak, Tom Dupré la Tour, Tziona NessAiver, akshay0724, sviter, Aaron Earle-Richardson, Abram Hindle, Achilleas Koutsou, Adeline

Fecker, Adina Wagner, Alex Ciok, Alex Lepauvre, Alexander Kiefer, Andy Gilbert, Aniket Pradhan, Anna Padee, Anne-Sophie Dubarry, Anton Nikolas Waniek, Archit Singhal, Ariel Rokem, Arne Pelzer, Austin Hurst, Ben Beasley, Bruno Nicenboim, Carlos de la Torre, Christian Clauss, Christian Mista, Chun-Hui Li, Claire Braboszcz, Daniel C Schad, Daniel Hasegan, Daniel Tse, Darin Erat Sleiter, David Haslacher, David Sabbagh, Demetres Kostas, Desislava Petkova, Dinara Issagaliyeva, Diptyajit Das, Dominik Wetzel, Eberhard Eich, Elizabeth DuPre, Ellen Lau, Emanuele Olivetti, Enrico Varano, Enzo Altamiranda, Eric Brayet, Etienne de Montalivet, Evgeny Goldstein, Fahimeh Mamashli, Farzin Negahbani, Federico Zamberlan, Florin Pop, Frederik D Weber, Gansheng Tan, Geoff Brookshire, George O'Neill, Giulio, Gonzalo Reina, Hamid Maymandi, Hasrat Ali Arzoo, Hermann Sonntag, Hongjiang Ye, Hyonyoung Shin, Hüseyin Orkun Elmas, Ilian AZZ, Ilias Machairas, Ivan Zubarev, Ivo de Jong, Jacob Phelan, Jakub Kaczmarzyk, Jan Zerfowski, Jasper J F van den Bosch, Jeroen Van Der Donckt, Johan van der Meer, Johannes Niediek, Josh Koen, Joshua J Bear, Juergen Dammers, Julia Guiomar Niso Galán, Julius Welzel, Katarina Slama, Katrin Leinweber, Laetitia Grabot, Lau Møller Andersen, Leonardo Rochael Almeida, Leonardo S Barbosa, Lorenzo Alfine, Lukáš Hejtmánek, Maksym Balatsko, Manfred Kitzbichler, Manoj Kumar, Manorama Kadwani, Manu Sutela, Marcin Koculak, Mark Henney, Martin BaBer, Martin Oberg, Martin van Harmelen, Matt Courtemanche, Matt Tucker, Matteo Visconti di Oleggio Castello, Matthias Dold, Matti Toivonen, Maureen Shader, Mauricio Cespedes, Michael Krause, Milan Rybář, Mingjian He, Mohammad Daneshzand, Nicolas Fourcaud-Trocmé, Nicolas Gensollen, Nicole Proulx, Niels Focke, Nikolas Chalas, Noah Markowitz, Omer Shubi, Pablo Mainar, Padma Sundaram, Pedro Silva, Quanliang Li, Quentin Barthélemy, Rahul Nadkarni, Ramiro Gatti, Ramonapariciog Apariciogarcia, Rasmus Aagaard, Reza Nasri, Richard Koehler, Riessarius Stargardsky, Robert Oostenveld, Robert Seymour, Robin Tibor Schirrmeister, Ryan Law, Sagun Pai, Sam Perry, Samuel Louviot, Sawradip Saha, Sebastiaan Mathot, Sebastian Major, Sebastien Treguer, Sebastián Castaño, Senwen Deng, Sergey Antopolskiy, Seyed (Yahya) Shirazi, Simeon Wong, Simeon Wong, Simon M

Hofmann, Simon-Shlomo Poil, Sondre Foslien, Sourav Singh, Stanislas Chambon, Steven Bethard, Steven M Gutstein, Svea Marie Meyer, T Wang, Thomas Moreau, Thomas Radman, Timothy Gates, Tom Ma, Tom Stone, Tommy Clausner, Toomas Erik Anijärv, Velu Prabhakar Kumaravel, Will Turner, Xabier de Zuazo, Xiaokai Xia, Yiping Zuo, Zhi Zhang, Ziyi ZENG, btkcodedev, buildqa, and luzpaz. MNE-Python, December 2024.

[32] Eric Larson and Samu Taulu. Reducing Sensor Noise in MEG and EEG Recordings Using Oversampled Temporal Projection. *IEEE Transactions on Biomedical Engineering*, 65(5):1002–1013, May 2018.

[33] Roland R. Lee and Mingxiong Huang. Magnetoencephalography in the Diagnosis of Concussion.

[34] Alexandria McPherson, Steven Bierer, Eric Larson, and Daniel McCloy. 2025-Refined-SSS-Methods-On-Scalp-MEG. February 2025. Publisher: OSF.

[35] Alexandria N McPherson, Iman Fahmy, Eric Larson, Wan-Jin Yeo, Niall Holmes, and Samu Taulu. Refined signal space separation methods for on-scalp MEG systems. *Physics in Medicine & Biology*, 2025.

[36] Hiroatsu Murakami, Zhong I. Wang, Ahmad Marashly, Balu Krishnan, Richard A. Prayson, Yosuke Kakisaka, John C. Mosher, Juan Bulacio, Jorge A. Gonzalez-Martinez, William E. Bingaman, Imad M. Najm, Richard C. Burgess, and Andreas V. Alexopoulos. Correlating magnetoencephalography to stereo-electroencephalography in patients undergoing epilepsy surgery. *Brain*, 139(11):2935–2947, November 2016.

[37] N V Nardelli, S P Krzyzewski, and S A Knappe. Reducing crosstalk in optically-pumped magnetometer arrays. *Physics in Medicine & Biology*, 64(21):21NT03, November 2019. Publisher: IOP Publishing.

[38] Robert Oostenveld, Pascal Fries, Eric Maris, and Jan-Mathijs Schoffelen. FieldTrip: Open Source Software for Advanced Analysis of MEG, EEG, and Invasive Electrophysiological

Data. *Computational Intelligence and Neuroscience*, 2011:e156869, December 2010. Publisher: Hindawi.

[39] R. D. Pascual-Marqui. Standardized low-resolution brain electromagnetic tomography (sLORETA): technical details. *Methods and Findings in Experimental and Clinical Pharmacology*, 24 Suppl D:5–12, 2002.

[40] Mangor Pedersen, David F. Abbott, and Graeme D. Jackson. Wearable OPM-MEG: A changing landscape for epilepsy. *Epilepsia*, 63(11):2745–2753, 2022. _eprint: https://onlinelibrary.wiley.com/doi/pdf/10.1111/epi.17368.

[41] Jens Pogorzelski, Ludwig Horsthemke, Jonas Homrighausen, Dennis Stiegekötter, Markus Gregor, and Peter Glösekötter. Compact and Fully Integrated LED Quantum Sensor Based on NV Centers in Diamond. *Sensors*, 24(3):743, January 2024. Publisher: Multidisciplinary Digital Publishing Institute.

[42] Ethan J. Pratt, Micah Ledbetter, Ricardo Jiménez-Martínez, Benjamin Shapiro, Amelia Solon, Geoffrey Z. Iwata, Steve Garber, Jeff Gormley, Dakota Decker, David Delgadillo, Argyrios T. Dellis, Jake Phillips, Guhan Sundar, Jerry Leung, Jim Coyne, Mike McKinley, Gilbert Lopez, Scott Homan, Lucas Marsh, Mary Zhang, Vincent Maurice, Benjamin Siepser, Teresa Giovannoli, Brandon Leverett, Gabriel Lerner, Scott Seidman, Vicente Deluna, Kayla Wright-Freeman, Julian Kates-Harbeck, Teague Lasser, Hooman Mohseni, T. J. Sharp, Anthony Zorzos, Antonio H. Lara, Ali Kouhzadi, Alejandro Ojeda, Pronoy Chopra, Zachary Bednarke, Michael Henninger, and Jamu K. Alford. Kernel Flux: Optical and Quantum Sensing and Precision Metrology 2021. *Optical and Quantum Sensing and Precision Metrology*, 2021. Publisher: SPIE.

[43] Molly Rea, Niall Holmes, Ryan M. Hill, Elena Boto, James Leggett, Lucy J. Edwards, David Woolger, Eliot Dawson, Vishal Shah, James Osborne, Richard Bowtell, and Matthew J. Brookes. Precision magnetic field modelling and control for wearable magnetoencephalography. *NeuroImage*, 241:118401, November 2021.

[44] Stefan Reimond and Oliver Baur. Spheroidal and ellipsoidal harmonic expansions of the gravitational potential of small Solar System bodies. Case study: Comet 67P/Churyumov-Gerasimenko. *Journal of Geophysical Research: Planets*, 121(3):497–515, 2016. _eprint: https://onlinelibrary.wiley.com/doi/pdf/10.1002/2015JE004965.

[45] J Sarvas. Basic mathematical and electromagnetic concepts of the biomagnetic inverse problem. *Physics in Medicine and Biology*, 32(1):11–22, January 1987.

[46] Holly Schofield, Ryan M. Hill, Odile Feys, Niall Holmes, James Osborne, Cody Doyle, David Bobela, Pierre Corvilain, Vincent Wens, Lukas Rier, Richard Bowtell, Maxime Ferez, Karen J. Mullinger, Sebastian Coleman, Natalie Rhodes, Molly Rea, Zoe Tanner, Elena Boto, Xavier De Tiège, Vishal Shah, and Matthew J. Brookes. A novel, robust, and portable platform for magnetoencephalography using optically-pumped magnetometers. *Imaging Neuroscience*, 2:1–22, September 2024.

[47] Robert A. Seymour, Nicholas Alexander, Stephanie Mellor, George C. O'Neill, Tim M. Tierney, Gareth R. Barnes, and Eleanor A. Maguire. Interference suppression techniques for OPM-based MEG: Opportunities and challenges. *NeuroImage*, 247:118834, February 2022.

[48] Andrzej Skowroński and Kunio Yamagata. Frobenius Algebras I, December 2011. ISBN: 9783037191026 9783037196021 ISSN: 2943-4947, 2943-4955.

[49] J. A. Stratton. Spheroidal Functions. *Proceedings of the National Academy of Sciences*, 21(1):51–56, January 1935.

[50] Samu Taulu and Riitta Hari. Removal of magnetoencephalographic artifacts with temporal signal-space separation: Demonstration with single-trial auditory-evoked responses.

[51] Samu Taulu and Matti Kajola. Presentation of electromagnetic multichannel data: The signal space separation method. *Journal of Applied Physics*, 97(12):124905, June 2005.

[52] Samu Taulu and Juha Simola. Spatiotemporal signal space separation method for rejecting nearby interference in MEG measurements. *Physics in Medicine & Biology*, 51(7):1759, March 2006.

[53] Samu Taulu, Juha Simola, and Matti Kajola. Applications of the signal space separation method. *IEEE Transactions on Signal Processing*, 53(9):3359–3372, September 2005. Conference Name: IEEE Transactions on Signal Processing.

[54] Samu Taulu, Juha Simola, Jukka Nenonen, and Lauri Parkkonen. Novel Noise Reduction Methods. In *Magnetoencephalography: From Signals to Dynamic Cortical Networks*, pages 35–71. July 2014. Journal Abbreviation: Magnetoencephalography: From Signals to Dynamic Cortical Networks.

[55] Tim M. Tierney, Niall Holmes, Stephanie Mellor, José David López, Gillian Roberts, Ryan M. Hill, Elena Boto, James Leggett, Vishal Shah, Matthew J. Brookes, Richard Bowtell, and Gareth R. Barnes. Optically pumped magnetometers: From quantum origins to multi-channel magnetoencephalography. *NeuroImage*, 199:598–608, October 2019.

[56] Tim M Tierney, Zelekha Seedat, Kelly St. Pier, Stephanie Mellor, and Gareth R Barnes. Adaptive multipole models of OPM data. preprint, Neuroscience, September 2023.

[57] K. Uutela, Samu Taulu, and Matti Hämäläinen. Detecting and Correcting for Head Movements in Neuromagnetic Measurements. *NeuroImage*, 14(6):1424–1431, December 2001.

[58] Ruonan Wang, Yujie Ma, Ruochen Zhao, Jin Ding, Ling Li, Yanfei Yang, Fulong Wang, Zhiqiang Cao, Xueying Zhang, Xiaoyang Lin, and Xiaolin Ning. Noise and artifact suppression in SQUID and wearable OPM-MEG: A systematic review of background, physiological, and Technical interference. *NeuroImage*, 318:121403, September 2025.

[59] Norbert Wiener. *Extrapolation, Interpolation, and Smoothing of Stationary Time Series: With Engineering Applications*.

[60] Xueping Xu, Chunbo Han, and Yi Liu. Design of Nonuniform Static Magnetic Compensation Coils for Magnetic Shielding Room. *IEEE Sensors Journal*, 25(9):14950–14959, May 2025.

[61] Gui XUE, Chuansheng CHEN, Zhong-Lin LU, and Qi DONG. Brain Imaging Techniques and Their Applications in Decision-Making Research. *Xin li xue bao. Acta psychologica Sinica*, 42(1):120–137, February 2010.

[62] Andrey Zhdanov, Jussi Nurminen, Joonas Iivanainen, and Samu Taulu. A minimum assumption approach to MEG sensor array design. *Physics in Medicine & Biology*, 68(17):175030, September 2023.